"If a man will begin with certainties, he shall end in doubts; but if he will be content to begin with doubts, he shall end in certainties."

Francis Bacon

A STUDY OF INELASTIC DIFFRACTIVE PROCESSES IN K^-p INTERACTIONS AT 10 GEV/C

by

Martin James Counihan

A thesis presented for the degree of Doctor of Philosophy of the University of London.

Department of Physics,
Imperial College of Science and Technology,
London, SW7

April 1971

ABSTRACT

This thesis is based on an experimental investigation of K^-p interactions at 10 GeV/c. It begins with an account of experimental procedures, after which we discuss the limitations of the experiment and some general features of the data as illustrated by the single-pion-production reactions. We go on to investigate diffractive dissociation, which can occur in a variety of reactions, and in particular we develop a partially dual model to describe the production of the Q and L mesons.

CONTENTS

(continued)

CHAPTER 1

THE 10 GEV/C EXPERIMENT

The experiment on which this thesis is based was originally proposed at the beginning of 1965, and was intended to investigate the interactions of negative K-mesons with protons using a K-meson beam with momentum 10 GeV/c. This was the highest momentum available at the time, and was obtained using the CERN Proton Synchrotron situated at Meyrin, near Geneva. Initially, the interactions were recorded in the British National Hydrogen Bubble Chamber.

The objectives of the experiment were to examine the mechanisms by which particles and resonant states could be produced, and to study their properties. It was anticipated that many theoretical models could be put to the test in this way, and that our knowladge of the hadron spectrum could be improved and extended. In particular, much was to be learned concerning "strange" hadrons such as the K^* resonances and the Omega-minus particle.

The first period of beam tuning and bubble chamber exposure began in April, 1965, and is referred to as "experiment 75". Since then there have been three additional sets of data taken with the same K^- beam momentum, namely experiments 10, 12 and 13. In all, some 700,000 photographs of the bubble chamber have been taken, and each shows a burst of (on average) eight K^- mesons passing through it. A small proportion of these interact with the hydrogen nuclei in the chamber, and most of those which do so lead to final states which are of interest to us. Such "events" are analysed from the photographic film, and when all the film analysis is complete some 300,000 events will have been measured.

Five European research groups have collaborated in all stages of the experiment (Refs. 1.1-1.5). The work has so far extended over five years, and the processing of the remaining film from experiments 12 and 13 will continue for at least another two years, into 1972.

Needless to say, experimental techniques and methods of data processing are constantly being revised and improved upon. For example, the beam and bubble chamber set-up has changed considerably from the original arrangement which was used in 1965, and film measurement techniques have advanced a great deal with the introduction of automatic measuring machines of various types. Furthermore, the computing facilities available to the collaboration have multiplied over the years, and the data processing systems and computer programs that we use are in a state of constant evolution.

For most of the people involved, the day-to-day work of the experiment consists largely of developing, updating and maintaining our systems to handle the flow of data to be analysed. The measuring and the analysis of events is a continuous process which is being accelerated steadily. For these reasons, this experiment and others like it have not only advanced our knowledge of high-energy particle physics, but have also taken advantage of and given impetus to many other areas of science and technology.

The justification for all this development lies in the statistical nature of the physics of hadronic interactions. As very large amounts of data become available, not only can we attach more precision and significance to our results, we can also investigate the underlying physical principles in greater depth.

In the remainder of this chapter, I shall describe briefly the principles by which the beam line and bubble chamber are used to produce photographic data on K^-p interactions at 10 GeV/c. In view of the many alterations which have been made to this system over the years, details have been omitted and the account is a very general one.

The published papers in which the work of the collaboration has been reported are listed in Refs. 1.6 et seq.

The Beam Line

The CERN Proton Synchrotron is capable of accelerating protons to a momentum of about 27 GeV/c, and in order to obtain a beam of 10 GeV/c negative kaons from this it is necessary to use a target placed in the path of the extracted proton beam. From such a target, a very large number of particles will be emitted, of various types, moving in a direction close to that of the incident proton beam but with a wide spectrum of momenta.

This secondary beam is then passed down the "beam line", which is a complicated chain of devices designed to collimate and purify the beam so that the bubble chamber can be exposed to a narrow beam of kaons of the desired momentum. Focussing is done chiefly by pairs of quadrupole magnets, and also by the use of "bending" magnets which deflect the beam. These latter play an important part in the momentum separation of the beam, for the angle through which any particle in the beam is deflected in passing across the magnetic field is dependent upon its momentum. In this way it is arranged that particles of momentum other than about 10 GeV/c are deflected away from the direction of the beam line. Collimating slits which will absorb such unwanted particles are spaced at intervals along the beam line.

While momentum separation is a relatively straightforward process, the problem of separating out unwanted types of particle is more difficult. There exist two methods of doing this, namely by "electrostatic" separation and by "radio-frequency" or R.F. separation. Both techniques use the fact that the masses of the beam particles differ from one another. The kaons, in which we are interested, have a mass of 494 MeV/c^2, to be compared with, say, 140 MeV/c^2 and 938 MeV/c^2 for tha pions and antiprotons which will have to be removed. At a fixed momentum of 10 GeV/c for all particles, these differences in mass imply differences in velocity.

In this experiment R.F. separation has been used, since electrostatic separators are not suitable at high energies. R.F. separation is essentially a "time-of-flight" method for distinguishing particles of different velocity. The separators, of which there are two in our beam line, each consist of a pair of

radio-frequency oscillating cavities, between which is a focussing device to focus the beam particles emerging from the first oscillator into the second. In passing through each cavity, the beam particles are deflected through an angle which depends on the phase of the oscillation at that instant; in passing through a complete separator, the deflection depends on the relative phases of the two oscillators as seen by each particle, and this relative phase is determined by the time of flight between them.

By adjusting the frequency of the oscillating cavities and the distance between them, this method of distinguishing particles of different velocities can be made sufficiently precise for the beam line to transmit only a pure sample of kaons at 10 GeV/c.

The Bubble Chamber

The kaons are transmitted down the beam line and into the bubble chamber, not continuously, but in short bursts with a repetition rate which is determined by the frequency with which the original protons are ejected from the synchrotron. As each burst passes through the chamber, K^-p interactions may take place with the protons which are the atomic nuclei of the liquid hydrogen contained in the chamber. These interactions will in general produce numbers of secondary charged particles, the trajectories of which must be made visible if the interactions are to be observed and measured. This is done in the following way.

The hydrogen in the bubble chamber is kept in a liquid state through being maintained under pressure at a temperature (27° K) which, if it were at atmospheric pressure, would be well above its boiling point. Thus, by slightly relaxing the pressure, the liquid can be put into a "superheated" state, and under certain conditions bubbles of hydrogen gas may appear. Now, when a fast charged particle moves through the bubble chamber, it will cause ionisation of the hydrogen along its track. If the hydrogen is superheated, the ions will act as nuclei for bubble formation. These bubbles are visible and can be photographed, leaving a record of the trajectories of the kaons and the charged products of their interactions.

FIGURE 1.1

Operation of the Beam Line and Bubble Chamber.

(Solid arrows represent particle flow, and broken arrows the time sequence.)

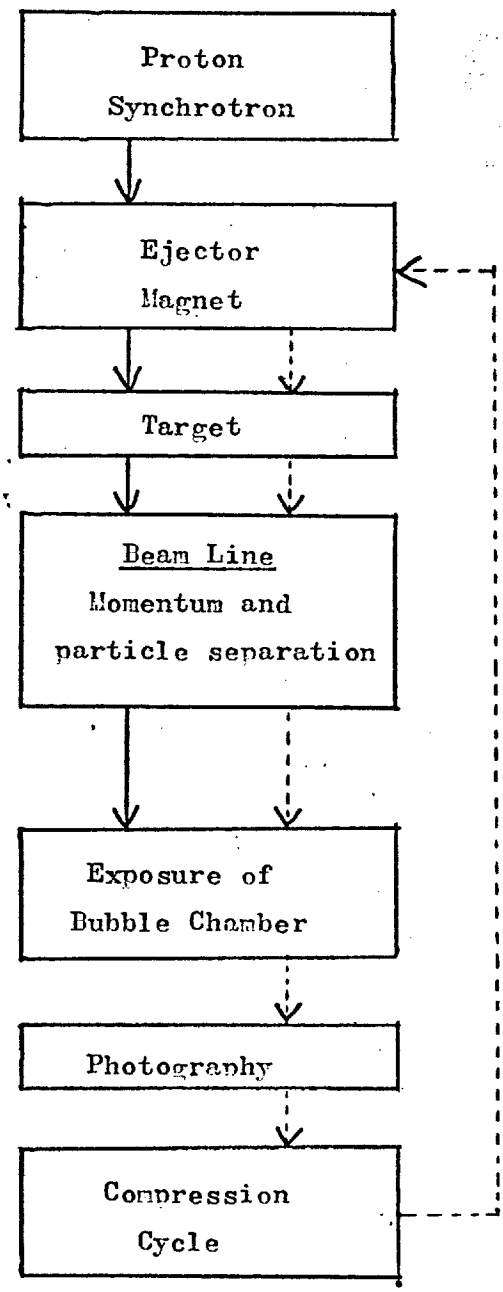

Accelerates the original protons.

Ejects a burst of high-momentum protons.

Gives off a secondary beam.

Restricts the beam to one of K^- mesons at 10 GeV/c.

K^-p interactions occur.

Charged particle tracks are recorded.

Chamber is cleared in preparation for the next burst.

When this has been done, the chamber is repressurised and cleared of bubbles, and depressurised again just before the next burst of kaons is received. This cycle is repeated every two seconds or so. In order to take photographs, the interior of the chamber is illuminated by a battery of flash lamps. Three cameras are used, separated from one another so that the events photographed can be reconstructed in three dimensions.

The complete sequence of events is illustrated by figure 1.1.

References (1)

1.1 Physikalisches Institut der Technisches Hochschule, Aachen.

1.2 Forschungstelle fur Physik Hocher Energien der Deutschen Akademie der Wissenschafter zu Berlin, Zeuthen.

1.3 European Centre for Nuclear Research (CERN), Geneva.

1.4 Department of Physics, Imperial College of Science and Technology, University of London.

1.5 Institut fur Hochenenergiephysik der Universitat, Wien.

1.6 Observation of a (K-PI-PI) resonance near 1800 MeV.
Bartsch et al., Physics Letters 22 , 357 (1966)

1.7 K^-p Elastic Scattering at 10 GeV/c.
Aderholz et al., Physics Letters 24B , 434 (1967)

1.8 Xi-minus, Omega-minus and Antibaryon Production in 10 GeV/c K^-p interactions.
Bartsch et al., Nuclear Physics B4 , 326 (1968)

1.9 Lamda Production in 10 GeV/c K^-p Interactions.
Aderholz et al., Nuclear Physics B5 , 606 (1968)

1.10 $K^*(890)$ Production in 10 GeV/c K^-p Interactions and Comparison with Absorption and Regge Pole Models.
Aderholz et al., Nuclear Physics B5 , 567 (1968)

1.11 Mass Dependence of the Small Angle Differential Cross Sections for High Energy Interactions.
Bartsch et al., Physics Letters 27B , 336 (1968)

1.12 Total and Differential Cross Sections in 10 GeV/c K^-p Interactions.
Aderholz et a., Nuclear Physics B7 , 111 (1968)

1.13 Analysis of the $K^*(1320)$ and L-Mesons produced in 10 GeV/c K^-p Interactions.
Bartsch et al., Nuclear Physics B8 , 9 (1968)

1.14 Evidence for a New Xi Resonance at 2500 MeV in 10 GeV/c K^-p Interactions.
Bartsch et al., Physics Letters 28B 439 (1969)

1.15 Omega-minus Production in 10 GeV/c K^-p Interactions.
Speth et al., Physics Letters 29B , 252 (1969)

1.16 Production of Strange Particles in 10 GeV/c K^-p Interactions and Comparison with the Predictions of the Multiperipheral Model.
Bartsch et al., Nuclear Physics B11 , 373 (1969)

1.17 Production of Proton-Antiproton and Kaon-Antikaon Pairs in four-body reactions of 8 GeV/c PI^+ and 10 GeV/c K^- on Protons.
Aderholz et al., Nuclear Physics B14, 255 (1969)

1.18 A Study of the Reaction $K^-p \longrightarrow pK^0\pi^-$ with the Veneziano Model.
Bartsch et al., Nuclear Physics B20 , 63 (1970)

1.19 Comparison of $\pi^\pm p$ and K^-p Reactions with the Multiperipheral Model using the Van Hove Hexagon and Cuboctahedron Plots.
Bartsch et al., Nuclear Physics B19 , 381 (1970)

1.20 Evidence that the L-Meson has Decay Modes Other than $K^*(1420)\pi$.
Bartsch et al., Physics Letters 33B, 186 (1970)

1.21 Application of the Veneziano Model with Pion and Pomeron Exchange to the Reaction $K^-p \rightarrow nK^-\pi^+$ at 10 GeV/c
Bartsch et al., Nuclear Physics B23 , 1 (1970)

1.22 A Dual Diffractive Model for the 0- and L-Mesons
Bartsch et al., Nuclear Physics B24 , 221 (1970)

CHAPTER 2

ANALYSIS OF THE FILM

This chapter will be devoted to an account of the procedure which is being used at Imperial College for the analysis of the "experiment 13" film, i.e. the latter part of the 10 GeV/c experiment. This film was taken at Easter, 1969, using the CERN two-metre bubble chamber. The system as a whole is illustrated by figure 2.1 .

2.1 FILM SCANNING

When the bubble chamber film is received, it is first of all necessary to scan through it visually in order to spot the events of interest and to make certain decisions about them. Within the image of the bubble chamber, each frame shows not only the particle tracks but also certain fiducial marks. These are used to define a fiducial region for scanning purposes, as well as to determine the position of the event when it is measured.

Outside the image of the bubble chamber, each frame shows certain additional items of information, namely the number of the frame and of the roll, the view number and the date of exposure. This information is also given in a form in which it can be sensed and checked by the automatic measuring machine, and there are also "Brenner marks" by which the position of the film can be automatically sensed.

Topology Convention

Since the K^-p system has no net charge, a genuine event will appear with as many positive as negative tracks leaving the interaction vertex, and these are distinguished from one another by the directions of their curvatures in the magnetic field which is applied to the chamber. Clearly, there must be an even number of "prongs" leaving the vertex.

FIGURE 2.1

Organisation of Film Analysis.

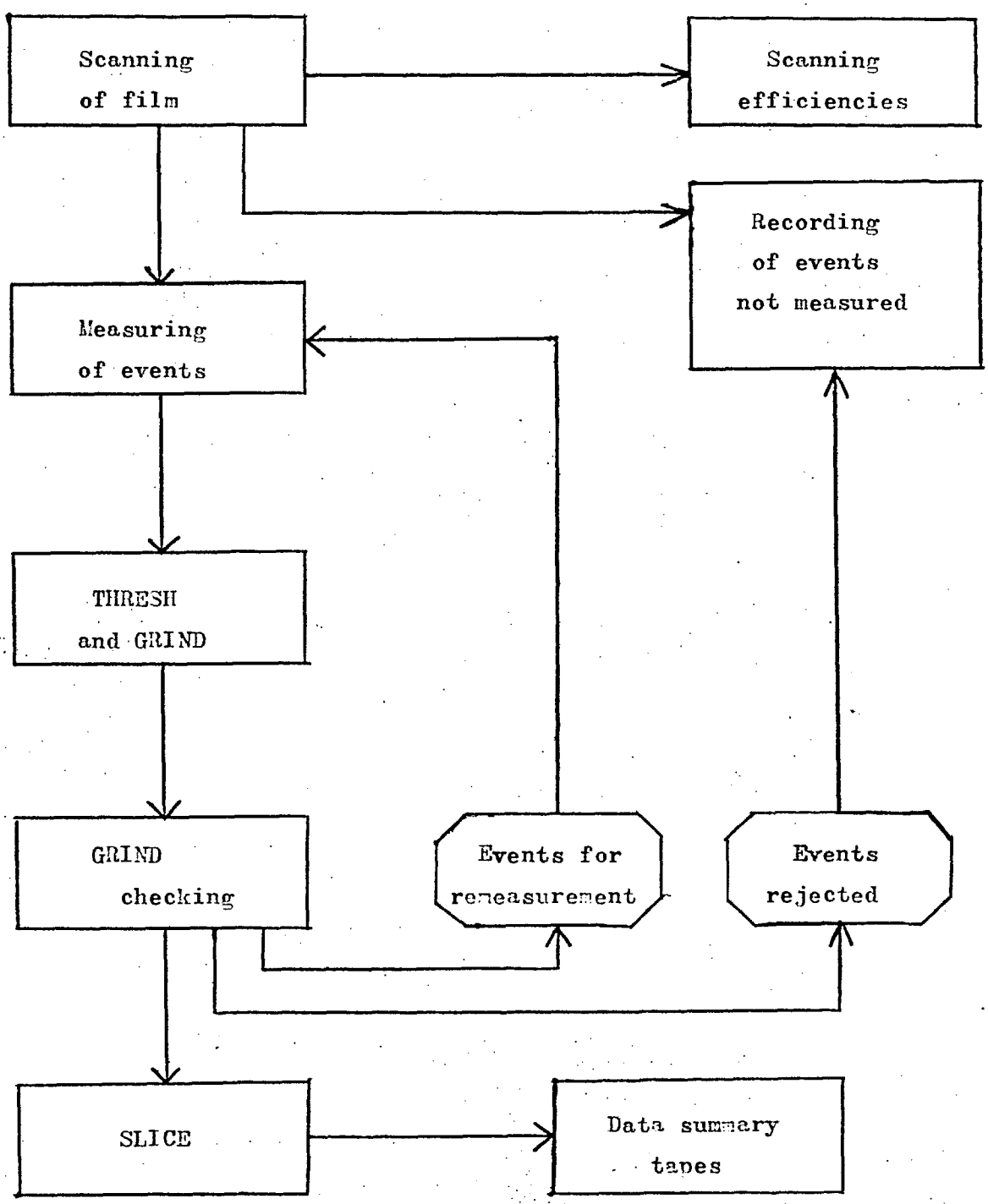

The topology of the event is represented by a three- digit number, of which the first digit is the number of prongs, the second is the number of these prongs which "kink", and the third is the number of "V^0's" which may be associated with the event. A kink in a track corresponds to an in-flight decay of the particle, involving the emission of an unseen neutral particle at the kink. A V^0 is a pair of tracks, one positive and the other negative, coming from a point at which a neutral particle has decayed in flight.

Acceptance of events

A rigid set of rules have been laid down concerning the acceptance of events for measurement. We measure all even-prong events with the exceptions of the topologies 000 and 410, 610, 810, etc. Normally, events for measurement must lie with their interaction vertices within a fiducial region which is defined by the positions of certain fiducial marks as seen on the first view; this is region 1 of figure 2.2. Region 2 limits the acceptance of neutral decay vertices, i.e. V^0's. If an event has more than one decay (charged or neutral) associated with it, it is classified as "rare" and will be measured if the interaction vertex is in either region 1 or region 2.

Furthermore, we measure the three-prong "tau" decays of the beam which are occasionally seen. Region 1 is the fiducial region for these.

Event types which are not to be measured are in any case scanned for in region 1, and their occurence is recorded. We also record events which, although of acceptable topology, could not be measured successfully, such as some which involve complicated secondary interactions close to the primary interaction vertex.

In the course of a scan through a roll of film, the scanner prepares a deck of "scan cards" on which are written the items of information needed for each event. There is one card for each event, giving the frame number, the serial number of the event

FIGURE 2.2

Bubble Chamber Fiducials.

(In the CERN 2 metre chamber, as seen on view 1.)

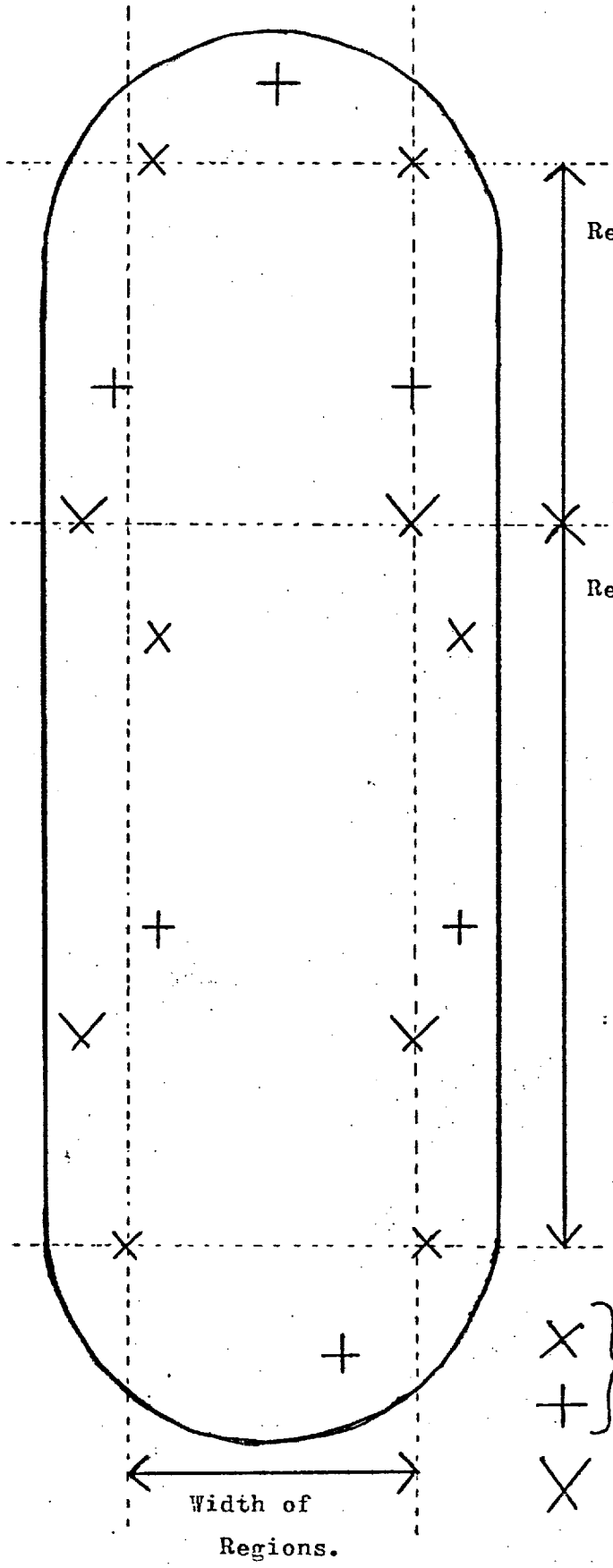

within the frame, the topology of the event, a number identifying the scanner personally and a small sketch of the event. In addition, comments must be written for the attention of either the measurer or a physicist summarising any further information according to well-defined rules. As an example of such a comment, if an electron pair is seen which may be associated with an event, it will be brought to the attention of a physicist by writing the abbreviation "EP".

Check Scanning

To reduce the probability of an event's being missed, two independent scans are made through every roll of film, and then the two sets of scan cards are used in making a "check scan" through the film. This is done by a physicist or well-experienced assistant.

The check scan involves comparing the two sets of scan cards and correcting any errors which may be present so as to produce a single set of cards which can be passed to the measurers of the film. These final scan cards are in the same form as those written during the first two scans, containing the identifications of the one or two original scanners of each event.

Although the majority of events are seen by both scanners, there are many which are seen by only one. From the final scan cards, an analysis can be made which gives the "detection efficiency" for each individual scanner. This is done periodically, and the results are used to encourage the quality of the scanning to be maintained.

Scanning Efficiencies

A film scanning system cannot be perfect, and it is important to be able to calculate the proportion of events of each topology which are missed through human error. This is done simply by counting the number of events seen by two scanners and the number seen by only one, for each type of event. From these two figures it is possible to calculate the probability that an event will be seen during a scan, and hence the number of events which

must actually have occured. These results are of importance in working out absolute cross-sections for the various reactions which can take place, since we must then allow for those events which went unnoticed. Scanning corrections are of the order of a few percent, and become less important for more complicated topologies.

The amount of film from experiment 13 which is being measured at Imperial College is 76 bobbins, each of which has about 775 frames. (A "roll" of film consists of four bobbins). An analysis of the kind mentioned above has been made from a sample of the scan cards; of the total of some 59000 frames, the sample covered 6200, and indicated that a total of about 35000 events will have to be measured and/or recorded. That is to say, we have an average of 0.6 events per frame.

Three-prong decays of the beam particles ("taus") were found to occur very infrequently, with about one frame in 200 containing such an event. This is to be expected with a K^- beam of this momentum. Further results of the scan-card analysis are summarised in figure 2.3.

FIGURE 2.3

Results from Analysis of Scan Cards.

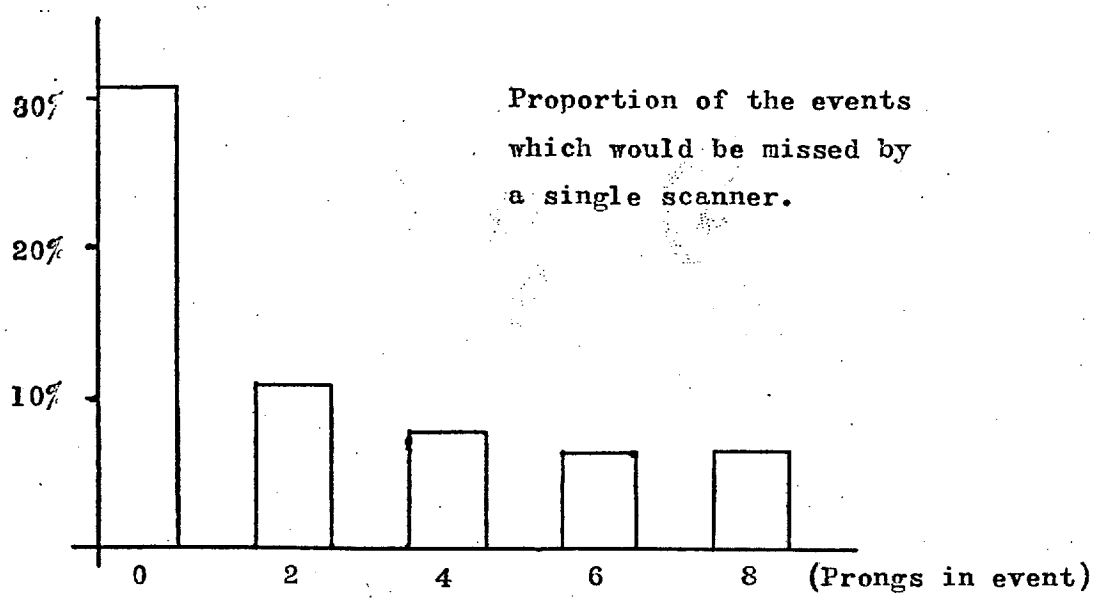

Proportion of the events which would be missed by a single scanner.

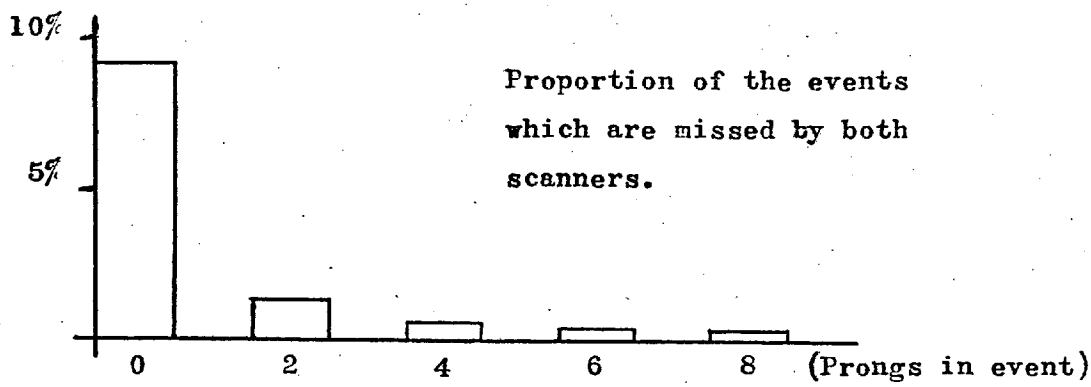

Proportion of the events which are missed by both scanners.

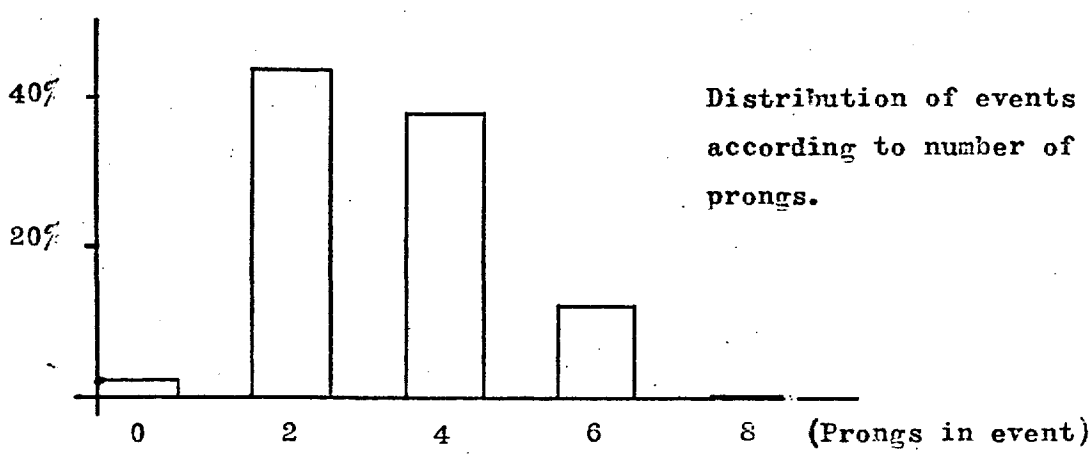

Distribution of events according to number of prongs.

2.2 MEASUREMENT OF EVENTS

The sequence of operations required in measuring our film is illustrated by figure 2.4.

Roadmaking

The automatic measuring machine (H.P.D.) takes as input digitised information concerning the location and topology of each event on the film. This is provided by the "roadmaking" (sometimes called "rough digitising") machines. Their operators record the identification of each event, its topology code, and the positions of certain points on it.

These points are: fiducial marks, the primary interaction vertex, the vertices of kinks, V^0's and secondary interactions, a series of points along each track and the end points of any stopping proton tracks. The coordinates of these points are given by the roadmaking machines with respect to the first fiducial mark. "Labels" are also transmitted to specify which point is which, which view of the event is being measured, and so on.

In order to check the consistency of these items of information, the roadmakers are monitored by the program ONLINE, and there is two-way teletype communication between the computer and the roadmaker operators. These teletypes are used by the operators in the recording of frame numbers, view codes, point labels etc., and by the program in acknowledging that measurements are registered on the roadmaking machines in accordance with these details.

If the roadmaking of an event is not correct, the ONLINE program may alert the operator and request a repeat. When a satisfactory set of points has been digitised, ONLINE will transfer the infomation onto tape. This is the input to the next program in the chain, which is MIST.

The exception to all this, which occasionally arises due to computer failures, is the temporary loss of the ONLINE program.

FIGURE 2.4

Measuring Events through the H.P.D.

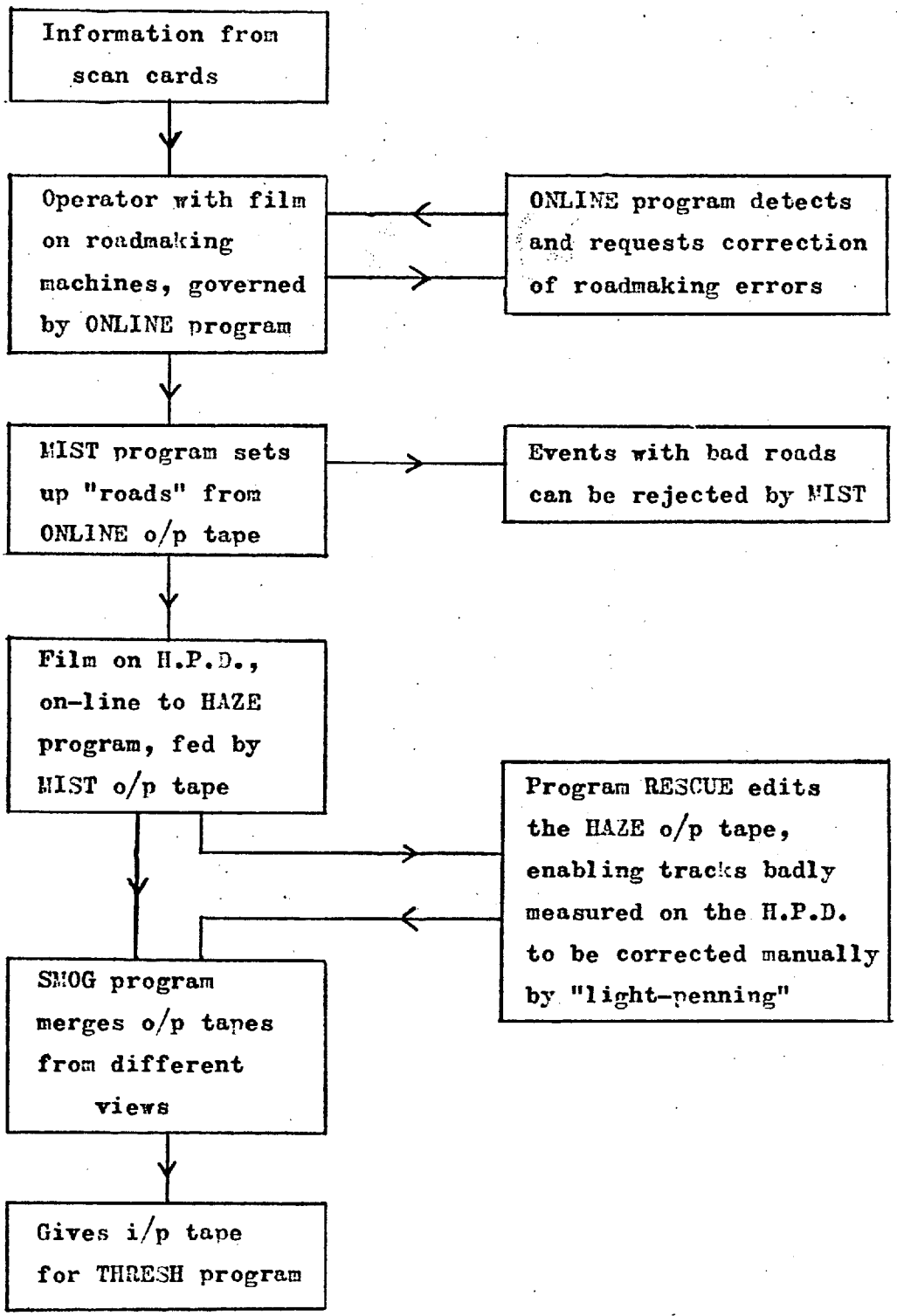

When this happens roadmaking can still be done, with direct paper tape output, and processed at a later stage; when roadmaking is done "off-line" in this way, errors cannot be immediately detected and so a larger proportion of events have to be sent back for roadmaking a second time.

The Program MIST

The roadmaking machines and ONLINE program give us the coordinates of a series of points along each track, and it is the function of MIST to construct "roads" through these points: These roads are the regions of the film which will be scanned by the H.P.D.

If the points for a track presented to the program do not lie approximately on an arc of a circle then the event may be rejected by MIST. However, about 95% of frames are passed through MIST successfully.

The H.P.D.

The H.P.D. (or Hough-Powell Device, after its original inventors) is a mechanism which, under computer control, makes a scan of a bubble chamber film frame and registers the bubble images which go to form the tracks. It does this optically, using a very narrow beam of light and detectors which measure the attenuation of the beam in passing through the film.

Under the guidance of the program HAZE, the H.P.D. makes precise measurements of the tracks and also records their degree of ionisation. If for some reason the machine is unable to do this (e.g. if a track cannot be distinguished in one of the roads) then the program will dump onto the output tape all the relevant information regarding that track, including all the digitised bubble images in its vicinity. These are subsequently dealt with manually by "light-penning" on a C.R.T. display.

Light-Penning

The HAZE output tape is the input to the program RESCUE which, on-line to a C.R.T. display, enables an operator to take appropriate action whenever a track has been unsatisfactorily treated in HAZE. The C.R.T. is used to display the road points, bubble positions and other items of information. The track which is giving trouble, and the reason why it was "dumped", are usually clear to the operator. For example, it may happen that, as a result of faulty roadmaking, the actual track does not lie within the road.

Corrective action is taken using a "light pen" to which the program will respond when it is applied to the C.R.T. screen. By drawing the light pen along the bubble images which comprise the track, the operator will trigger the RESCUE program into recalculating the position of the track, independently of the original roads. About 50% of the tracks displayed have to be treated in this way; the remainder are either judged to be good enough as they stand, or are so badly determined that no further attempt is made to obtain a measurement. In the latter case, it is hoped that the other two views of the event will be measured well, so that the subsequent stereoscopic reconstruction of the event may still be successful.

About 30-40% of tracks are dumped on the HAZE output tape and so are displayed by the RESCUE program as described above. The output from the latter does not contain these tracks in "dumped" form, but in the same form as those which passed successfully through HAZE.

The SMOG Program

When the film has been put through the H.P.D. and the HAZE output has been passed through RESCUE, the measurements of the three views of each event (which will have been written onto different tapes at different times) must be collated and merged onto a single magnetic tape. This is done by the program SMOG, the output from which is the input for the THRESH program.

2.3 THRESH and GRIND

The program THRESH computes the three-dimensional geometry of each event from the measurements of the three views on film. The particle tracks are helices with slowly-decreasing curvatures; this decrease in curvature is due to the slowing-down of the particles, and depends on their masses.

THRESH requires information ("titles") to be fed into it at the beginning of each run. These titles give the positions of the cameras and of the fiducial marks in the chamber, various optical parameters, criteria for mass assignments to particles, criteria for the treatment of short stopping tracks, and so on.

Since there are three views of each event rather than two, there is some overdetermination of the three-dimensional configuration. This is necessary for a statistical fit to be made to the measurements, and the output from THRESH contains not a single, precise set of coordinates and helix parameters but a number of fits, corresponding to different mass assignments for the particles, together with statistical errors. In addition to this, the program can output information on the degree of ionisation in each track.

GRIND is the program which we use to analyse each event kinematically from the output of THRESH. Like THRESH, GRIND has to be preloaded with experiment-dependent titles, and these contain among other things a list of hypotheses for explaining the events. The program will output the details of a statistical fit to the plausible hypotheses; it is convenient to classify these fits according to the number of independent constraints which are used in making them.

GRIND Checking

In general, an event involving only charged particles will give rise to a four-constraint (4-C) fit; if there is one unseen neutral particle, its momentum can be reconstructed in a 1-C fit.

If secondary interactions or decays are involved, each vertex is fitted individually before the event as a whole is fitted. The overall number of tenable hypotheses can become quite large. To decide finally on its classification, every event is looked at on a scan table and checked against the GRIND output. Many factors play a part in this final decision-making — the ionisations of the tracks, the statistical probabilities of the fits, the presence of electron pairs and so forth.

More often than not, an event cannot be assigned uniquely to a particular fitted hypothesis. It often happens that the event is underconstrained, e.g. when there are two or more unseen neutral particles produced. These "nofit" events are classified according to the identities of the observed charged particles, although these are often ambiguous. Unresolvable ambiguities occur to a lesser extent with fitted events.

Standardised criteria are used in GRIND checking. We will always take 4-C fits in preference to 1-C fits, for example, and fits will be taken in preference to nofits. "0-C" events, which cannot be fitted statistically but which are reconstructed by simply solving the energy-momentum conservation equations, are rejected.

Broadly speaking, the GRIND checking of an event will result in one of the following types of decision being made:

(i) The event is satisfactorily and uniquely fitted and assigned to an hypothesis.

(ii) The event is fitted, but must be taken as ambiguous between two or three hypotheses.

(iii) Because of the production of neutral particles, the event is not fitted, but is assigned to a nofit hypothesis.

(iv) The event is unfitted and ambiguous between two or three nofit hypotheses.

(v) The event will have to be rejected. This is the case with 0-C events, and sometimes with events which are too complicated to be measurable, and with events which should not have been measured in the first place such as those occuring

outside the fiducial region.

(vi) The event will have to be remeasured. This may be because some obvious fault comes to light in the original measurement, or because of some inconsistency between between the event on film and the GRIND output for it; e.g. the ionisations of tracks may be inconsistent with the fits made by the program.

The Production of D.S.T.'s

Data Summary Tapes, or D.S.T.'s for short, are prepared from the GRIND output tape through the program SLICE, using "slice cards" which specify the hypothesis or hypotheses accepted for each event in the GRIND checking.

A D.S.T. record is written for every hypothesis, containing all the information which may be relevant to analysing the underlying physics of the interactions. Besides calculating such quantities as C.M. momenta, effective masses of combinations of particles, invariant momentum transfers and so on for the D.S.T., SLICE computes the experimental errors on these physical quantities from the error matrix calculated in GRIND.

Non-unique hypotheses are flagged as such on the D.S.T., and can be given a weight which is the inverse of the total number of hypotheses fitting the event. Events involving strange particle decays can be given a "decay weight" determined by the probability that the strange particle might not have been seen to decay.

Our D.S.T.'s are the end product of the film analysis system described in this chapter, and are our starting point for the study of the physics of the K^-p interaction at 10 GeV/c.

CHAPTER 3

SINGLE PION PRODUCTION

A K^-p interaction can lead to single pion production in four possible charge states:

(i) $K^-p \rightarrow K^0\pi^-p$
(ii) $K^-p \rightarrow K^-\pi^0p$
(iii) $K^-p \rightarrow K^-\pi^+n$
and (iv) $K^-p \rightarrow K^0\pi^0n$.

In case (i), if the K^0 is seen to decay by $K^0 \rightarrow \pi^+\pi^-$, this decay is measured and a 4-C (four-constraint) fit is made to the event. If the K^0 is not seen to decay, and in cases (ii) and (iii), the momentum of the neutral particle must be calculated and a 1-C fit is made.

3.1 THE DATA

$K^-p \rightarrow K^0\pi^-p$

Our data sample contains 494 4-C events of the type with seen K^0 decay. These events are extremely reliable, and all but two of them were fitted uniquely to the $K^-p \rightarrow K^0\pi^-p$ hypothesis. Associated with each event is a "decay weight" to allow for similar events where the K^0 may have decayed into $\pi^+\pi^-$ outside the limits of our fiducial region in the bubble chamber. The sum of these weights is 562.8, and when we also allow for the neutral decay modes and the long-lived component of the K^0 we arrive at 1,639 as the number of events of type (i) which probably took place. Using the microbarn equivalent calculated in Appendix A, this corresponds to a cross-section of 0.318 mb. $\pm$ 6% .

Since the K^0 is seen in 494 cases, we might expect to find about 1,145 1-C events where the K^0 is not seen.

There are 1,281 1-C events fitted to reaction (i), but 342 of these are fitted ambiguously with other hypotheses. It is our

practice to give ambiguous events a weight which is the reciprocal of the number of different hypotheses to which they can be fitted. This "hypothesis weight" is almost always $\frac{1}{2}$, and is occasionally $\frac{1}{3}$. Taking this into account, our 1,281 events are weighted to 1,110 , which compares well with the number mentioned in the last paragraph.

$\underline{K^- p \rightarrow K^- \pi^0 n}$

The events in this channel are invariably 1-C fits, and we have 2,171 of them. Allowing for those which are ambiguous, this number is weighted down to 1,995.5 , implying a cross section of 0.387 mb. $\pm$ 4%.

There are 347 ambiguous fits in this channel, a high proportion of them ambiguous with the 1-C $K^0\pi^-p$ events mentioned above. We shall investigate this problem of ambiguities and that of possible misfitting in more detail later.

$\underline{K^- p \rightarrow K^- \pi^+ n}$

This channel contains 2,627 1-C events, of which 24 are ambiguous, so that the weighted sum is 2,615. This corresponds to a cross section of 0.507 mb. $\pm$ 4%. The low proportion of ambiguous events is partly due to the fact that a positive pion can almost always be distinguished from a proton by its ionisation, so there is little chance of confusion between this channel and the $K^- p \rightarrow K^- \pi^0 p$ and $K^- p \rightarrow K^0 \pi^- p$ channels.

Though we have no difficulty with ambiguous events in this channel, it is likely that some contamination is present from the unfittable reaction $K^- p \rightarrow K^- \pi^+ \pi^0 n$, particularly when the $\pi^0 n$ system has a low effective mass.

$\underline{K^- p \rightarrow K^0 \pi^0 n}$

This channel contains at least two unseen neutral particles (the topology will be either 000 or 001) and no fit can be made to such an event. Our experiment therefore provides no useful information on this reaction.

3.2 AMBIGUITIES AND BIASES

$K^-\pi^0 p \leftrightarrow K^0\pi^- p$ Ambiguities

As we mentioned in the previous section, there are nearly 350 ambiguous events in our data which give 1-C fits to both reactions (i) and (ii). We must ask ourselves what properties such events are likely to have, and whether or not it is safe to proceed with the analysis of the data without making corrections for them.

The situation is illustrated by figure 3.2.1, and the criterion for ambiguity to occur is that the final-state kaon and pion should have momenta (lab. frame) equal in magnitude.

To understand why this is so, bear in mind that the momenta of the charged particles are measured independently of their masses, and that the momentum of the neutral particle follows by subtraction. On the other hand, energies of the particles depend on their masses, and if both fits to an event satisfy overall energy conservation we must have

$$E(K^0) + E(\pi^-) = E(K^-) + E(\pi^0)$$

i.e.

$$(\underline{p}_o^{\,2} + m_K^{\,2})^{\frac{1}{2}} + (\underline{p}_-^{\,2} + m_\pi^{\,2})^{\frac{1}{2}} = (\underline{p}_-^{\,2} + m_K^{\,2})^{\frac{1}{2}} + (\underline{p}_o^{\,2} + m_\pi^{\,2})^{\frac{1}{2}}$$

which is only the case if $\underline{p}_o^{\,2} = \underline{p}_-^{\,2}$. In figure 3.2.2, the quantity $/\underline{p}_-/ - /\underline{p}_o/$ is shown for the ambiguous data as well as for the uniquely-fitted data, and our result is confirmed.

Using the Monte-Carlo event-generating program FOWL, we have examined events which satisfy our criterion for ambiguity, and found that they lead to no anomalous behaviour in the distributions (mass spectra, t-distributions, etc.) which are of physical interest.

FIGURE 3.2.1

Cannot distinguish between this:

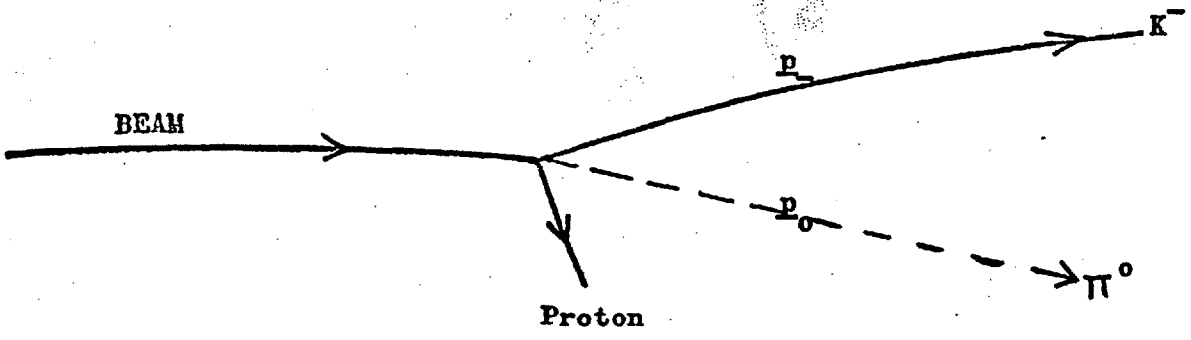

and this:

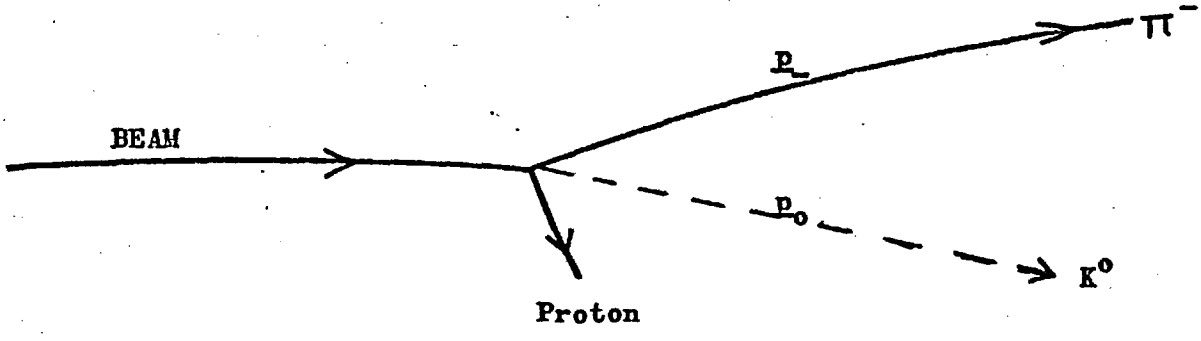

FIGURE 3.2.2 Differences in Lab. Momenta between kaon and pion tracks. (500 MeV/c bins)

(a) $p(K^0) - p(\pi^-)$, unique fits.

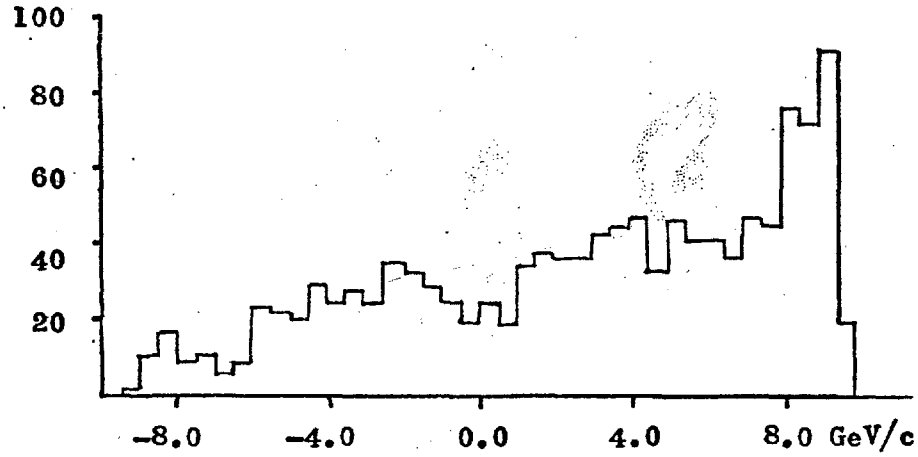

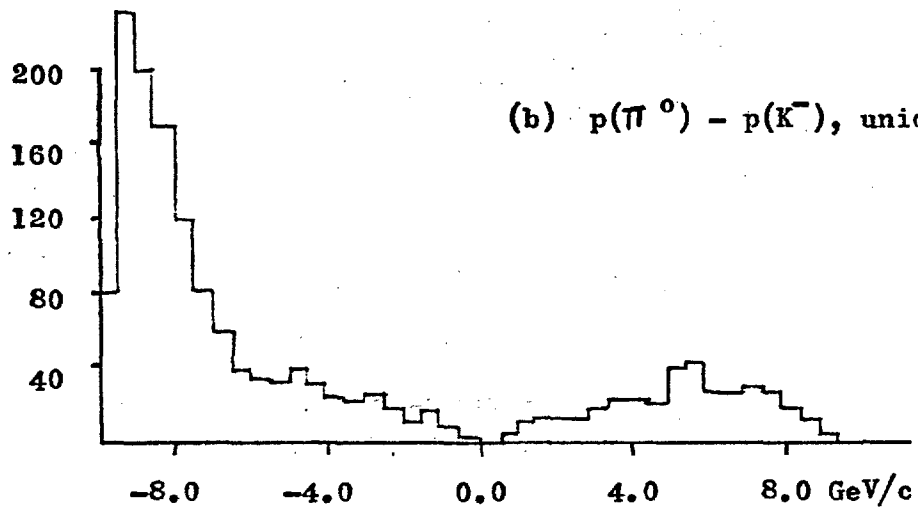

(b) $p(\pi^0) - p(K^-)$, unique fits.

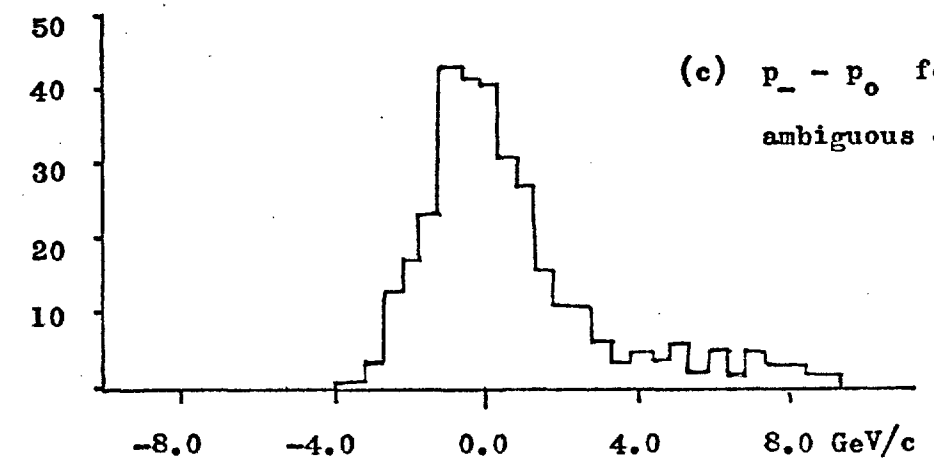

(c) $p_- - p_o$ for ambiguous events.

Misfits in $K^- p \rightarrow K^- \pi^0 p$

Figure 3.2.3 shows the $K^-\pi^0$ effective mass spectrum for our reaction (ii) data, as well as $m(K^0\pi^-)$ for reaction (i). In the former, there is a clear enhancement just above threshold and well below the $K^*(890)$ mass. In the latter, there is no such enhancement.

There is no plausible physical reason why an excess of events should appear in this region for reaction (ii), and we shall argue that it arises from elastic events which are misfitted because of imprecision in determining the beam momentum.

To fit a π^0 in this way (see fig. 3.2.4), we must have

$$m_{\pi}^2 = (E(B') - E(B))^2 - (\underline{p}(B') - \underline{p}(B))^2$$

and when the beam is relativistic, this gives

$$m_{\pi}^2 = m_K^2 .(2 - p(B)/p(B') - p(B')/p(B)) - 2p(B')p(B).(1-\cos\theta)$$

where θ is the angle between $\underline{p}(B')$ and $\underline{p}(B)$. When $\underline{p}(B')$ and $\underline{p}(B)$ are not very different, the first term is small. The last term can be written in terms of the pion's transverse momentum to give

$$m_{\pi}^2 = -p_t^2(\pi) \quad .$$

Now, for the purposes of fitting we can have $-0.12 \lesssim m_{\pi}^2 \lesssim 0.1$, so such a fit can be made if

$$p_t(\pi) \lesssim 110 \text{ MeV/c.}$$

That is to say, if a extra π^0 is fitted (because of a badly-known beam momentum) to an elastic event, then the π^0 will have a very low transverse momentum. A consequence of this is that all the tracks will be approximately coplanar.

Figure 3.2.5 shows that the events in the $K^-\pi^0$ peak do, in fact, have predominantly low transverse momenta.

FIGURE 3.2.3

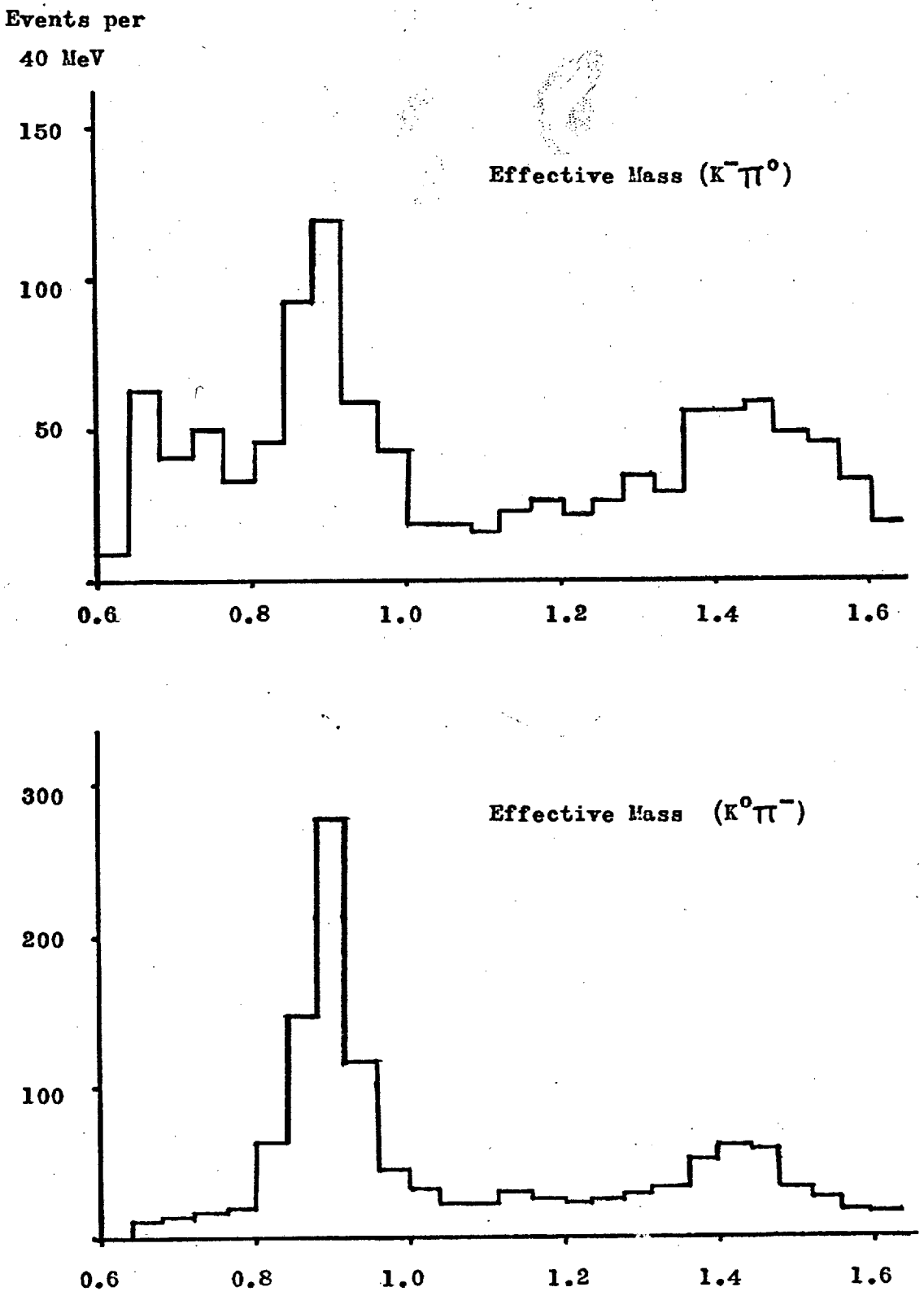
Events per
40 MeV
150
100
50
Effective Mass ($K^-\pi^0$)
0.6
0.8
1.0
1.2
1.4
1.6
300
200
100
Effective Mass ($K^0\pi^-$)
0.6
0.8
1.0
1.2
1.4
1.6

FIGURE 3.2.4

Event is really like this:

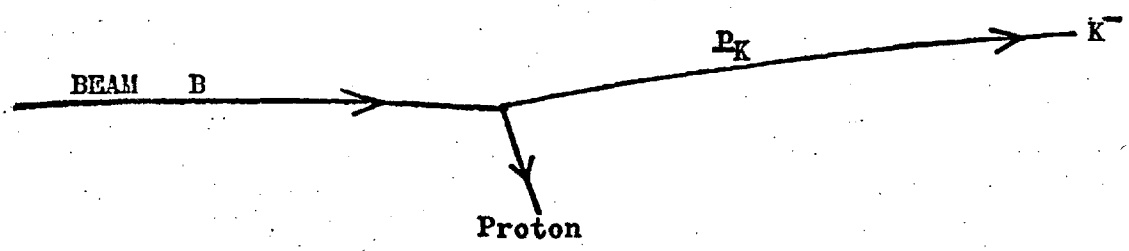

but is fitted to this:

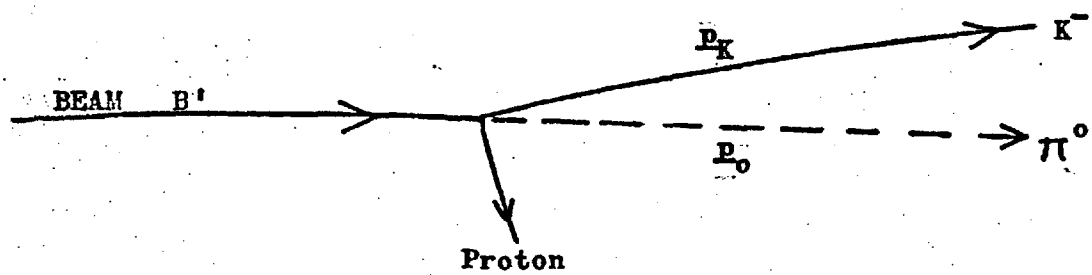

FIGURE 3.2.5

Scatter plot of $m(K^-\pi^0)$ against transverse momentum of π^0.
Each dot = one event.

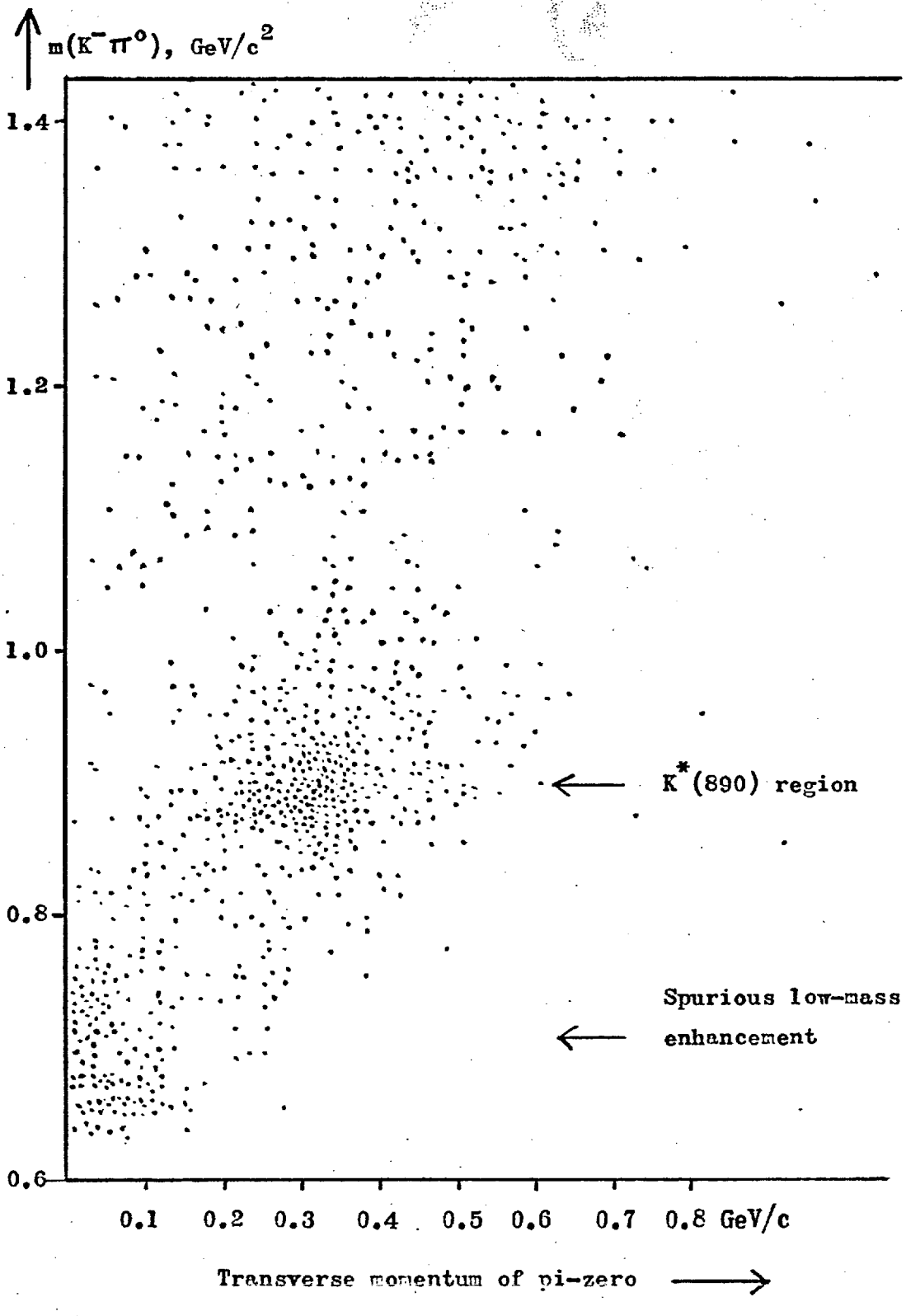

What about the $K^-\pi^0$ effective mass spectrum for these misfitted events? To understand this, we must bear in mind that there will tend to be large measurement errors on the (usually fast) kaon momentum, whereas the proton is usually well-measured. The fitting procedure will adjust p_K and p_π in order to conserve overall energy and momentum. Initially, we have a "missing energy" and "missing momentum" which will be almost equal (since they are presumed to arise from an error in the momentum of a highly relativistic beam) and so the fit will require the pion to be relativistic. Since the kaon is usually moving close to the forward direction, it turns out (approximately) that

$$s(K^-\pi^0) = m_K^2.(1 + p_\pi/p_K) + m_\pi^2.(1 + p_K/p_\pi)$$

which, under the circumstances, cannot be far above threshold.

We have seen that the hypothesis of "misfitted elastics" will explain the presence of a low-mass $K^-\pi^0$ peak in reaction (ii), as well as the low transverse momenta associated with the pions. We should not be surprised that a number of elastic events failed to fit the elastic hypothesis — in fact there is a 1% cut-off in statistical probability for a 4-C fit applied in this experiment, and since we have about 16,000 elastic events in our data there must be about 160 which are falsely rejected because of low probability. Such events may well contribute to the phenomenon we see in fig. 3.2.3.

These misfitted events do not have a strong reflection in the $\pi^0 p$ effective mass spectrum, and it will not be necessary to remove them in order to analyse the $\pi^0 p$ system.

3.3 FEATURES OF THE DATA

The features of the single-pion-production data will serve to illustrate many properties which are, in fact, common to all high-energy hadronic interactions, including the many-body reactions which we will examine later in this work.

The most striking of these features is shown by fig. 3.3.1, the transverse momentum spectra for kaons, pions and for nucleons produced in all of the $K^- p \rightarrow \bar{K}\pi N$ channels. Although the kinematic limit for a transverse momentum is in this case about 2.0 GeV/c, the distributions all peak at about 300 MeV/c. The three parts of fig. 3.3.1 are combined in fig. 3.3.2, which is a logarithmic histogram of the squared transverse momenta. Insofar as the data points on this figure lie on a straight line, the transverse momentum spectrum is described by a Boltzmann-like distribution of the form

$$\frac{d\sigma}{dp_t} = Ap_t \cdot \exp(-p_t^2/q^2)$$

where A and q are constants. The straight line superimposed on fig. 3.3.2 corresponds to a value q = 410 MeV/c.

The incident CMS momentum of the K^- and proton is 2.1 GeV/c, and the longitudinal momenta of the final-state particles will be of this order, the transverse momenta being restricted to a few hundred MeV/c. It is therefore appropriate to display the data according to longitudinal momentum phase space. This technique is discussed in Appendix E.

Histograms of the longitudinal momentum phase space angle ω are given in fig. 3.3.3, and fig. 3.3.4 is a key to their interpretation. Different regions of ω correspond to different peripheral or multiperipheral diagrams, some of which are shown in fig. 3.3.5. Fig. 3.3.3 (a)-(c) can tell us a great deal about the reaction mechanisms for single pion production, and we will discuss them in some detail.

FIGURE 3.3.1

Transverse momentum spectra in single pion production channels

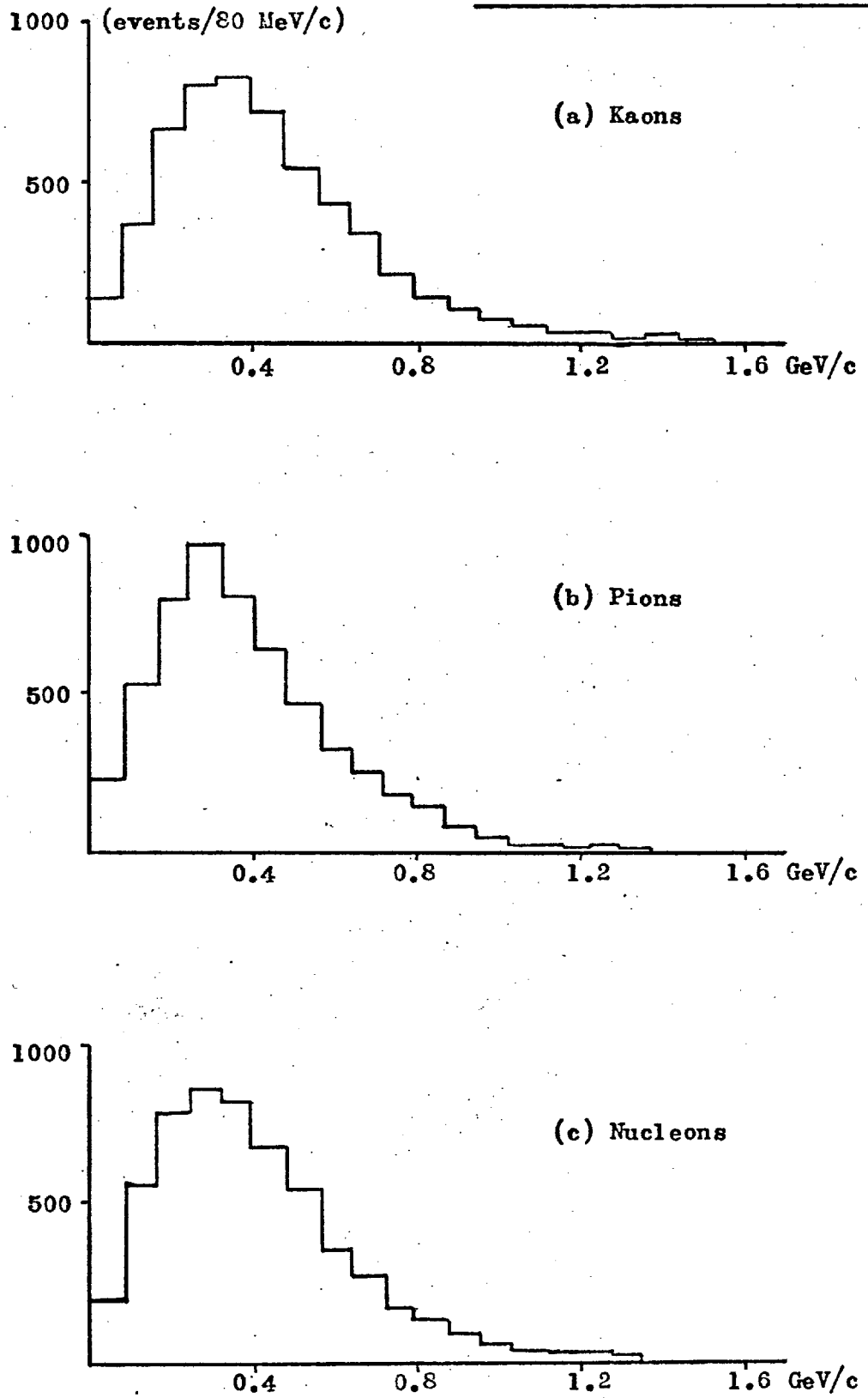

FIGURE 3.3.2

Distribution of p_t^2 for produced particles in all $K^-p \rightarrow \overline{K}\pi N$ channels.

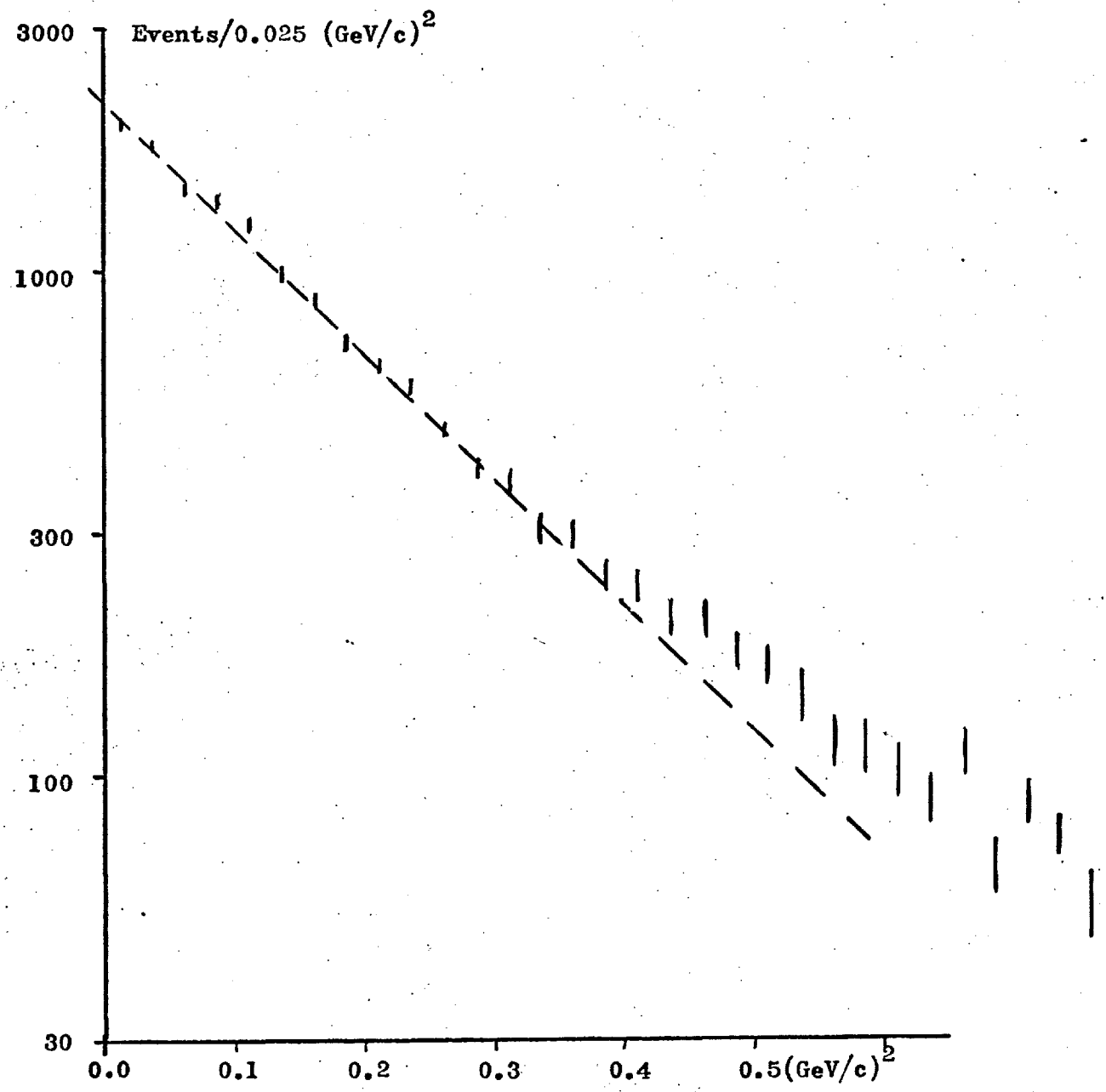

FIGURE 3.3.3 Distributions of "LPS" angle ω for the $K^-p \rightarrow \bar{K}\pi N$ reactions.

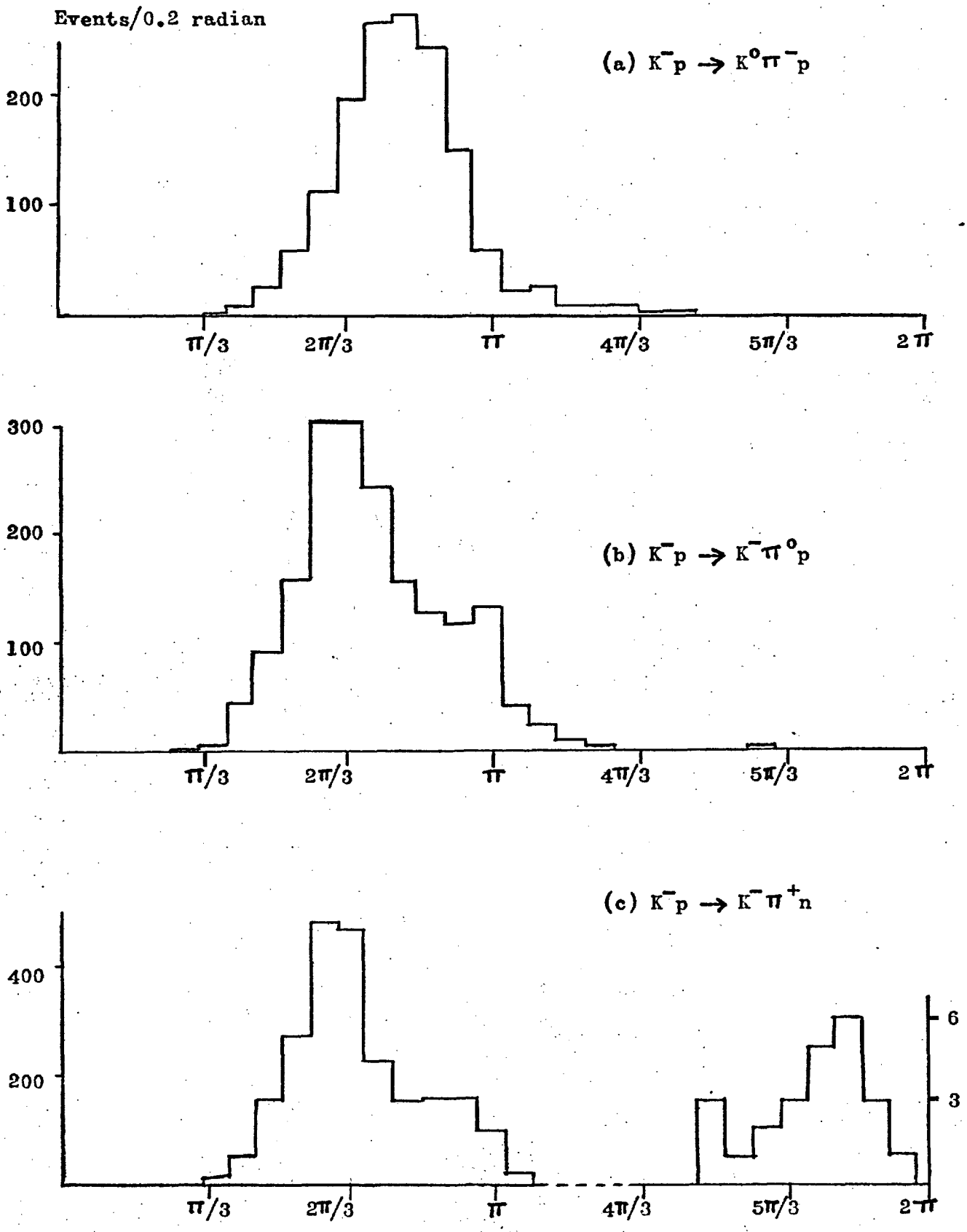

FIGURE 3.3.4 The Longitudinal Momentum Phase Space: definition of ω angle.

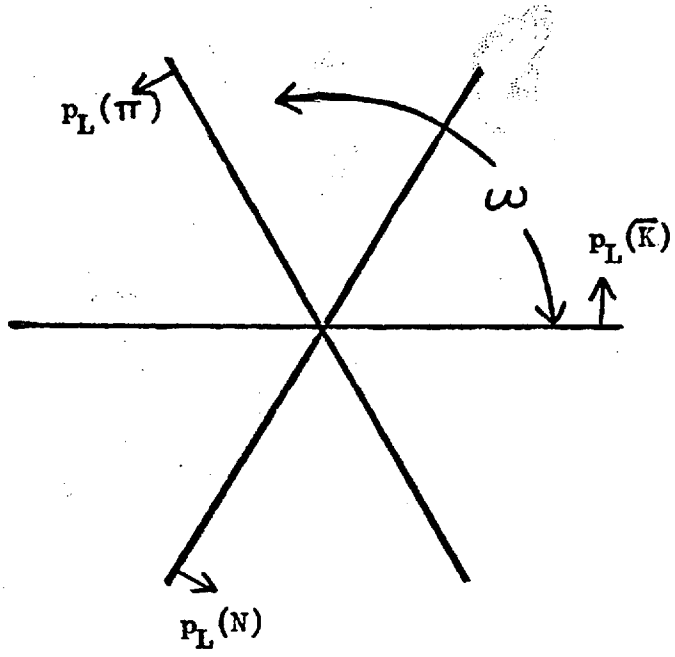

FIGURE 3.3.5 Peripheral Exchange diagrams referred to in the text.

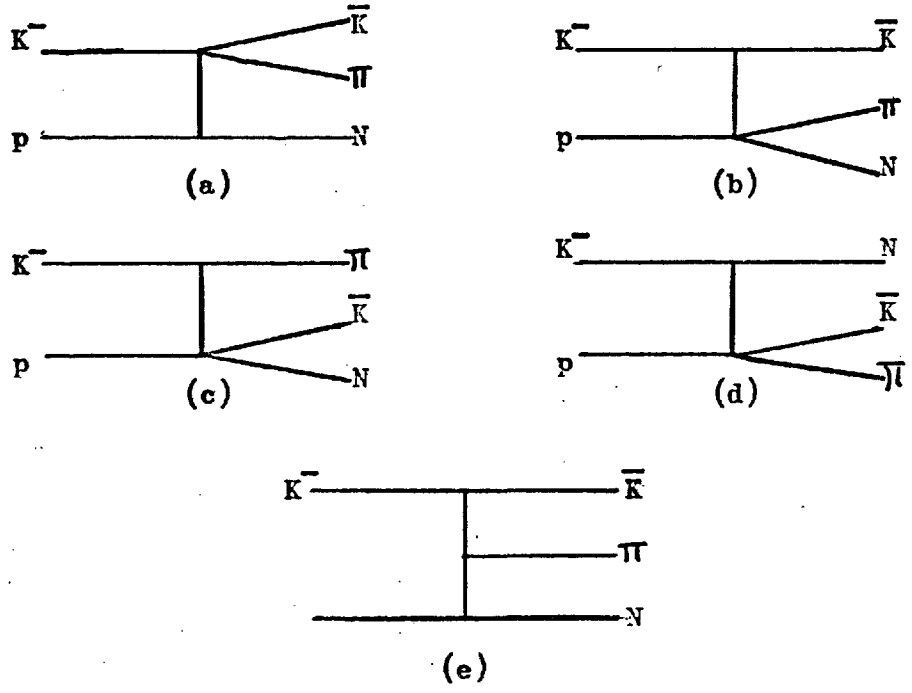

$K^- p \rightarrow K^0 \pi^- p$

These events, in fig. 3.3.3(a), are mostly in the third sextant of the ω-plot; this corresponds to the peripheral process of fig. 3.3.5(a). The spill-over into the second sextant indicates that the pion can often be associated with the nucleon, as in fig. 3.3.5(b).

The small number of events in the fourth sextant reflects the rarity of strange meson exchange (fig.3.3.5(c)). The absence of events elsewhere in the plot can also be explained in terms of the peripheral model.

$K^- p \rightarrow K^- \pi^0 p$

Comments similar to those above apply also to this reaction, with the difference that here the second sextant (fig. 3.3.5(b)) contains a much larger proportion of events.

$K^- p \rightarrow K^- \pi^+ n$

The ω-distribution for this channel is similar to that for $K^- p \rightarrow K^- \pi^0 p$, but has considerably more events at and below the point $\omega = 2\pi/3$.

We notice that the fourth sextant of this distribution is almost empty; this is understandable from fig. 3.3.5(c), which for this channel would involve an "exotic" double charge on the exchanged particle. A peculiarity of this channel is that a few events occur with high values of ω, i.e. in the region corresponding to fig. 3.3.5(d); in the right-hand part of fig. 3.3.3(c) the vertical scale has been expanded to make them clear. The peripheral model could only explain such events by the exchange of an exotic S=+1 baryon, and we consider it more probable that the events are misfits.

In all three reactions, it is clear that baryon exchange and strangeness exchange tend to be suppressed in comparison to the exchange of B=S=0 objects. That is to say, the most important

multiperipheral graph is that of fig. 3.3.5(e). Figs. 3.3.5(a) and (b) are limiting cases of this, and we have seen that the former dominates reaction (i) whereas the latter is also very important in reactions (ii) and (iii).

We have so far said nothing concerning inelastic diffraction, which will be the principal subject of this work. We will use the terms "inelastic diffraction" and "Pomeron exchange" interchangeably, the Pomeron being essentially the same object which is predominantly responsible for high-energy elastic scattering. We will defer detailed discussion of the Pomeron's properties until Chapter 7, but in the meantime we will make frequent reference to the better known ones.

There is strong evidence (the "Gribov-Morrison Rule", Ref. 5.5) that when a particle is diffractively dissociated, the produced system must belong to the same spin-parity series as the original particle. Any $\overline{K}\pi$ system must have natural spin-parity, and since the kaon is a pseudoscalar, it follows that the dissociation $K^- \rightarrow \overline{K}\pi$ cannot be diffractive. For this reason we will say no more about the process of fig. 3.3.5(a). $K^*(890)$ production, which is dominant for such events, is analysed in Ref. 1.10.

Events where the pion is associated with the nucleon will be analysed in the next section; it is significant that these events occur most copiously without charge exchange, and we shall show that their dominant production process is Pomeron exchange.

3.4 THE πN SYSTEMS

We established in the previous section that peripheral production of low-mass πN systems occurs abundantly in our data. In figures 3.4.1 (a)-(c) the πN effective mass spectra are shown for reactions (i) to (iii).

The Production Mechanisms

We will distinguish the following processes which may lead to the production of low-mass πN systems:

(a) The production of $I = 3/2$ πN systems. In order to conserve I-spin at the baryon vertex this would have to come about through isovector exchange from the kaon.

(b) The production of $I = 1/2$ πN systems by isovector exchange from the kaon.

(c) The production of $I = 1/2$ πN systems by isoscalar exchange. To conserve I-spin at the kaon vertex this can only occur in reactions (ii) and (iii).

We may describe these three processes by three independent amplitudes, and because we are in the resonance region these will be strong functions of the πN effective mass. An I-spin analysis of the $K^- p \rightarrow \bar{K}\pi N$ reactions is given in Appendix D, and in terms of the notation used there the processes listed above correspond to the three F_T^B amplitudes.

Ideally, we should like to separate out the contributions of these different amplitudes and study them independently; we are particularly interested in the amplitude for process (c), where the exchanged object is liable to be the Pomeron. However, to disentangle the contributions of the different amplitudes (over any region of the phase space) will require five quantities (three magnitudes and two relative phases) to be obtained from the three partial cross-sections. This is not possible.

FIGURE 3.4.1

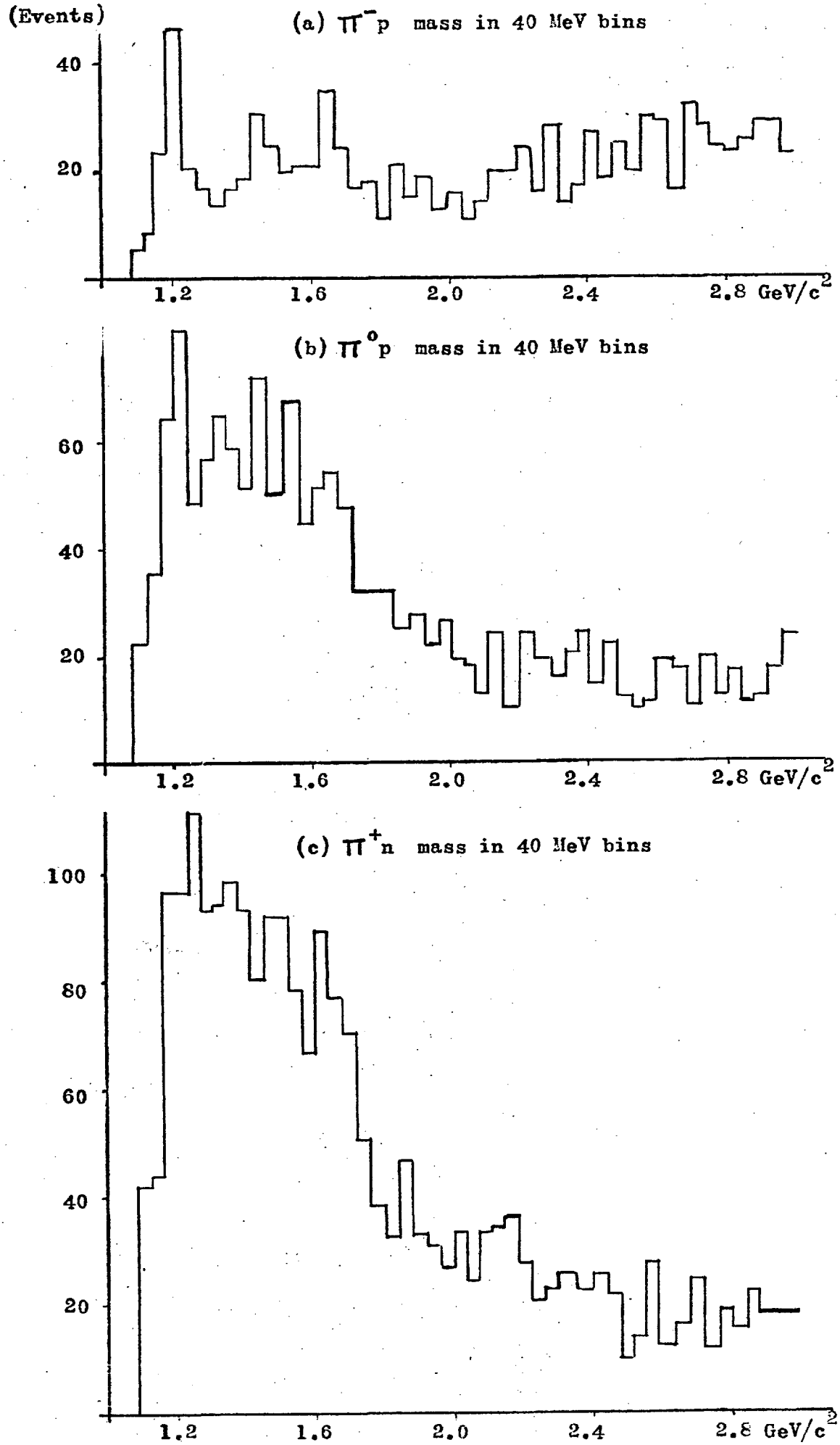
(Events)
(a) $\pi^- p$ mass in 40 MeV bins
40
20
1.2
1.6
2.0
2.4
2.8 GeV/c^2
(b) $\pi^0 p$ mass in 40 MeV bins
60
40
20
1.2
1.6
2.0
2.4
2.8 GeV/c^2
(c) $\pi^+ n$ mass in 40 MeV bins
100
80
60
40
20
1.2
1.6
2.0
2.4
2.8 GeV/c^2

Nevertheless, we shall see that conclusions can be drawn concerning the relative importance of processes (a) to (c).

$\underline{K^- p \rightarrow K^0(\pi^- n)}$

If we look now at fig. 3.4.1(a), i.e. the $\pi^- p$ mass spectrum, we see a clean $\Delta^0(1236)$ enhancement and also two less significant peaks at about 1460 and 1660 MeV/c^2. The 1660 MeV/c^2 bump could be due to the $\Delta(1650)$ or perhaps the $\Delta(1670)$ resonance; but there is no established Δ resonance between 1236 and 1650 MeV/c^2 which might account for the enhancement at 1460 MeV/c^2. It therefore seems probable that there is a significant amout of $I = \frac{1}{2}$ $\pi^- p$ production in the 1460 MeV/c^2 region — perhaps the "Roper" resonance.

Above about 2.0 GeV/c^2, the $\pi^- p$ spectrum begins to rise slowly. This is in fact a reflection of the strongly-produced K^* resonances in the $K^0\pi^-$ system, and so far as the $\pi^- p$ spectrum is concerned it is a non-resonant background which must have both I = 3/2 and I = 1/2 components.

We can say, then, that process (a) plays a large part in this reaction. Process (b) contributes, to a lesser extent, at around 1460 MeV/c^2. Above about 2.0 GeV/c^2 both processes will give a non-resonant contribution. The bump at 1660 MeV/c^2 cannot with certainty be put down to one process or the other.

$\underline{K^- p \rightarrow K^-(\pi N)^+}$

It is mentioned in Appendix D that the ratio of the cross-sections $\sigma(\pi^+ n)/\sigma(\pi^0 p)$ is an indicator of the I-spin of the $(\pi N)^+$ systems. This ratio (with statistical errors) is displayed in fig. 3.4.2 as a function of the $(\pi N)^+$ effective mass. It is immediately clear from this figure that the $(\pi N)^+$ systems are predominantly of I-spin $\frac{1}{2}$; the ratio is always closer to 2 than to 0.5, and only comes down to 1 at high values of the mass, where we might expect to find a statistical mixture of the two I-spins.

FIGURE 3.4.2

$$\frac{\sigma(\pi^+ n)}{\sigma(\pi^0 p)} \quad \text{in } K^- p \rightarrow K^-(\pi N)^+$$

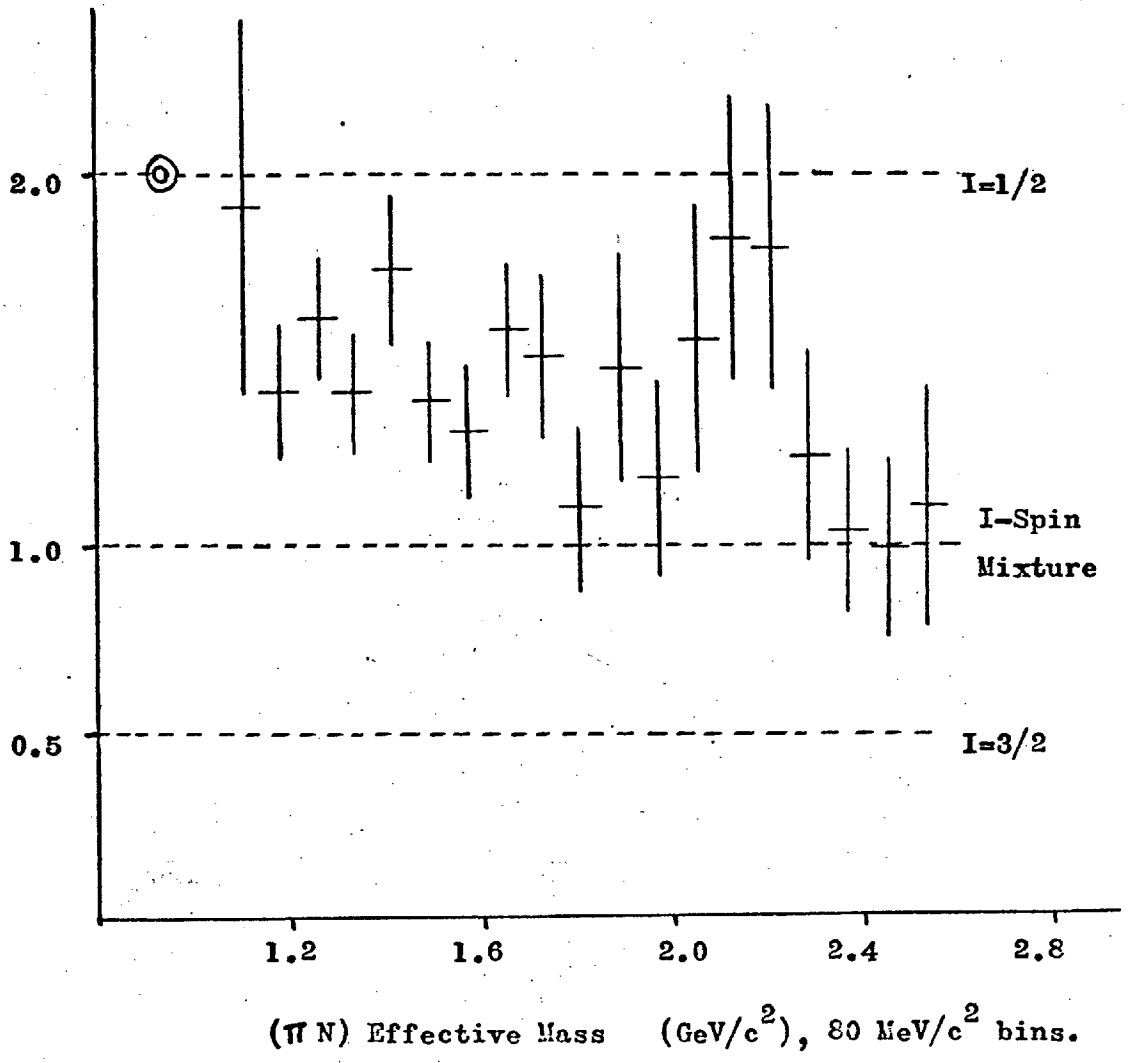

The double circle represents the (unphysical) point where $m(\pi N) = m_p$. It is reasonable to suppose that our data points should extrapolate back to $I=\frac{1}{2}$ at this point. It would clearly be possible to draw a smooth curve from this point down through the data points (bearing in mind their errors) and tending asymptotically to the central dotted line. The only significant deviation from such a curve would be at around 2160 MeV/c^2, where the data points rise up towards the $I=\frac{1}{2}$ line. This is perhaps a hint of $N^*(2190)$ production.

The $(\pi N)^+$ mass spectra (figs. 3.4.1 (b) and (c)) show some important features. The only bump which can be clearly identified as a resonance is that at the $\Delta^+(1236)$ mass (in both spectra), but above this, and extending up to about 1800 MeV/c^2, is a broad and rather ragged enhancement (again in both spectra). It is relevant that the numbers of events involved are much greater than in the case of the $\pi^- p$ spectrum.

Qualitative Conclusions

The $I = \frac{1}{2}$ $\pi^- p$ production depends on the $F_1^{\frac{1}{2}}$ amplitude of Appendix D, and from eqns. D15–D17 we see that the contribution of this amplitude to $\pi^0 p$ production (or $\pi^+ n$ production) will be about one-eighth (or a quarter) of the contribution to the $\pi^- p$ production cross-section. (Assuming that interference effects are not very strong.) Now, the $\pi^- p$ $I=\frac{1}{2}$ cross-section is small below about 2.0 GeV/c^2, so the corresponding contributions to the $(\pi N)^+$ cross-sections are likely to be very small. In other words, process (b) must be relatively insignificant in reactions (ii) and (iii).

The dominance of $I=\frac{1}{2}$ in reactions (ii) and (iii) must, therefore, arise from the occurence of process (c).

Quantitative Results

We have examined the consequences of assuming that process (b) can in fact be ignored in all three reactions. As shown in Appendix D, we can then extract from our data the contribution of process (c) alone. This can be written

$$\sigma_c = \sigma(ii) + \sigma(iii) - 3\sigma(i)$$

and is plotted (with statistical errors) in figure 3.4.3. This quantity ought, of course, to be positive over the entire mass range; the fact that it becomes negative at high values of the (π N) mass is an indication of the failure of our assumption.

Figure 3.4.3 shows no clear resonance structure. We can say only that process(c) produces π N systems of predominantly low effective mass; the spectrum consists of a broad enhancement (width at half height is about 480 MeV/c^2) which peaks at about 1360 MeV/c^2. The number of events with m(π N) less than 2.0 GeV/c^2 in fig. 3.4.3 is 1,281; in view of the approximation we have made, this must be regarded as merely a lower limit on the number of events in the data corresponding to process (c).

In order to estimate cross-sections for the three processes, it is more useful to assume that there is no interference between the three amplitudes describing them. Although this would be a most unreliable approximation at any particular value of the π N effective mass, it is not likely to be far wrong when we integrate the amplitude over the whole of phase space. This is because the phases of the amplitudes are likely to vary considerably across the π N resonance region.

Again using results from Appendix D, we have calculated numbers of events and cross-sections for processes (a)-(c) in the approximation of "no interference", and they are tabulated in Figure 3.4.4.

FIGURE 3.4.3

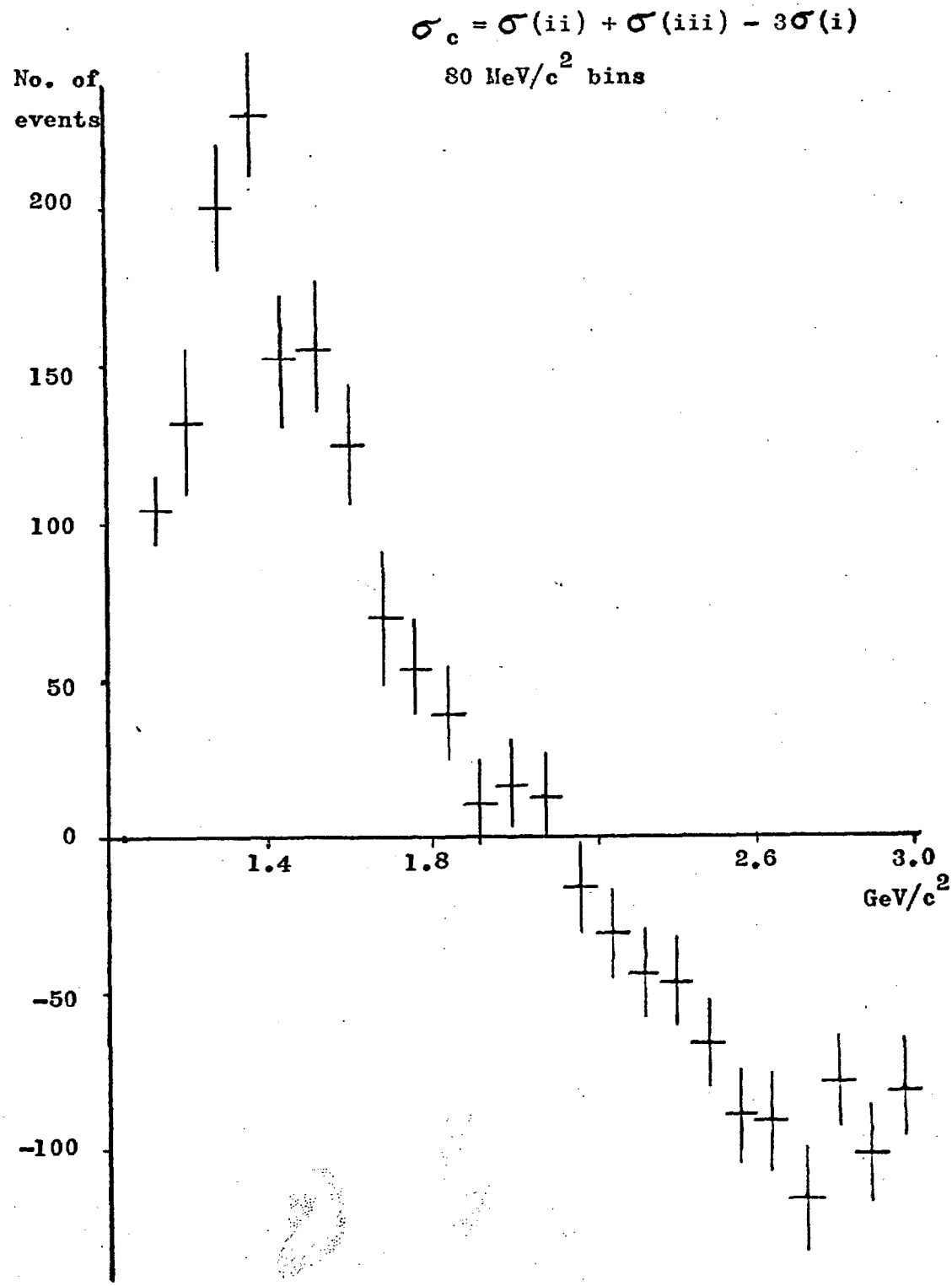
$\sigma_c = \sigma(ii) + \sigma(iii) - 3\sigma(i)$
80 MeV/c^2 bins
No. of events
200
150
100
50
0
-50
-100
1.4
1.8
2.6
3.0
GeV/c^2

FIGURE 3.4.4

Nos. of events and cross-sections (with $m(\pi N) < 2.0$ GeV/c^2) for reactions (i)-(iii) and processes (a)-(c), in the "no interference" approximation.

	Process (a)	(b)	(c)	Sum
(i) $K^0\pi^-p$	185 (36 μb.)	267 (52 μb.)	—	452 (88 μb.)
(ii) $K^-\pi^0p$	370 (73 μb.)	34 (7 μb.)	659 (128 μb.)	1063 (206 μb.)
(iii) $K^-\pi^+n$	185 (36 μb.)	66 (7 μb.)	1320 (256 μb.)	1571 (305 μb.)
Sum	740 (145 μb.)	367 (65 μb.)	1979 (385 μb.)	

In calculating these results, we have used the individual reaction cross-sections for $m(\pi N) < 2.0$ GeV/c^2. No errors are quoted, since the statistical errors would be considerably less than the uncertainties arising from our assumptions.

t-Distibutions

In figures 3.4.5 and 3.4.6 we show logarithmic t-distributions from the incident K^- to the outgoing kaon. In figure 3.4.5, the data are those for the individual channels, with $m(\pi N)$ less than 2.0 GeV/c^2.

In figure 3.4.6, the t-distributions are those for the three separate production mechanisms listed earlier; they are found by taking linear combinations of the data in figure 3.4.5, i.e. by solving eqns. D30-D32 in Appendix D. This method is based on the assumption that there is no interference between the amplitudes describing these production mechanisms, and its justification was mentioned in the previous subsection.

The first two plots of figure 3.4.6 correspond to the isovector (presumably ρ) exchange processes, and would not be well described by straight lines. Close to t=0, their slopes are small. The data points in the third plot adhere closely to a straight line up to about $-t = 0.4$ GeV^2 ; the line superimposed is an "eyeball" fit, and has slope equal to 6.4 GeV^{-2}.

Process (c), then, gives rise to a steep t-distribution with a slope not much less than that found for elastic scattering in Appendix A. We take this as strong evidence for the diffractive nature of process (c).

FIGURE 3.4.5

Logarithmic t-Distributions for $K^- p \rightarrow \overline{K}(\pi N)$, with $m(\pi N) < 2.0$ GeV/c^2.

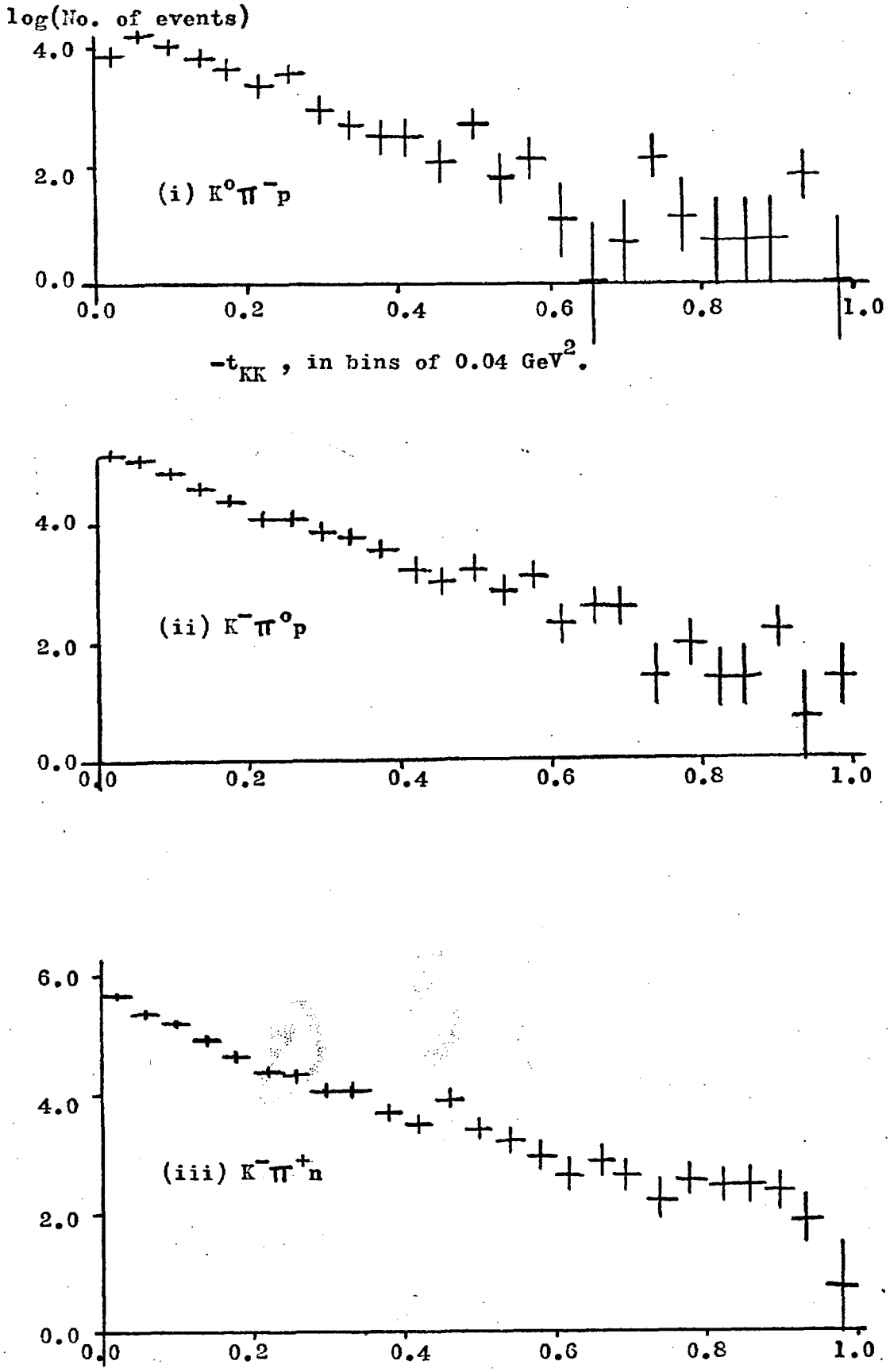

FIGURE 3.4.6

Logarithmic t-Distributions for $K^- p \rightarrow \overline{K}(\pi N)$, separated according to the reaction mechanism according to the "no interference" approximation, with $m(\pi N) < 2.0$ GeV/c^2

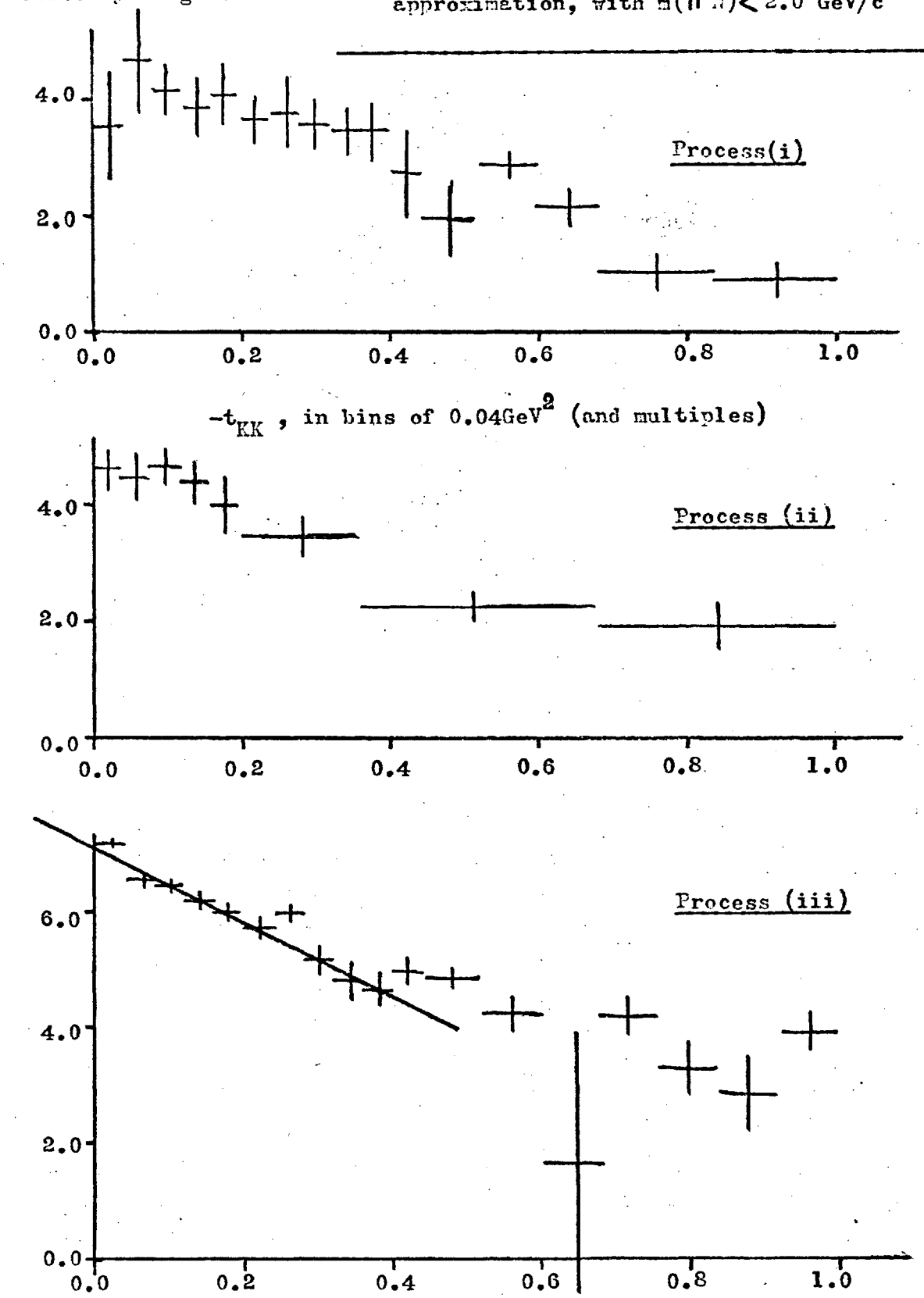

3.5 CONCLUSIONS

We can summarise as follows the results of the previous section:

(i) It is clear from the data that there is abundant peripheral production of low-mass $(\pi N)^+$ systems.

(ii) These arise predominantly from the exchange of an isoscalar object; we deduce this from the facts that the cross-section for charge exchange ($K^- p \rightarrow \bar{K}^0 (\pi N)^0$) is small and that the $(\pi N)^+$ systems have an average I-spin not much greater than $\frac{1}{2}$.

(iii) Isovector exchange also occurs (to a lesser extent) and gives rise to both I=3/2 and I=1/2 (πN) systems.

(iv) The $(\pi N)^+$ mass spectrum resulting from isoscalar exchange does not have any clear resonant structure; rather, we find a broad enhancement stretching from 1300 to 1800 MeV/c^2. However, it is impossible to make an exact analysis of this production process in isolation from the competing isovector exchange processes, and this conclusion depends on an assumption which can only be approximately true.

(v) Isoscalar exchange accounts for roughly 50% of the total cross-section for $K^- p \rightarrow K^- \pi^+ n$, and 33% of that for $K^- p \rightarrow K^- \pi^0 p$. (Numbers from results in figure 3.4.4).

(vi) The t-distribution for this isoscalar exchange process is well descibed by an exponential at lower values of t, and the logarithmic slope is about 6.4 GeV^{-2}.

We can conclude from all this that we are observing the diffractive dissociation of the incident proton; i.e. that Pomeron exchange is responsible. Note that this conclusion depends on a definition of the Pomeron which is based on its empirical properties

alone. These properties are well-established in the literature, and are discussed in Chapter 7.

One such property is the approximate constancy (with beam momentum) of the cross-section for any Pomeron-exchange reaction. Now, at very high energies, we expect Pomeron exchange to dominate the $K^-p \to K^-(\pi N)^+$ cross-sections, since the amplitudes for reggeon exchange will tend to zero. If the Pomeron exchange cross-section is in fact constant, and equal to that which we find at 10 GeV/c (and given in figure 3.4.4) then the asymptotic cross-sections are predicted to be about 0.13 mb. for $K^-p \to K^-\pi^0p$ and 0.26 mb. for $K^-p \to K^-\pi^+n$.

From recent work on $pp \to p\pi N$ reactions (Ref. 3.2), and making use of the factorisability of the Pomeron exchange amplitude, it has been calculated (in Ref. 3.1) that the asymptotic $K^-p \to K^-(\pi N)^+$ cross-sections are 0.11 and 0.22 mb. The predictions of the previous paragraph are in fairly good agreement with this.

Further information on the role of Pomeron exchange in these reactions appears in refs. 1.21 and 3.1, where the data is fitted to models which incorporate inelastic diffraction as well as the other possible reaction mechanisms. In the first of these ("Application of the Veneziano Model with pion and Pomeron exchange to the reaction $K^-p \to nK^-\pi^+$ at 10 GeV/c"), the proportion of the cross-section due to Pomeron exchange is found to be 25.5% — rather less than the 50% which we find.

In Ref. 3.1 ("Dual + Pomeron Analysis of $K^\pm p \to K^\pm\pi^0p$"), on the other hand, the proportion of Pomeron exchange is found as 55%, to be compared with our 33%.

We need not be too concerned by these discrepancies, since the models used in Refs. 1.21 and 3.1 are at best approximate and are used more to test the versatility of the Veneziano model than to extract numbers from our data. Since their results straddle ours in (v) above, we consider our results as being confirmed by them.

In summary: Our examination of the $K^- p \rightarrow \bar{K}\pi N$ data has shown up the limitations of the experiment (in sections 3.1 and 3.2), the peripheral character of high-energy scattering (in section 3.3) and many of the ideas and techniques which we find useful. In particular, we have been able to show that a high proportion of the cross-section for single pion production can only be accounted for by Pomeron exchange.

References (3)

Ref. 3.1 Dual + Pomeron Analysis of $K^{\pm} p \rightarrow K^{\pm}\pi^0 p$,
Kajantie and Papageorgiou,
CERN preprint TH.1170 (1970)

Ref. 3.2 H. Satz,
Nuclear Physics B14, 366 (1969)

CHAPTER 4

DOUBLE PION PRODUCTION

The possible $K^-p \rightarrow \bar{K}\pi\pi N$ reactions are:

(i) $K^-p \rightarrow K^-\pi^+\pi^-p$

$K^-p \rightarrow K^-\pi^0\pi^0p$

(ii) $K^-p \rightarrow K^0\pi^-\pi^0p$

$K^-p \rightarrow K^-\pi^+\pi^0n$

(iii) $K^-p \rightarrow K^0\pi^+\pi^-n$

and $K^-p \rightarrow K^0\pi^0\pi^0n$

where only the numbered reactions can be fitted to events in the bubble chamber. In the case of reaction (i), these are 4-C fits; in the other two cases they are 1-C fits which can only be made when the decay of the K^0 is seen and measured.

4.1 THE DATA

The numbers of fits in our data sample, together with other information, is tabulated in figure 4.1.1. In reactions (ii) and (iii) there are few ambiguous fits and the sum of the hypothesis weights is not much less than the total number of fits.

In reaction (i), on the other hand, there are roughly 1600 ambiguous fits. Most of these ambiguities arise from the difficulty of distinguishing between the two negative tracks, the K^- and the π^-. Thus, both hypotheses refer to the same channel, and the sum of the hypothesis weights is close to the actual number of events.

The cross-sections are quoted with a statistical error only. We can trust reaction (i) (4-C fits) and also reaction (ii) (fitting a π^0), but in reaction (iii) the missing mass is large and so, very often, is its error. It is often impossible to distinguish between $K^-p \rightarrow K^0\pi^+\pi^-n$ and $K^-p \rightarrow K^0\pi^+\pi^-\pi^0n$, and this no doubt leads to some contamination and loss of events in our data.

FIGURE 4.1.1

Cross-sections, etc., for double pion production.

	Reaction (i)	(ii)	(iii)
Number of fits.	6892	1526	801
Sum of hypothesis weights.	6069	1520	793
Probable number of events, allowing for unseen K^o decays.	6069	5680	2478
Cross-section, with statistical error.	1.18 mb. ± 3%	1.10 mb. ± 4%	0.48 mb. ± 4½%

4.2 POMERON EXCHANGE

Under what circumstances can inelastic diffraction give rise to a $\overline{K}\pi\pi N$ final state? Since Pomeron exchange cannot lead to the dissociation $K^- \rightarrow (\overline{K}\pi)^-$, for reasons discussed in the previous chapter, the only possibilities are the following:

(a) $K^- \rightarrow K^-\pi^+\pi^-$ in reaction (i),
(b) $K^- \rightarrow K^0\pi^-\pi^0$ in reaction (ii) and
(c) $p \rightarrow p\pi^+\pi^-$ in reaction (i).

We show experimental $K^-\pi^+\pi^-$, $K^0\pi^-\pi^0$ and $p\pi^+\pi^-$ effective mass spectra in figure 4.2.1, and for comparison figure 4.2.2 contains $K^0\pi^+\pi^-$, $p\pi^-\pi^0$ and $n\pi^+\pi^-$ spectra in the same region. No selections have been applied to any of this data. The vertical axes on these histograms are calibrated with both the cross-sections (corrected, where necessary, for unseen K^0 decays) and the numbers of events per bin of width 80 MeV/c^2 .

The $(K\pi\pi)^-$ mass spectra of figure 4.2.1 (a) and (b) are very similar to one another, both in shape and in cross-section. The Q enhancements just below 1.4 GeV/c^2 dominate these, and the L enhancements are also visible at about 1.8 GeV/c^2. On the other hand, figure 4.2.2 (a), the $K^0\pi^+\pi^-$ mass spectrum, contains far fewer events and no structure similar to the Q and L peaks.

Figures 4.2.2 (b) and (c), i.e. the $(N\pi\pi)^0$ mass spectra, both show a low cross-section with no outstanding enhancements. In contrast, figure 4.2.1(c) (the $p\pi^+\pi^-$ spectrum) contains a large number of events even close to threshold, and there is a clear peak at around 1.7 GeV/c^2 which may well be due to resonance production.

Where Pomeron exchange can occur, then, we see that there is production of $(K\pi\pi)^-$ and $(N\pi\pi)^+$ systems with effective masses which are not far above the respective thresholds. This is a very strong effect, and suffices to explain why the total cross section for reaction (iii) (where no Pomeron exchange can occur) is less than half that for reaction (i) or (ii).

FIGURE 4.2.1

Effective Mass Spectra, in bins of 80 MeV/c^2.

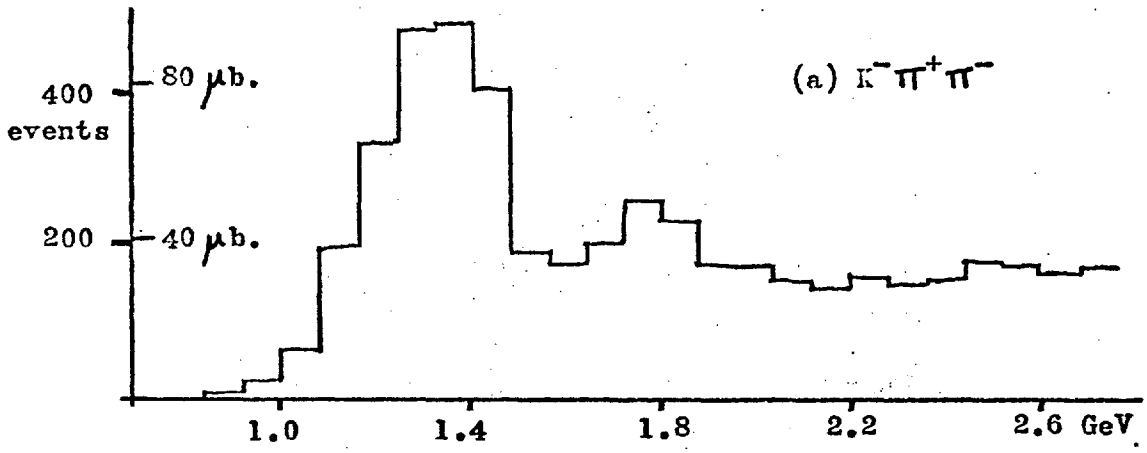

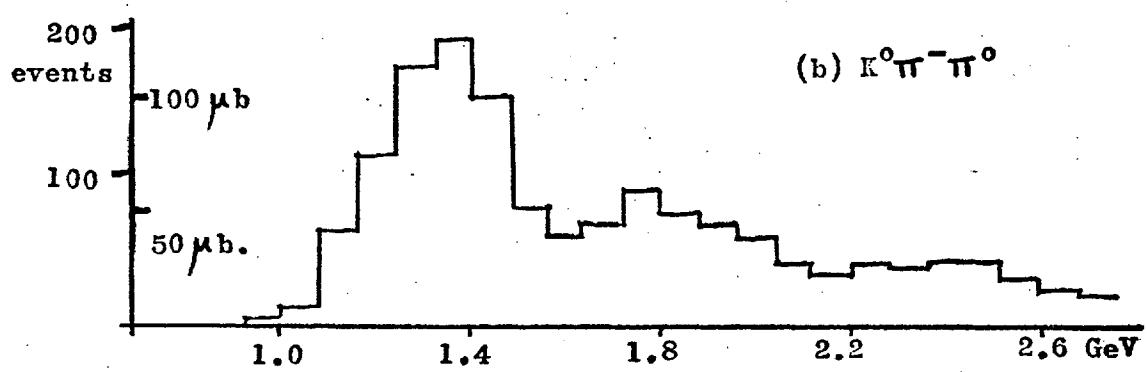

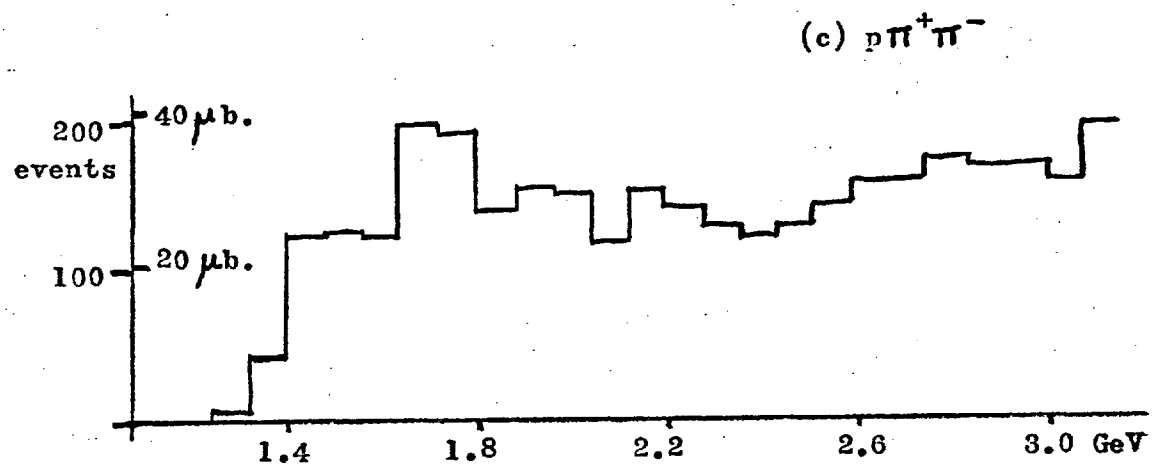

FIGURE 4.2.2 Effective Mass Spectra, in bins of 80 MeV/c^2

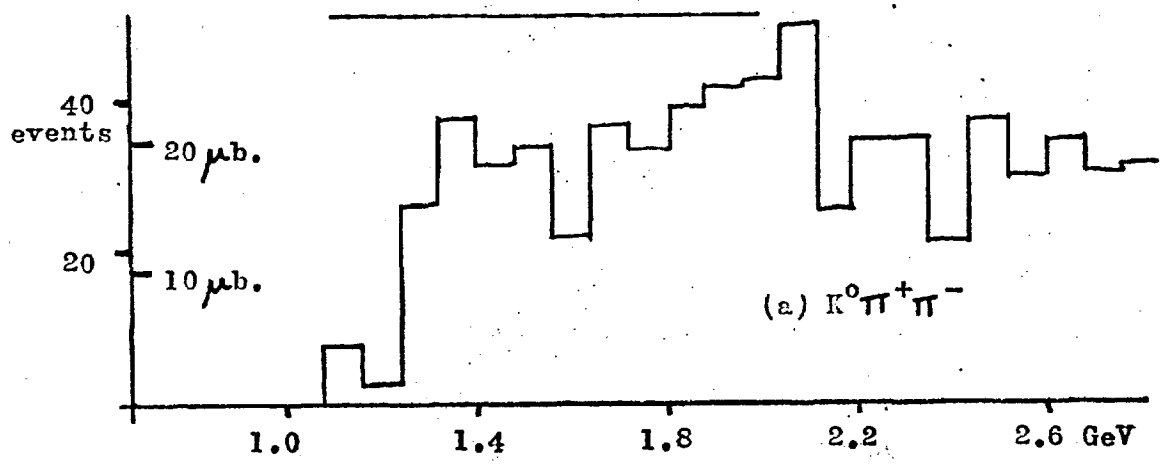

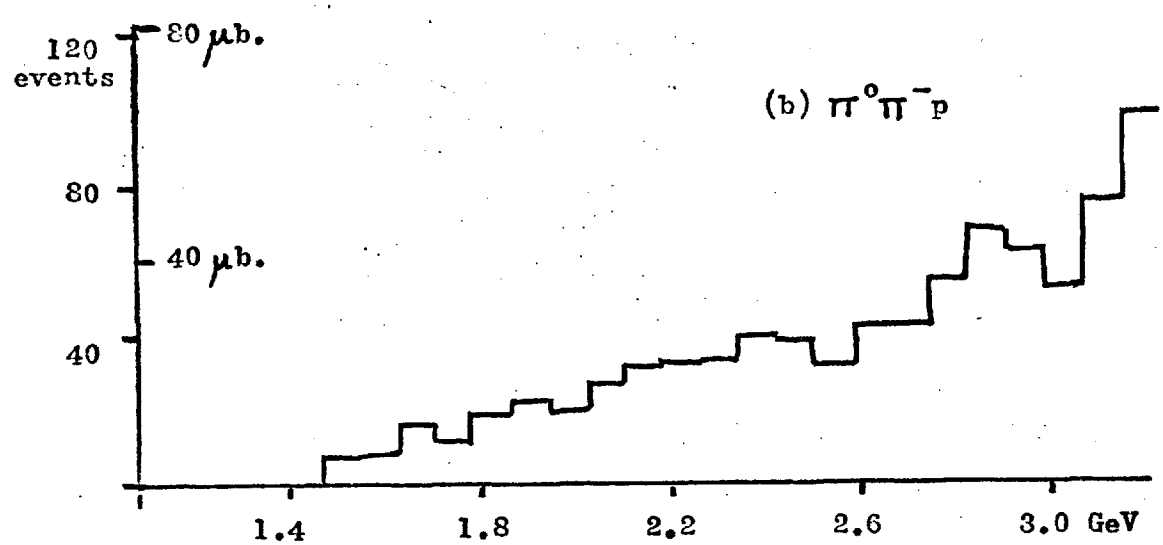

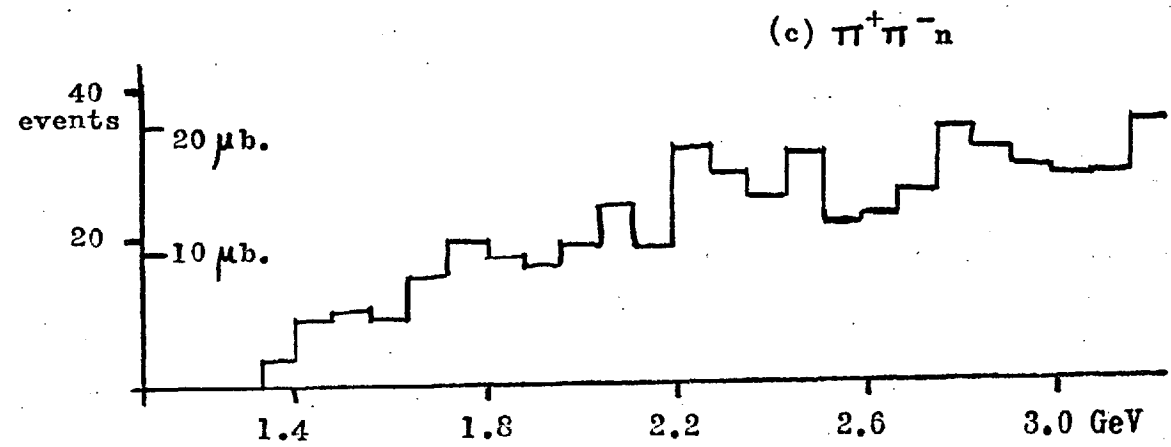

We can remove most of the "background" from figs. 4.2.1 (a) and (b) by applying the following cuts to our data:

For process (a): $-t_{pp} < 0.6$ GeV^2, and
$m(p\pi^+)$ not in the $\Delta^{++}(1236)$ mass region.

For process (b): $-t_{pp} < 0.6$ GeV^2, and
$m(p\pi^-)$ not in the $\Delta^{0}(1236)$ mass region, and
$m(p\pi^0)$ not in the $\Delta^{+}(1236)$ mass region.

The cuts on t_{pp} leave almost all events which involve Pomeron exchange from the proton, whilst removing the majority of the other events. The $\Delta(1236)$ resonance is produced abundantly (in the charge states indicated) and it is as well to eliminate it here since it is incompatible with Pomeron exchange from the proton.

The events selected by the above criteria have the $\bar{K}\pi\pi\pi$ effective mass spectra of figure 4.2.3 (a) and (b). These show very clean Q and L enhancements, and only a small proportion of the events have high (> 2.5 GeV/c^2, say) values of this effective mass. We also notice that the two spectra are very similar in shape to one another.

The dissociation of the proton, i.e. process (c), poses a more difficult problem. In figure 4.2.4 we plot the $p\pi^+\pi^-$ effective mass spectrum, with $-t_{KK} < 0.6$ GeV^2 and with $K^{*o}(890)$ events removed from the sample. There are recognisable resonance peaks in this spectrum, but the background is greater than in the $\bar{K}\pi\pi\pi$ case and the spectrum extends higher above threshold. This indicates that the simple cuts we have applied are not sufficient to isolate the diffractively produced $p\pi\pi\pi$ systems.

Certain features of fig. 4.2.4 are worthy of comment. There are significant peaks close to 1460, 1720 and 2200 MeV/c^2. These may well correspond to the $N^*(1470)$, $N^*(1690)$ and $N^*(2190)$ resonances, as indicated over the histogram. However, the width of our 1460 MeV/c^2 peak is much less than the width established for that resonance. Of course, the masses and widths "established" for these N^*'s are obtained by partial wave analyses of formation experiments, and it is not obvious that they should have a similar

FIGURE 4.2.3

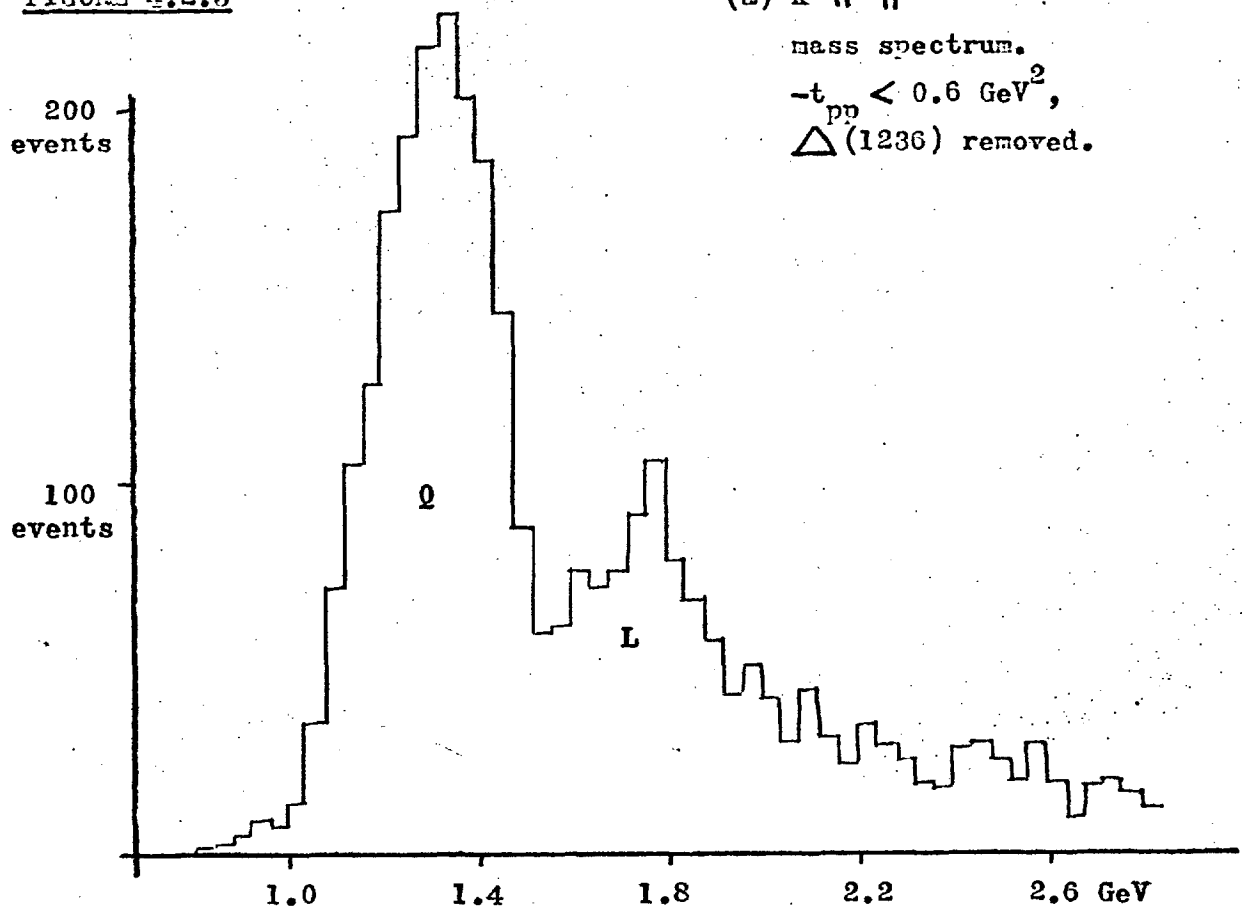
(a) $K^-\pi^+\pi^-$
mass spectrum.
$-t_{pp} < 0.6$ GeV^2,
Δ(1236) removed.
200 events
100 events
Q
L
1.0
1.4
1.8
2.2
2.6 GeV

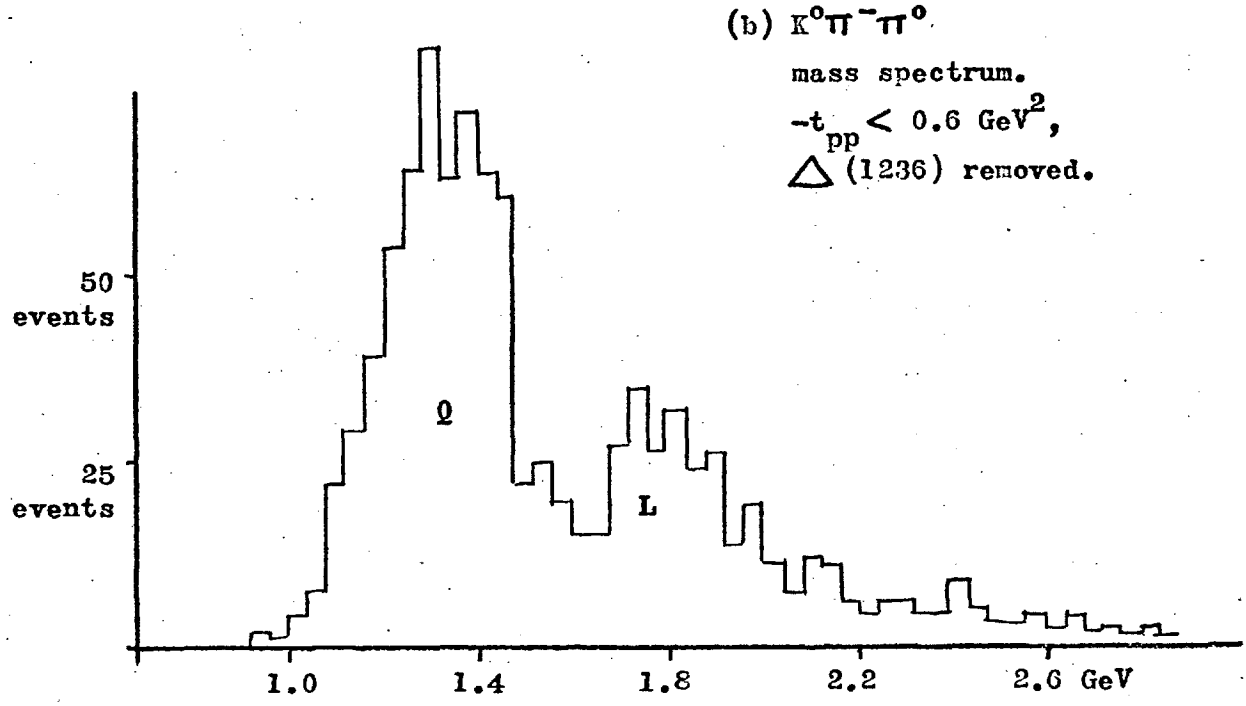
(b) $K^0\pi^-\pi^0$
mass spectrum.
$-t_{pp} < 0.6$ GeV^2,
Δ(1236) removed.
50 events
25 events
Q
L
1.0
1.4
1.8
2.2
2.6 GeV

FIGURE 4.2.4

$p\pi^+\pi^-$ effective mass spectrum,
with $t_{KK} < 0.6$ GeV^2,
and $K^*(892)$ events removed.

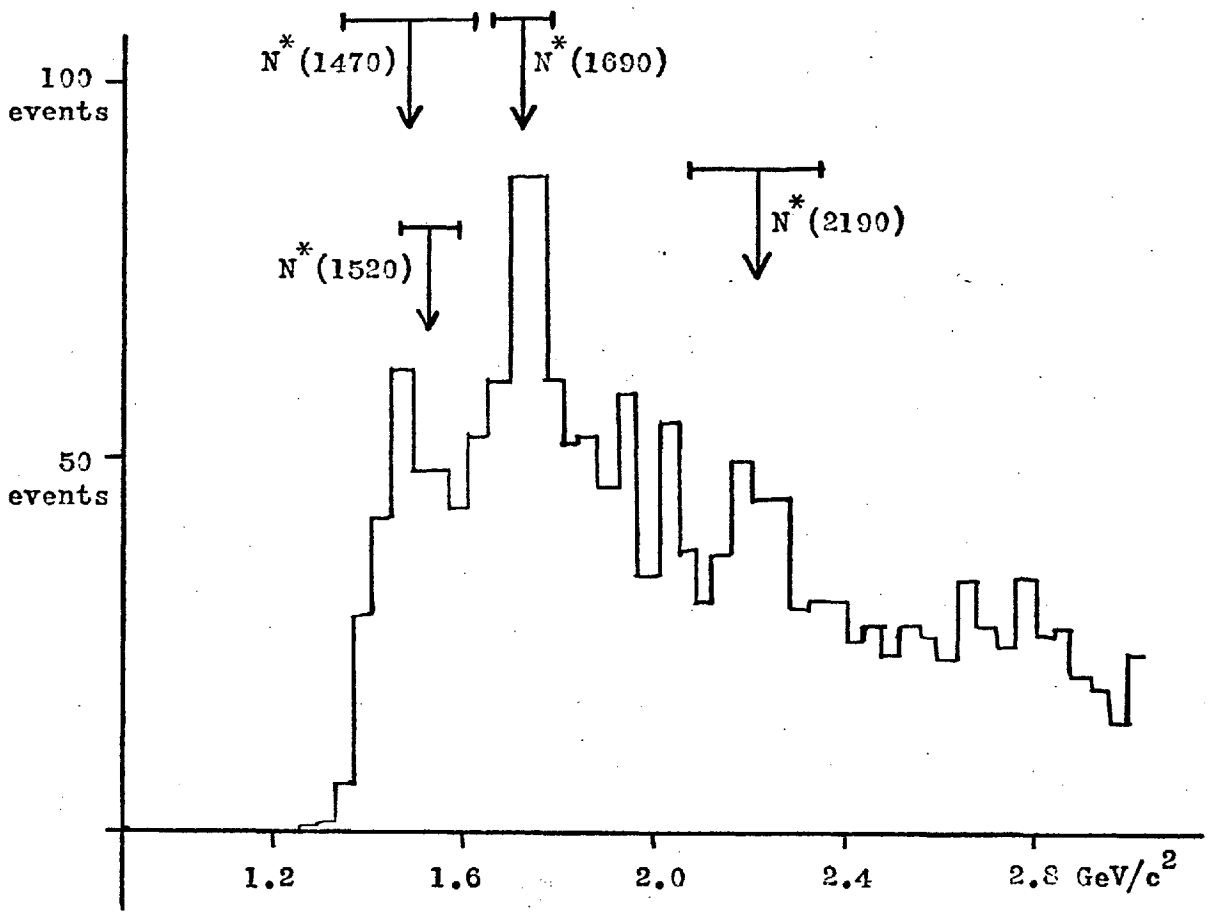

appearance in production. It is perhaps equally likely that the $N^*(1520)$ (also indicated in the figure) is responsible for the first peak. If we assume that the $p\pi^+\pi^-$ mass spectrum is dominated by the resonances we have suggested, an interesting pattern emerges. The spin-parities of the $N^*(1520)$, $N^*(1690)$ and $N^*(2190)$ are $(3/2)^-$, $(5/2)^+$ and $(7/2)^-$ respectively, i.e. they belong to the same spin-parity series as the proton. In fact, they can be regarded as Regge recurrences of the proton.

It is then very tempting to suggest that diffractive dissociation arises from the excitation of the incident particle to some higher spin state. This is essentially the Gribov-Morrison rule (Ref. 5.5). Applying this idea to the Q and L enhancements, we surmise that they are resonances with $J^P = 1^+$ and 2^- respectively, and can be treated as recurrences of the kaon.

This view of diffractive dissociation is illustrated in figure 4.2.5; we shall refer back to it later.

So far in this chapter we have pointed out the occurence of diffractive dissociation in the two-pion-production channels. The cross-sections for the dissociations $K^- \rightarrow K\pi\pi$, $K^- \rightarrow K^*(890)\pi^-$, and $p \rightarrow \Delta^{++}(1236)\pi^-$ are collected together in the table of figure 4.2.6. We have already mentioned that there is a good deal of $\Delta^{++}(1236)$ production in reaction (i), as well as $K^{*o}(890)$. In the next section, we shall concentrate on the quasi-three-body final states involving these resonances.

FIGURE 4.2.5

A view of diffractive dissociation:

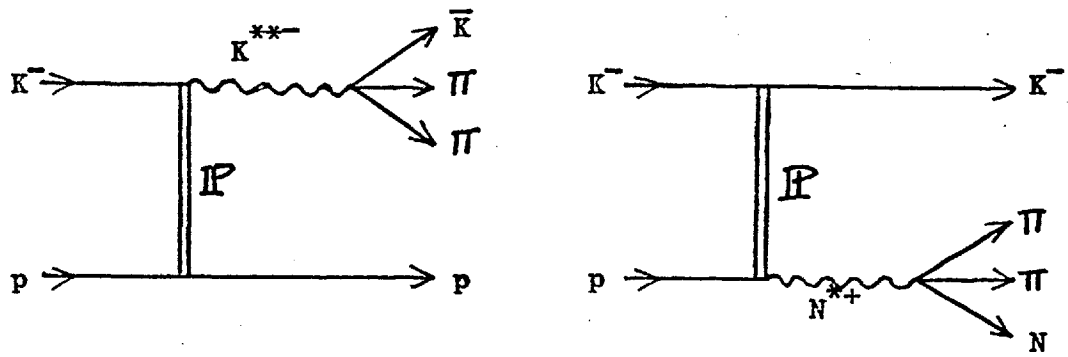

FIGURE 4.2.6

Cross-Sections for diffractive dissociation processes:

Process	Restrictions	Cross-Section
$K^- \to K^-\pi^+\pi^-$	No Δ, $m(\bar{K}\pi\pi) < 2.5$ GeV	0.59 mb. $\pm$ 3½%
$K^- \to K^-\pi^+\pi^-$	No Δ, $m(\bar{K}\pi\pi) < 1.5$ GeV	0.35 mb. $\pm$ 4%
$K^- \to K^0\pi^-\pi^0$	No Δ, $m(\bar{K}\pi\pi) < 2.5$ GeV	0.55 mb. $\pm$ 4%
$K^- \to K^0\pi^-\pi^0$	No Δ, $m(\bar{K}\pi\pi) < 1.5$ GeV	0.33 mb. $\pm$ 4½%
$K^- \to K^*(890)\pi^-$	No Δ, $m(K^*\pi) < 2.5$ GeV $K^* \to K^-\pi^+$ only.	0.29 mb. $\pm$ 4%
$p \to \Delta(1236)\pi^-$	No $K^*(890)$, $m(\Delta\pi) < 2.5$ GeV.	0.13 mb. $\pm$ 5%

N.B. (i) K^* and Δ resonances are defined by the intervals
$K^* = (0.82, 0.96)$ GeV/c^2, $\Delta = (1.12, 1.34)$ GeV/c^2

(ii) In addition to the restrictions mentioned in the table, we require /t/ to be less than 0.6 GeV^2 in every case. Here, t is t_{pp} or t_{KK} as appropriate.

(iii) Errors quoted are statistical, based on numbers of events.

4.3 THE DOUBLE-REGGE-EXCHANGE MODEL

Here, we will analyse two important quasi-three-body subreactions of reaction (i), viz.

(iv) $K^-p \to K^{*o}(890)\pi^-p$, and

(v) $K^-p \to K^-\pi^-\Delta^{++}(1236)$.

There is a great deal of $K^{*o}(890)$ in the diffractively produced $K^-\pi^+\pi^-$ systems — about 50% — and by selecting this resonance we obtain a $K^*\pi$ mass spectrum which is not very different from the full $K^-\pi^+\pi^-$ spectrum (fig.4.3.2(b) c.f. fig.4.2.3(a)). We have a relatively smaller L enhancement because the branching ratio for $L \to K^*(890)\pi$ is less than that for the Q (Ref. 1.20, for example).

The $\Delta\pi$ spectrum (fig. 4.3.3(b)) turns out to be much more sharply peaked to low values of the effective mass than the $p\pi^+\pi^-$ spectrum (fig. 4.2.4). It seems that the selection of the Δ leaves a much "cleaner" set of events.

We will discuss these reactions in the light of the multi-peripheral picture (fig. 4.3.1), using the Double-Regge-exchange model with Pomeron exchange in order to make predictions. This well-known model has been tested by many authors in the past (Refs. 4.1, 4.2 and 4.3). If reaction (iv) above is assumed to proceed according to fig. 4.3.1(a), the squared matrix element is of the form

$$|A|^2 = N \cdot Q_{\pi p}^{\ 2} \cdot \exp(7t_{pp}) \cdot (Q_{\pi K^*})^{2\alpha} \cdot \frac{1}{1 - \cos(\pi\alpha)} \qquad (4.1)$$

where

$$Q_{\pi p} = s_{\pi p} - t_{KK^*} - m_p^{\ 2} + \tfrac{1}{2}(t_{pp} + t_{KK^*} - m_\pi^{\ 2})$$

$$Q_{\pi K^*} = s_{\pi K^*} - t_{pp} - m_K^{\ 2} + \tfrac{1}{2}(t_{pp} + t_{KK^*} - m_\pi^{\ 2}) \cdot \frac{t_{KK^*} + m_K^{\ 2} - m_{K^*}^{\ 2}}{t_{KK^*}}$$

$$\alpha = \alpha'(t_{KK^*} - m_\pi)$$

N = Normalisation constant.

In fact we will ignore the first factor of (4.1), i.e. treat the overall normalisation as a free parameter. In the third factor, the coefficient of t_{pp} is taken to be 7.0 GeV^{-2}, a typical "slope" for πp elastic scattering. We use a linear pion trajectory α, and will take its slope α' to be 1.0 GeV^{-2}.

Similarly, assuming reaction (v) to be described by the exchanges in fig. 4.3.1 (b), we use for our squared matrix element the expression

$$|A|^2 = N \cdot Q_{K\pi}^{\ 2} \cdot \exp(3t_{KK}) \cdot (Q_{\pi\Delta})^{2\alpha} \cdot \frac{1}{1 - \cos(\pi\alpha)} \qquad (4.2)$$

where

$$Q_{K\pi} = s_{K\pi} - t_{p\Delta} - m_K^{\ 2} + \tfrac{1}{2}(t_{KK} + t_{p\Delta} - m_\pi^{\ 2})$$

$$Q_{\pi\Delta} = s_{\pi\Delta} - t_{KK} - m_p^{\ 2} + \tfrac{1}{2}(t_{KK} + t_{p\Delta} - m_\pi^{\ 2}) \cdot \frac{t_{p\Delta} + m_p^{\ 2} - m_\Delta^{\ 2}}{t_{p\Delta}}$$

α = pion trajectory, same as used above.

Again we shall not fix the overall normalisation factor N. Note that in the third factor of (4.2) t_{KK} is given a coefficient of only 3.0 GeV^{-2}. This is, in effect, the $K\pi$ elastic scattering slope; as such, it is not directly measurable experimentally, but can be estimated by comparing πp, Kp and pp elastic scattering slopes at high energies. This procedure assumes that the elastic scattering differential cross-sections can be factorised into Pomeron "form factors", of exponential form, for each particle. Our value of 3.0 GeV^{-2} for the $K\pi$ elastic scattering slope was found in this way, and checked by comparing fig. 4.3.3 (c) with the predictions given by eqn. (4.2) using this and neighbouring slopes.

In figures 4.3.2 and 4.3.3, the data has superimposed on it the predictions of the Double-Regge-exchange model (dashed lines). These curves are normalised to the total number of events in each case (except for fig. 4.3.3(a)), and were obtained by use of the Monte-Carlo phase space integration program FOWL, which is described in Chapter 5. Note that both the data and the predicted curves given here have t_{pp} (or t_{KK}) restricted to being less than 0.6 GeV^2 in absolute value.

FIGURE 4.3.1

Multiperipheral Diagrams for the reactions

(a) $K^- p \rightarrow K^{*o}(890)\pi^- p$, and

(b) $K^- p \rightarrow K^- \pi^- \Delta^{++}(1236)$

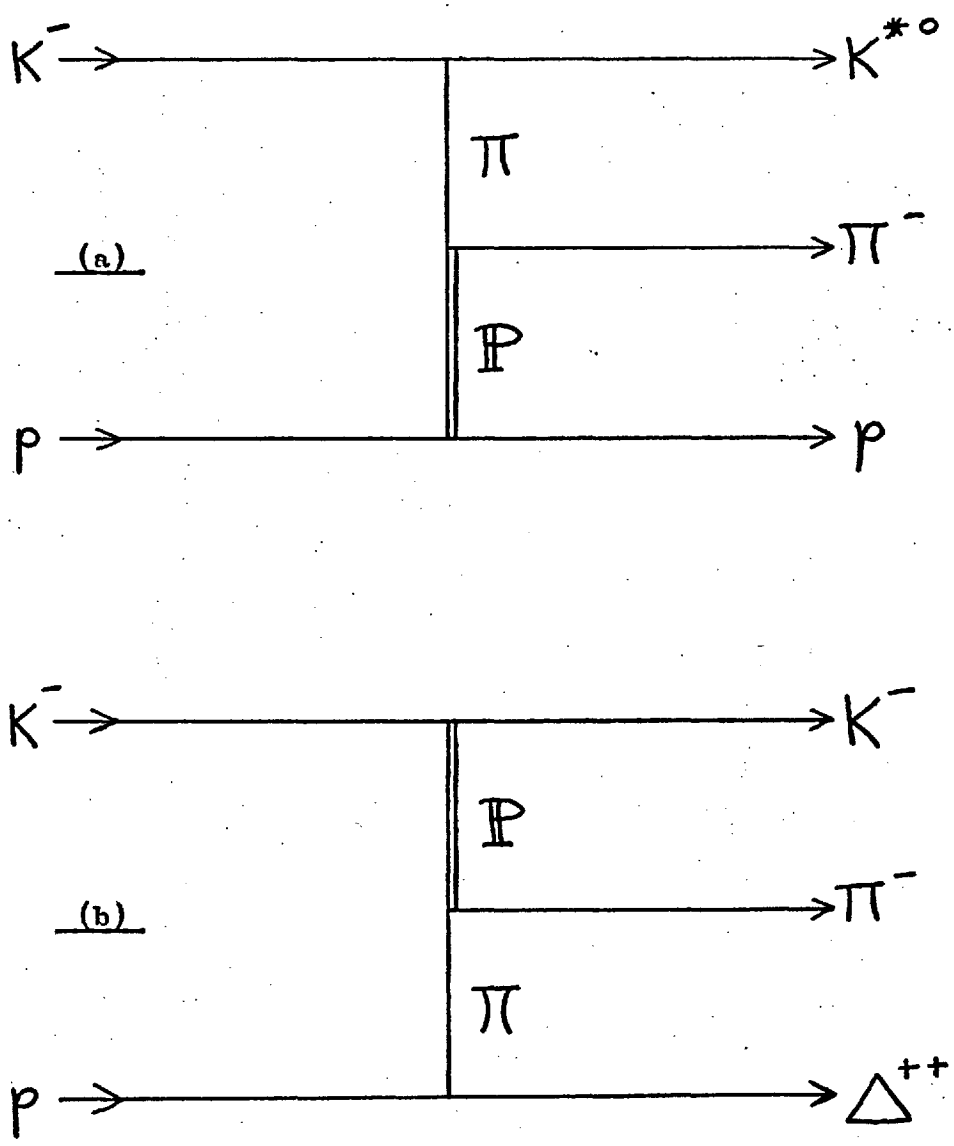

FIGURE 4.3.2 $K^- p \rightarrow K^{*o} \pi^- p$

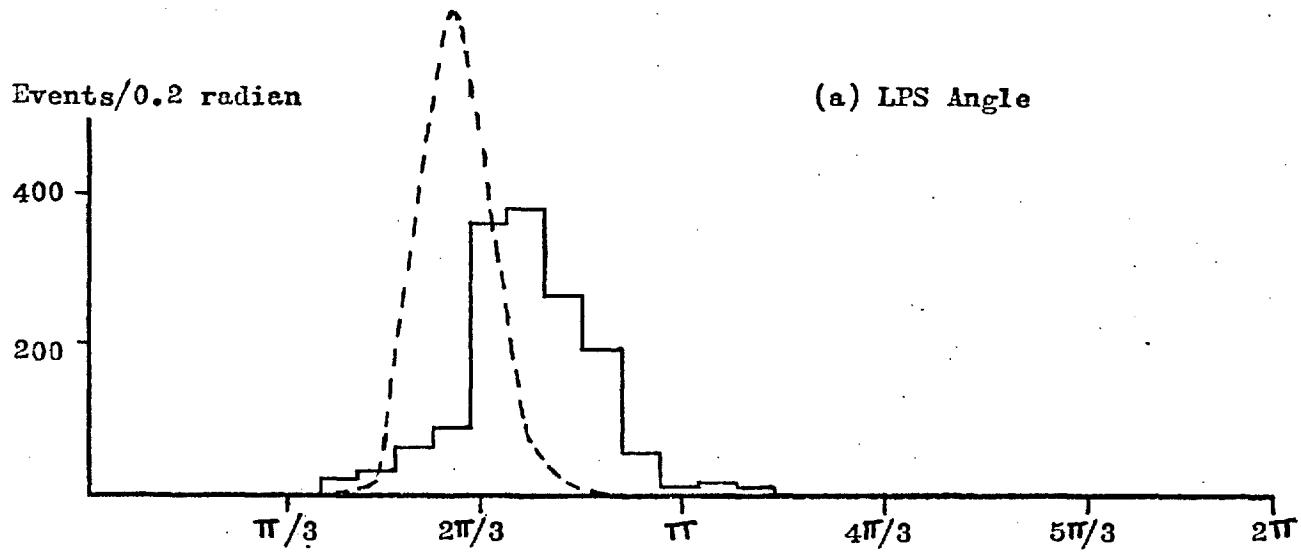

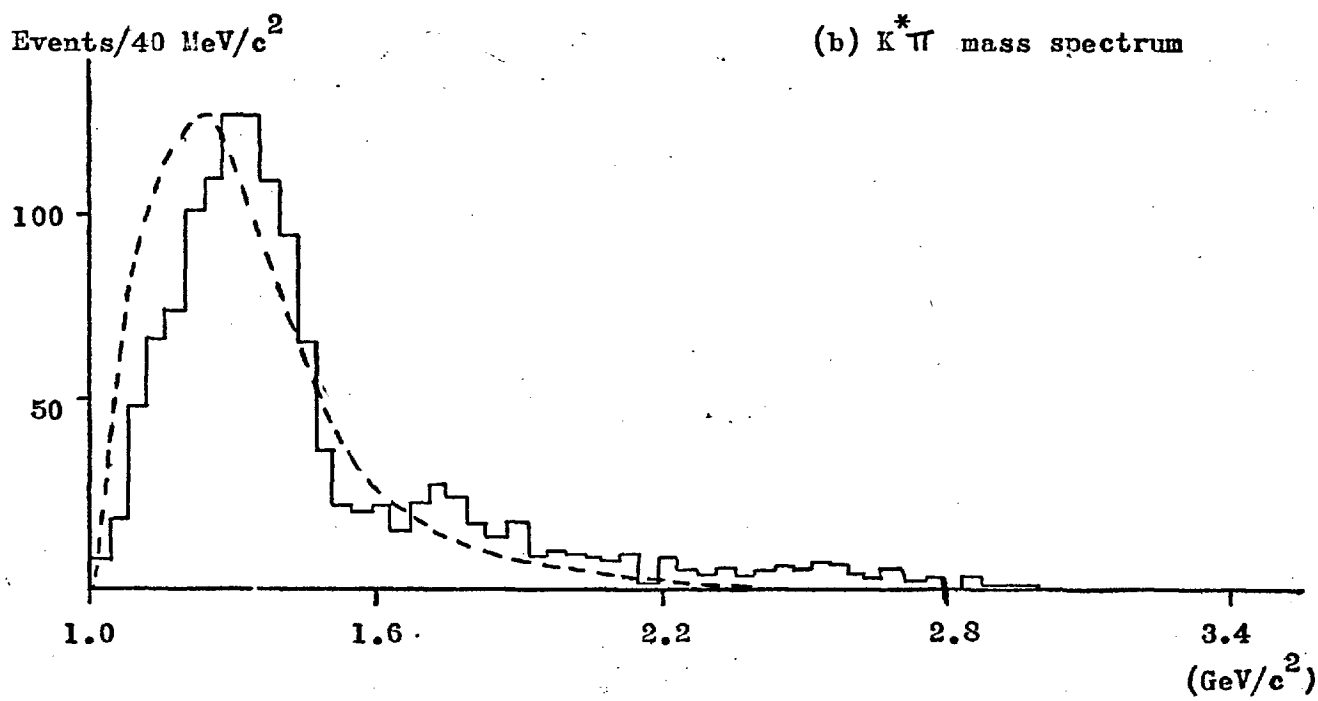

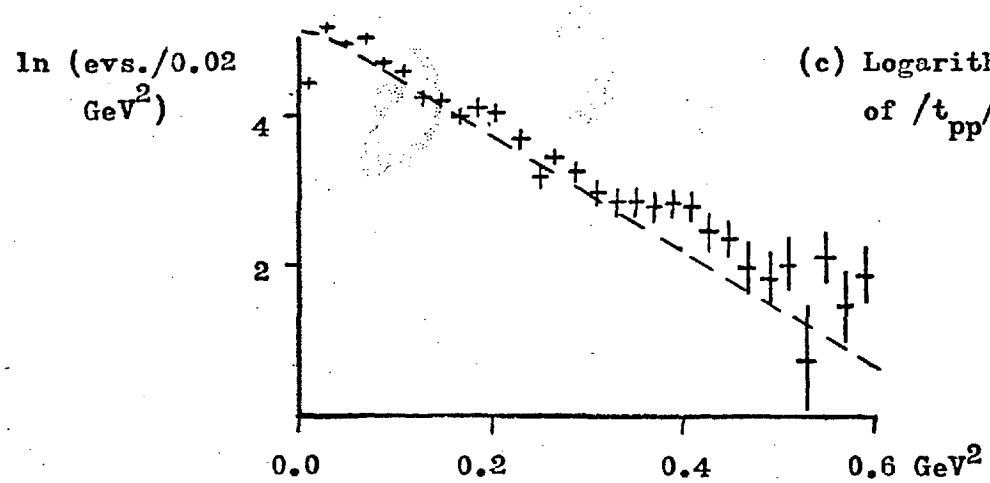

FIGURE 4.3.3 $K^- p \rightarrow K^- \pi^- \Delta^{++}$

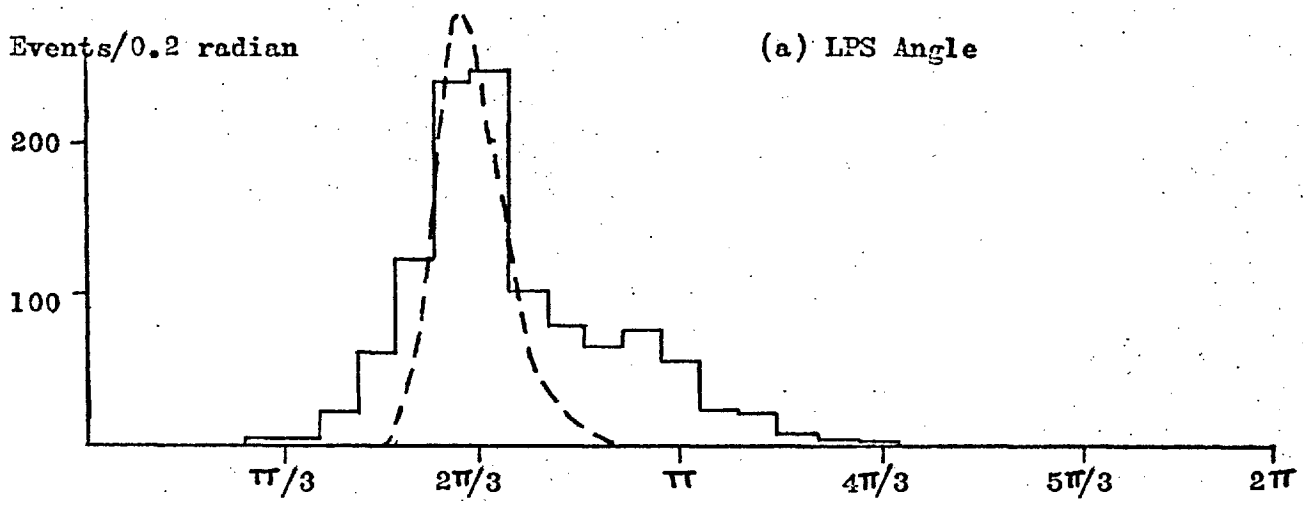

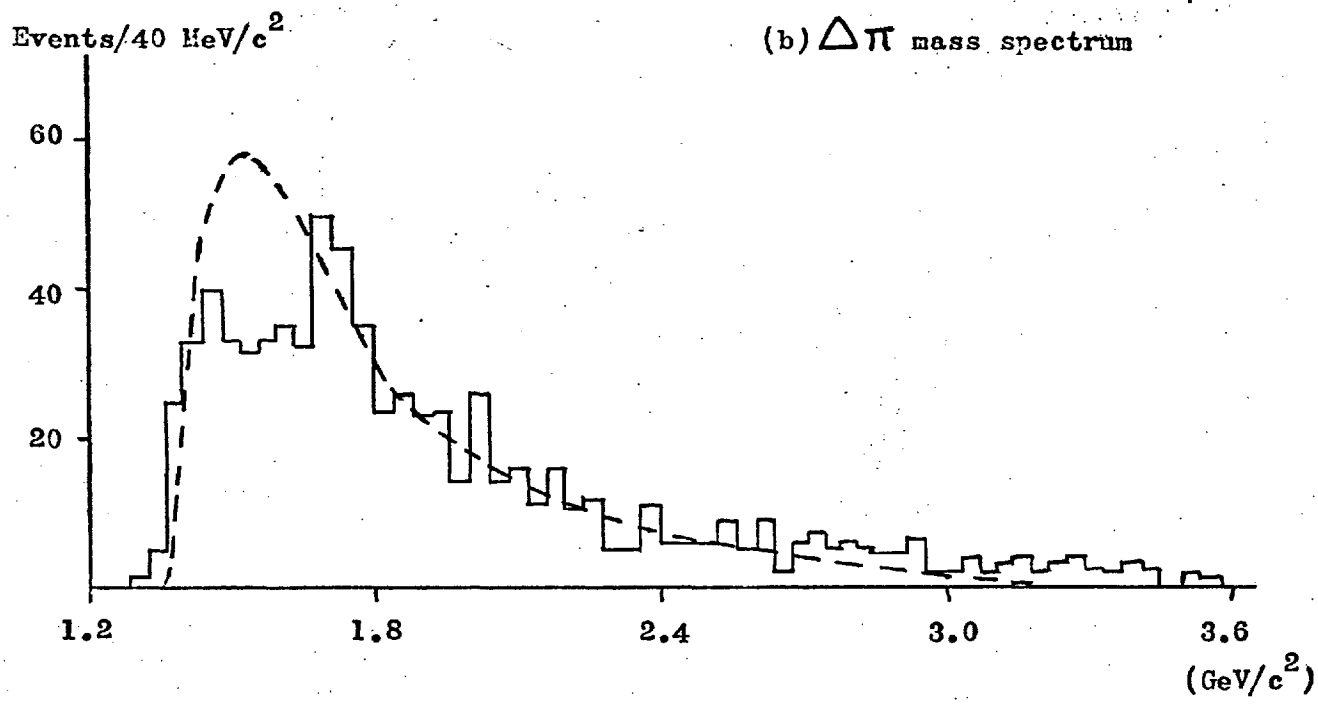

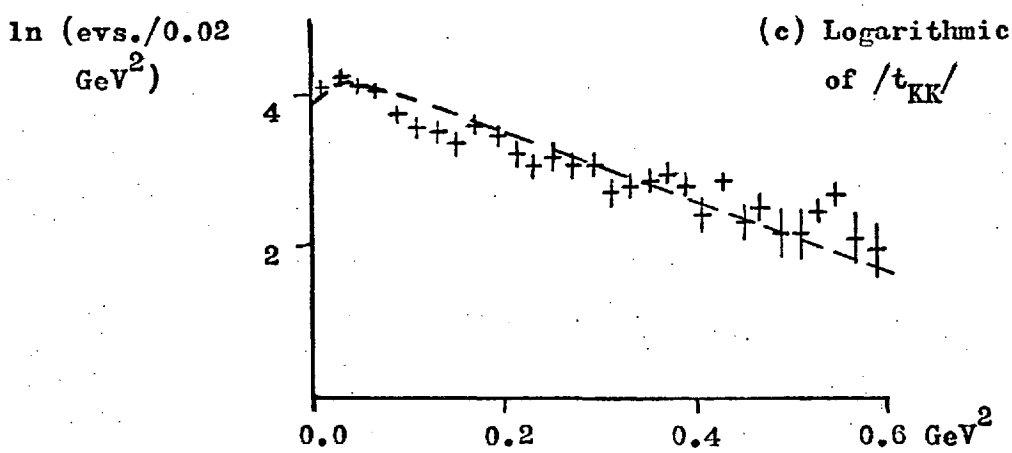

The distributions which we have chosen to show in figs. 4.3.2 and 4.3.3 are of particular interest for comparing the predictions of the model with the experimental data. Let us look first at the t-distributions. These are very well fitted by the model, and are approximately exponential with slopes of 7.7 and 4.6 GeV^{-2} for t_{pp} and t_{KK} respectively.

Only the gross features of the $K^*\pi$ and $\Delta\pi$ effective mass spectra are predicted by the model; there is in each case a low-mass threshold enhancement, but this cannot explain the structure which is apparent in the data, particularly the $\Delta\pi$ mass spectrum. On the other hand, the suppression of high effective masses in both spectra is described well by the Double-Regge model.

Figures 4.3.2 (a) and 4.3.3 (a) are the distributions of the longitudinal momentum phase space angle ("LPS" angle) which is explained in Appendix E. (N.B. With reference to fig. E1, we adhere to the convention that particle 1 is the "leading", or "beam-like" particle, and particle 3 the "target-like" particle.)

There is an immediately obvious discrepancy shown up between theory and experiment in the first of these figures. The predicted curve peaks close to an angle of $2\pi/3$ radians, i.e. the pions are predicted to be slow-moving in the C.M. frame. The data, on the other hand, indicate that the pions tend to be moving forward, i.e. in the direction of the K^*. This is because the $K^*\pi$ systems are largely resonant; in particular the Q bump takes up a large proportion of the cross-section in this case, and can be regarded as a 1^+ resonance with an s-wave (i.e. isotropic) decay into $K^*\pi$. The failure of this model to take this into account is the reason for the disagreement in fig. 4.3.2 (a).

For a different reason, there is also a disagreement between the data and our predictions in figure 4.3.3 (a). The main peak at an LPS angle of $2\pi/3$ radians is satisfactorily explained, but there is an additional surplus of events in the third sextant which is absent on the theoretical curve. Events in this region

involve a negative pion travelling forward (in the C.M.) along with the K^-.

We interpret these events as arising from nondiffractive $K^-\pi^-$ scattering, perhaps (in the multiperipheral picture) involving K^* exchange. In other words, the discrepancy in figure 4.3.3 (a) arises because the cuts we have applied to the data do not exclude all nondiffractive events.

In conclusion: Diagrams 4.3.1 (a) and (b), quantified by eqns. (4.1) and (4.2), are found to be a fair description of our data on the reactions $K^-p \rightarrow K^{*o}(890)\pi^-p$ and $K^-p \rightarrow K^-\pi^-\Delta^{++}(1236)$. The discrepancies found between our data and our predictions can be understood without compromising the conclusion that these reactions are dominated by diffractive dissociation.

4.4 UNDERSTANDING DIFFRACTIVE DISSOCIATION

We have just seen that the Double-Regge-exchange model gives predictions for the $K \rightarrow K^{*}\pi$ and $p \rightarrow \Delta\pi$ dissociation processes which are in reasonable agreement with the experimental data. The distributions show that the main source of disagreement is the failure of this model to allow for resonant beheviour in the $K^{*}\pi$ and $\Delta\pi$ systems.

The Double-Regge-exchange model with Pomeron exchange is the modern refinement of the idea of Deck (Ref. 4.4) which pictures diffractive dissociation as the elastic scattering of an initially virtual particle. See figure 4.4.1(a). Given that hadrons in general can always be regarded as bound states of other hadrons, we can see that such scattering must surely occur, and we are provided with a way of visualising diffractive dissociation which is simple and for many purposes very useful.

On the other hand, we need to be able to understand the diffractive production of resonances — or, at any rate, of resonance-like enhancements. Figure 4.4.1 (b) can give us an insight into this. Here we have drawn a "triangle graph" which, if regarded as a Feynman graph, can for our purposes be contracted to the form of figure 4.4.1 (c). This latter diagram will have singularities where the internal lines are on the mass shell and have four-momenta which are proportional to one another (the Landau-Bjorken conditions). That is to say, we expect the $K^{*}\pi$ mass spectrum to peak at the value $m(K)+m(\rho) = 1260$ MeV/c^2, and the $\Delta\pi$ spectrum similarly at 1700 MeV/c^2. (N.B. We take the rescattering vertices to be $K\rho \rightarrow K^{*}\pi$ and $N\rho \rightarrow \Delta\pi$ because they are the simplest exothermic transitions we could have here.)

The bumps predicted by the above argument may be identified with the Q enhancement and the $N^{*}(1690)$. If we replace the ρ by the f(1260), the masses predicted are close to those of the L and the $N^{*}(2190)$. Thus, much of the structure seen in the mass spectra of the diffractively-produced systems can be explained by a remarkably simple model which does not invoke the existence of resonances in these systems.

FIGURE 4.4.1 Mechanisms for Diffractive Dissociation:

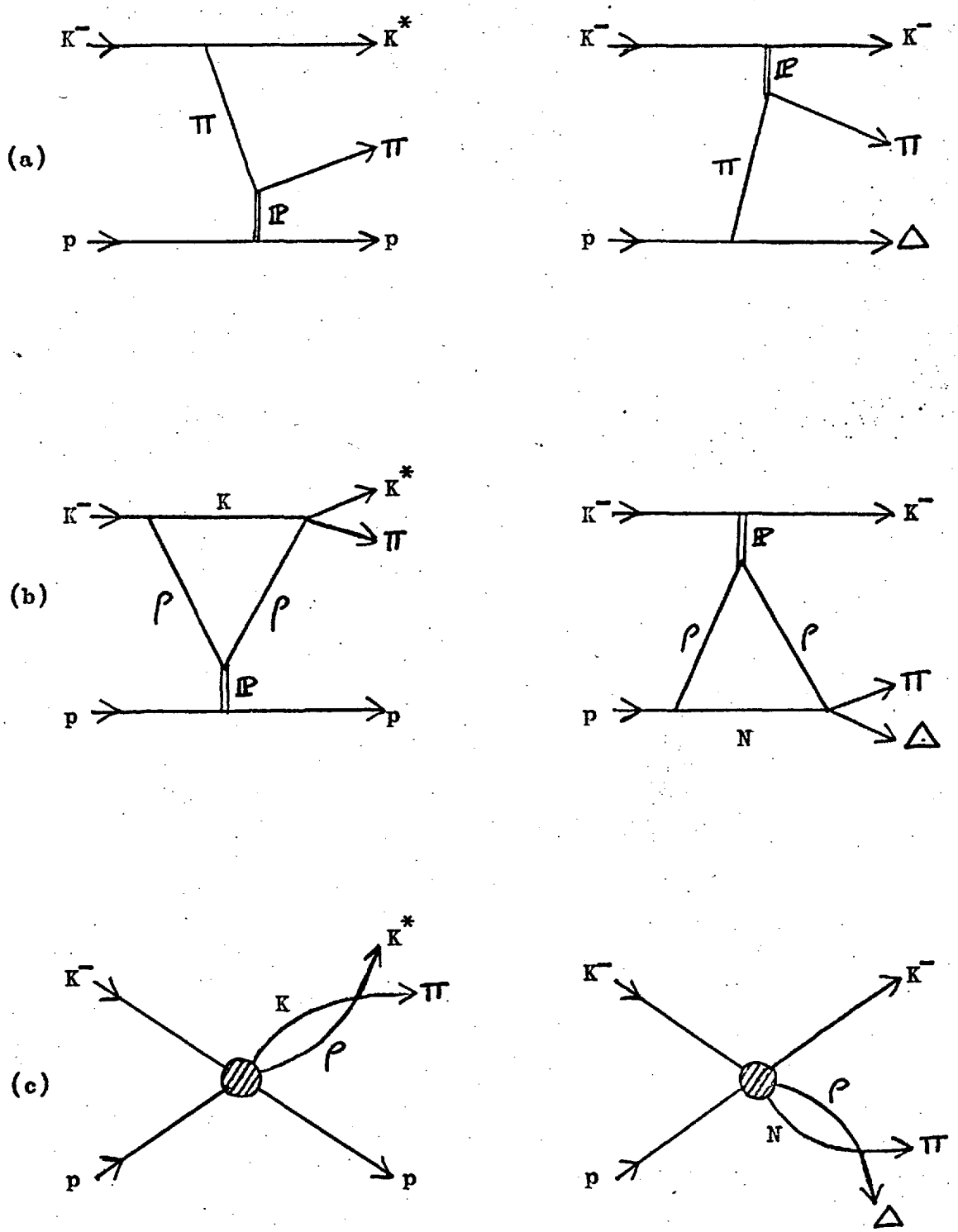

We have now introduced three distinct explanations for the diffractive dissociation phenomena that we have observed, shown diagrammatically in figures 4.2.5 and 4.4.1. We cannot point to any one of them as being the "correct" description; each of them contains some truth, and yet none of them in itself can give us a complete explanation.

In fact, we are faced with an excellent example of the concept of Duality (See Refs. 4.5 and 4.6, for example) . This is one of the most important recent developments in the field of hadron physics, and has great unifying strength in enabling us to understand apparently distinct explanations for certain hadronic reactions as being no more than alternative representations of essentially the same physical processes.

In the present examples, the idea of Duality leads us to hope that a "good" description of the $K^- P K^{*} \pi$ and $pP\Delta\pi$ vertices would contain, as special cases, the aspects which we have discussed in this Chapter.

In the next Chapter we will in fact develop a dual model for the $K^- \rightarrow K\pi\pi\pi$ diffractive dissociation vertex, which unifies (inter alia) the "s-channel" and "t-channel" descriptions which are shown by figs. 4.2.5 and 4.3.1(a). To understand our "triangle graph" explanation in the same context is a rather more subtle problem, to which we will return in Chapter 7 when we discuss the Pomeron in terms of dual loop graphs.

References (4)

4.1 E. Berger, Physical Review, 166 (1968), 1525

4.2 D. Grether and R. Sard, Nuclear Physics B14, 381 (1969)

4.3 M. J. Losty, Ph.D. Thesis (imperial College) 1971

4.4 R. T. Deck, Physical Review Letters 13, 169 (1964)

4.5 H. Satz, CERN Preprint TH.1214 (1970)

4.6 C. Schmidt, CERN Preprint TH.1128 (1970)

CHAPTER 5

A DUAL DIFFRACTIVE MODEL FOR THE Q AND L MESONS

We present here a study of the reaction

$$K^-p \rightarrow (K^-\pi^+\pi^-)p \qquad (5.1)$$

where the assumption is made that it proceeds by Pomeron exchange as illustrated in figure 5.0.1, i.e. that the production of the $K^-\pi^+\pi^-$ system is a diffractive process. This process is characterised by predominantly low $K^-\pi^+\pi^-$ effective masses, and by small four-momentum transfers t_{pp} from the proton.

As was mentioned in the previous Chapter, the $K^-\pi^+\pi^-$ mass spectrum contains the Q and L enhancements, which have been the subject of some controversy among different authors. They have been explained by some as resonances with unnatural spin-parity which is usually accepted as being 1^+ for the Q and 2^- for the L meson. Other authors have argued instead that these peaks result from a kinematic mechanism similar to that proposed by Deck (Ref. 4.4).

We have developed a model which combines these interpretations by being explicitly dual with respect to the top vertex of figure 5.0.1. It is similar in essence to that used by Pokorski and Satz (Ref.5.1) to describe diffractive dissociation of the nucleon in the reaction $pp \rightarrow pn\pi^+$.

5.1 DESCRIPTION OF THE MODEL

The amplitude for the diffractive process (5.1) is factorised in the form

$$A = F(p,p') \cdot S(p',K^-,\pi^+,\pi^-) \cdot V(K^-_{(in)},P,K^-,\pi^+,\pi^-) \qquad (5.2)$$

where the bracketed parameters indicate the four-momenta on which

FIGURE 5.0.1

Schematic graph for the diffractive reaction $K^-p \to (K^-\pi^+\pi^-)p$

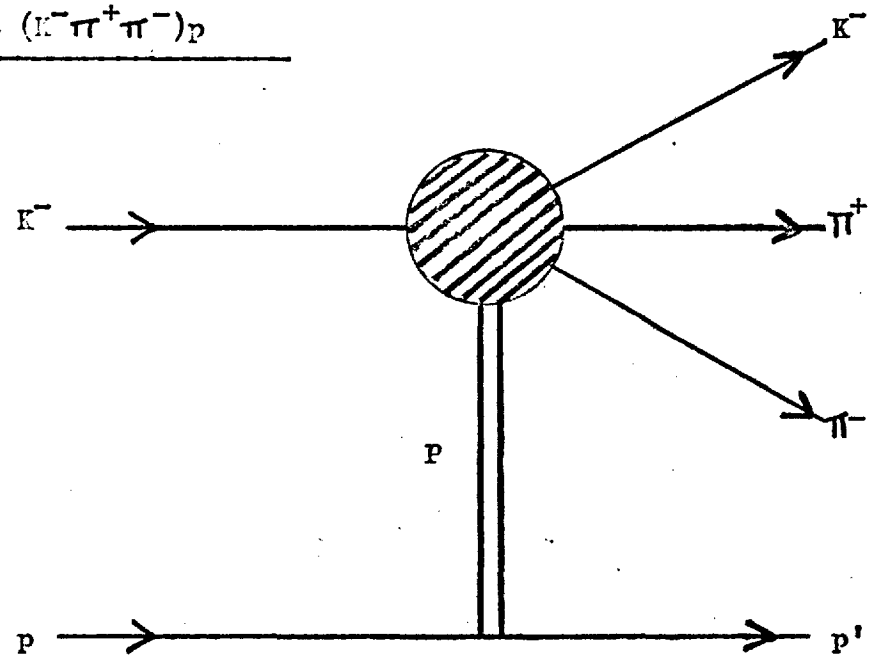

FIGURE 5.1.1

Labelling for the B_5 function

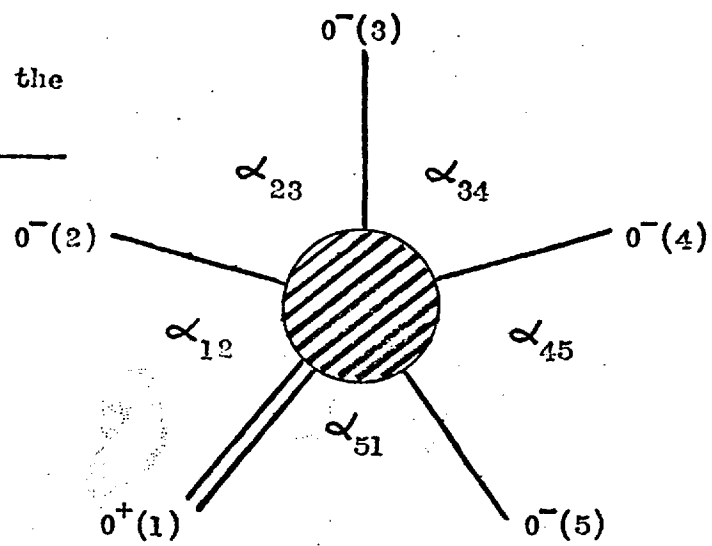

each of the three factors can depend. (The P represents the Pomeron). Although our model can be applied equally well to any of the charge configurations for the $K^-p \rightarrow (\overline{K}\pi\pi)p$ reaction, we will concentrate on reaction 5.1, for which we have a large data sample consisting of four-constraint fits.

The factor F

The first factor of eqn. 5.2, $F(p,p')$, describes the lower vertex, and we expect it to be a function of the four-momentum transfer from the target to the final proton. We use the usual expression for Pomeron exchange, viz.

$$F = \exp(\tfrac{1}{2}A.t_{pp}) \quad . \tag{5.3}$$

Now, at the point where $m(K^-\pi^+\pi^-) = m_K$, the factor V has a pole with constant residue and the factor S reduces to a constant. At this (unphysical) pole, we would expect the residue of eqn. 5.2 to describe elastic K^-p scattering, and so the slope A in eqn. 5.3 is taken to be that found experimentally (Ref. 5.2) for elastic K^-p scattering at 10 GeV/c.

The factor V

This factor is a dual Veneziano-type amplitude which describes the upper vertex of fig. 5.0.1. The Pomeron is here treated as a scalar particle with the quantum numbers of the vacuum. The coupling of four pseudo-scalar and one scalar particle has been investigated within the Veneziano model by Savoy (ref. 5.3) in connection with the interaction of the σ meson with four pions. The exchanged trajectories start with P-wave resonances between two pseudoscalar particles, and with S-wave resonances between a pseudoscalar and the scalar particle. Explicitly, with labelling indicated in fig. 5.1.1, the Veneziano amplitudes are of the form

$$V = -\alpha_{34}.B_5(-\alpha_{12},1-\alpha_{23},-\alpha_{34},1-\alpha_{45},-\alpha_{51}) \tag{5.4}$$

where α_{ij} is the trajectory funtion for the pair of particles i and j.

It was shown by Savoy that this amplitude has the correct properties in all its Regge limits. The B_5 function is the five-point generalisation of the Beta-function which was introduced by Bardakci and Ruegg.

In our case, where the particles are $K^-_{(in)}$, P, K^-, π^+ and π^-, we can form four cyclic permutations of them which are non-equivalent and which do not contain exotic channels. These give rise to four terms, each of the form of eqn. 5.4. These permutations are illustrated in figure 5.1.2. In forming the complete Veneziano amplitude V in eqn. 5.2, we add these four terms to obtain a fully crossing-symmetric expression. Their weights are taken to be equal for the following reasons:

(a) Close to the second pole in the K-trajectory (i.e. the Q meson) terms I and II of fig. 5.1.2 will dominate the amplitude. If they are added with equal weight, it can be shown that the decays $Q \rightarrow K^*\pi$ and $Q \rightarrow K\rho$ are predicted to be S-wave, as required by experiment. This is verified by the results we will show later.

(b) Terms I and III must contribute equally if the sum V is to be C-invariant.

(c) For reasons of symmetry, term IV must have the same weight as the other three terms.

In evaluating the B_5 functions, we have used complex trajectory fuctions with linear real parts; the trajectory parameters are calculated and listed in Appendix C. The imaginary parts of the trajectory functions are chosen to give non-zero widths to the produced resonances. In the case of the kaon trajectory, we have chosen an imaginary part which gives a Q-meson width which is rather narrower than the observed peak at 10 GeV/c. The peak has become narrower with increasing energy, and we expect that it will continue to do so when very high-energy experiments can be performed; it is by no means clear that the observed peak is due to a single resonance, and it has been suggested (Ref. 5.4) that there are two 1^+ resonances present, with opposite C-parities. Only one of these resonances can be produced by Pomeron exchange, and

FIGURE 5.1.2

The four non-exotic graphs contributing to the Veneziano amplitude.

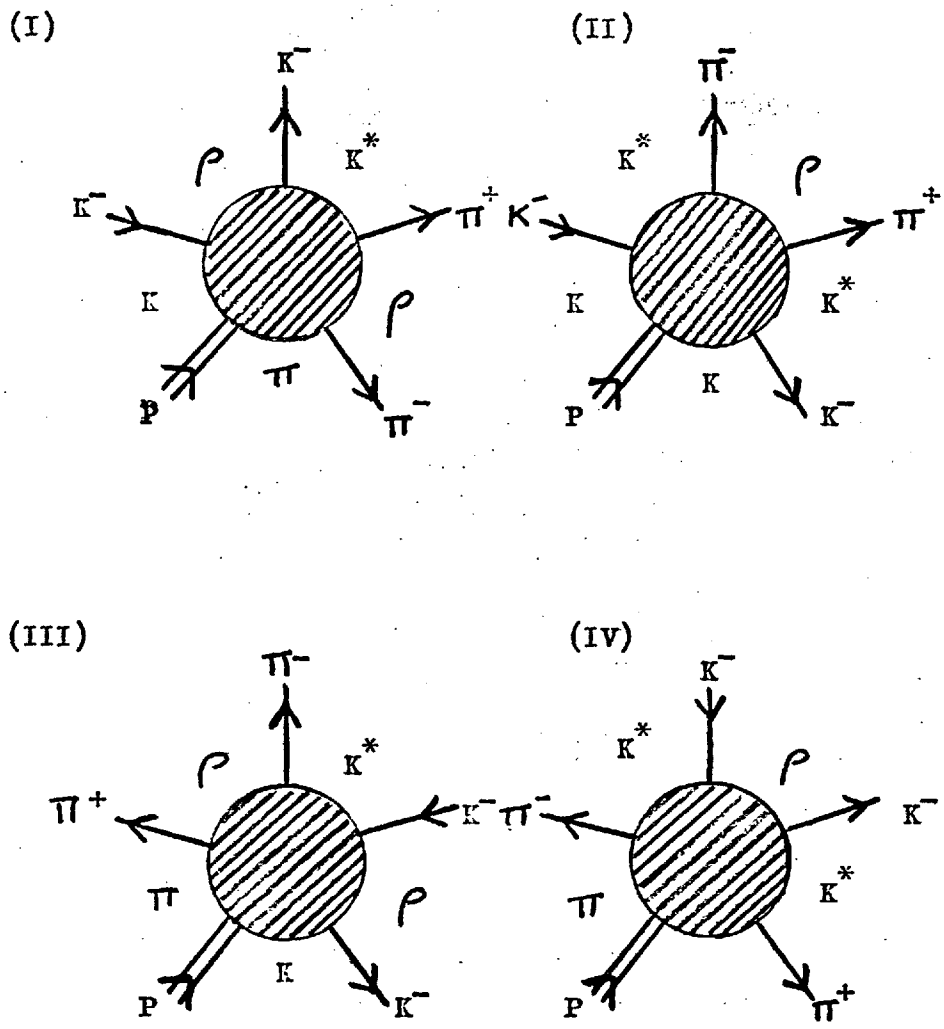

should survive at high energies.

In this connection, we should point out that our model should describe $K^+p \to K^+\pi^-\pi^+$ as well as reaction 5.1. However, there are significant differences between the Q mesons observed experimentally in K^- and K^+ experiments — in the latter, the peak is usually observed to be split. We cannot, then, expect our model to describe in detail the structure of the Q enhancement, and we feel justified in using a kaon trajectory function which implies a more realistic width than that which is observed.

An important assumption which is made in our choice of trajectory functions is that the combination of the Pomeron with a meson leads to a state lying on the same Regge trajectory as that meson.

The factor S

The reaction of figure 5.0.1 has the Regge limits shown explicitly in figure 5.1.3, and all these different graphs are taken into account by the dual nature of the Veneziano amplitude. An intrinsic difficulty in treating the diffraction process in our model arises from the fact that the Pomeron couples to the top vertex as a 0^+ particle (the Gribov-Morrison rule, Ref.5.5) yet behaves like a spin 1 particle for the Regge limits. In fact, the Pomeron can be described by a trajectory with intercept $\alpha(0) = 1$ and very small slope.

The 0^+ coupling has been taken into account in constructing the Veneziano amplitude; we now need a factor S which becomes $S_{p'\pi^-}$ when the Pomeron couples to the π^- as in fig. 5.1.3 (b), but $S_{p'K^-}$ in the limit of fig. 5.1.3 (d) and so on for the other graphs. We consider that the most realistic prescription for S is to use $S_{p'M}$, where M is the "trailing" meson of the outgoing $K^-\pi^+\pi^-$ system. In other words, we take S to be the squared

FIGURE 5.1.3

Regge Limits of the Amplitude for $K^- p \to (\bar{K}\pi\pi)p$

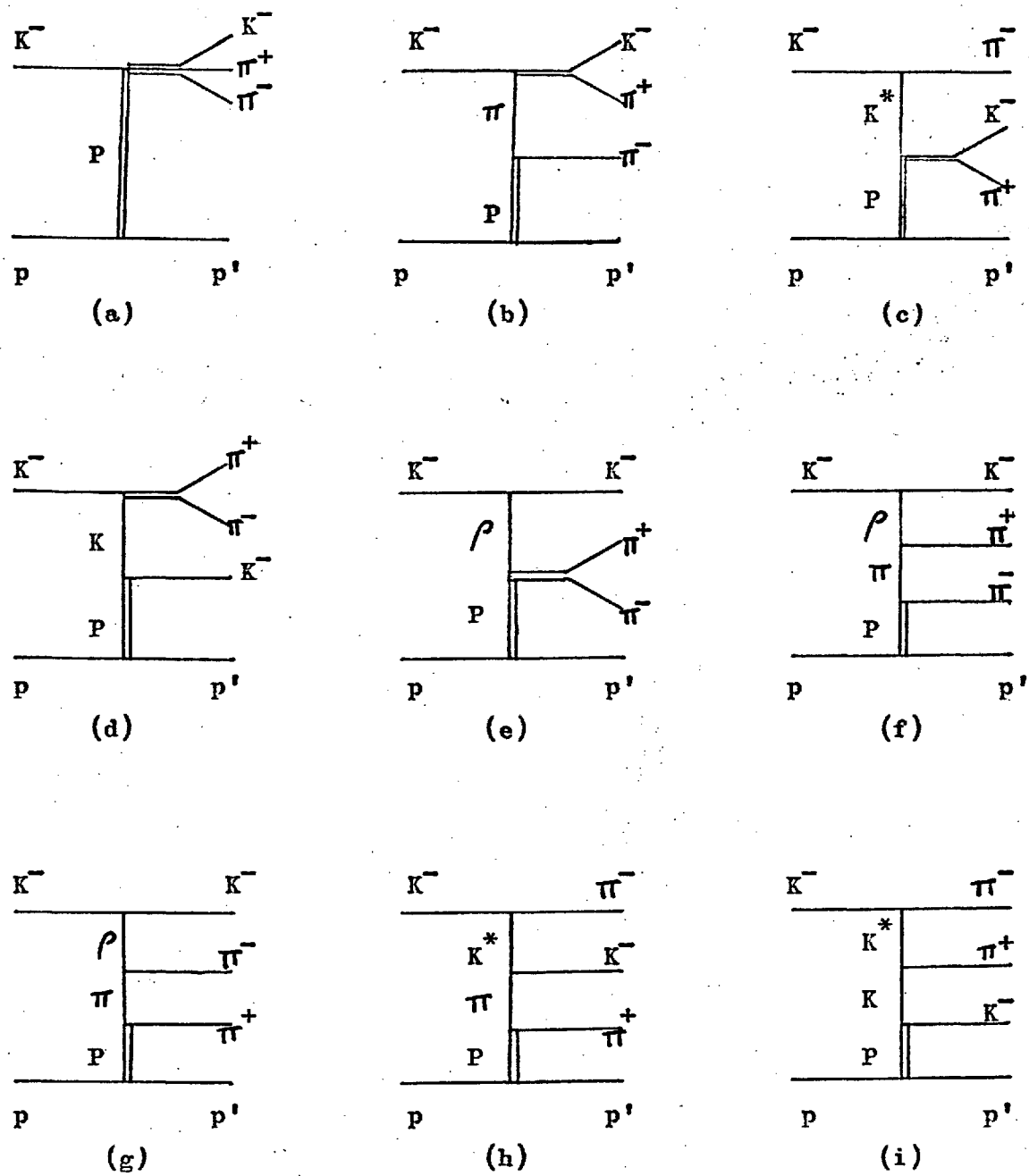

effectve mass between the outgoing proton and the outgoing meson with the lowest longitudinal C.M. momentum; in this way we ensure the correct Regge behaviour for our amplitude in a simple and transparent way.

Alternatively, we can devise a C-symmetric analytic function for S which has similar properties, viz.

$$S = S(pK^-_{in}) + S(p'K^-) + S(p\pi^+) + S(p'\pi^-)$$
$$+ t_{pp'} - 4m_p^2 - 2m_K^2 - 2m_\pi^2$$

and we have verified that this leads to the same results as the prescription described above.

The choice of the factor S is crucial to the model; if we use a constant (as is done in Ref. 5.1) then our $\bar{K}\pi\pi$ mass spectrum would be grossly distorted towards high masses. With the presciption proposed here the amplitudes at the Regge limits are essentially equivalent to those used in multi-Regge model calculations.

Overall Normalisation

The amplitude of eqn. 5.2 is not, as it stands, correctly normalised, and the Veneziano model by itself does not provide the normalisation for our B5 functions in the factor V. There are possible justifications for using Sakurai's universal ρ coupling constant f^2 for this purpose (Ref. 5.6) , but we have not made use of this and we treat the absolute normalisation as a free parameter in our model.

It should be pointed out that even if eqn. 5.2 were normalised, the cross-section that would follow for reaction 5.1 would still be very sensitive to the widths that we take for the resonances produced in the $\bar{K}\pi\pi$ system. (To understand why, consider the expansion of the B5 function close to one of its poles in the physical region. An example of such an expansion is eqn. B15 of Appendix B, and it is clear from this that the cross-section for $Q \rightarrow K^*(890)\pi$ is proportional to $1/(\Gamma_{K^*}^2)$.)

5.2 PREDICTIONS OF THE MODEL

The Program FOWL

The complete amplitude 5.2 has been calculated in the Monte-Carlo program FOWL in order to make comparisons with our experimental data. This program works by performing a Monte-Carlo integration of the squared amplitude over phase space, and this involves the sequence of events illustrated by figure 5.2.1.

To use the program efficiently, it is necessary to use "importance sampling" of events in phase space; that is to say, we generate events which, though random, tend to be in that region of phase space which is physically of importance. In practice, this is done according to the squared four-momentum transfers between the rungs of a "ladder graph" which is taken to represent the event (In our case, the graph of fig.5.1.3(g)). This means that each event generated must be given a "phase space weight" which is large in the weakly-populated regions of phase space, but small in the well-populated regions.

We have generated events according to the distribution $\exp(10t_p + 4t_\rho + 4t_\pi)$ (see fig. 5.1.3(g)). This is because the transverse momenta of the secondary particles must tend to be small (this is true in general) and so the t's will be predominantly small. In particular, we expect t_p to be very sharply peaked at low values. Anticipating that our model will predict this sort of behaviour, we must use this sort of importance sampling if the predictions resulting from the Monte-Carlo integration are to have an acceptable degree of statistical significance over the physically important regions of phase space.

Also, to improve the efficiency of computation, we only take events generated with $-t_p < 0.6$ and with $m(\bar{K}\pi\pi) < 2.5$ GeV. These limits correspond to selections made on our data in order to isolate events of type $K^- p \rightarrow (\bar{K}\pi\pi)p$ proceeding by Pomeron exchange, i.e. those which should be described by our model.

FIGURE 5.2.1 Operation of the Program FOWL

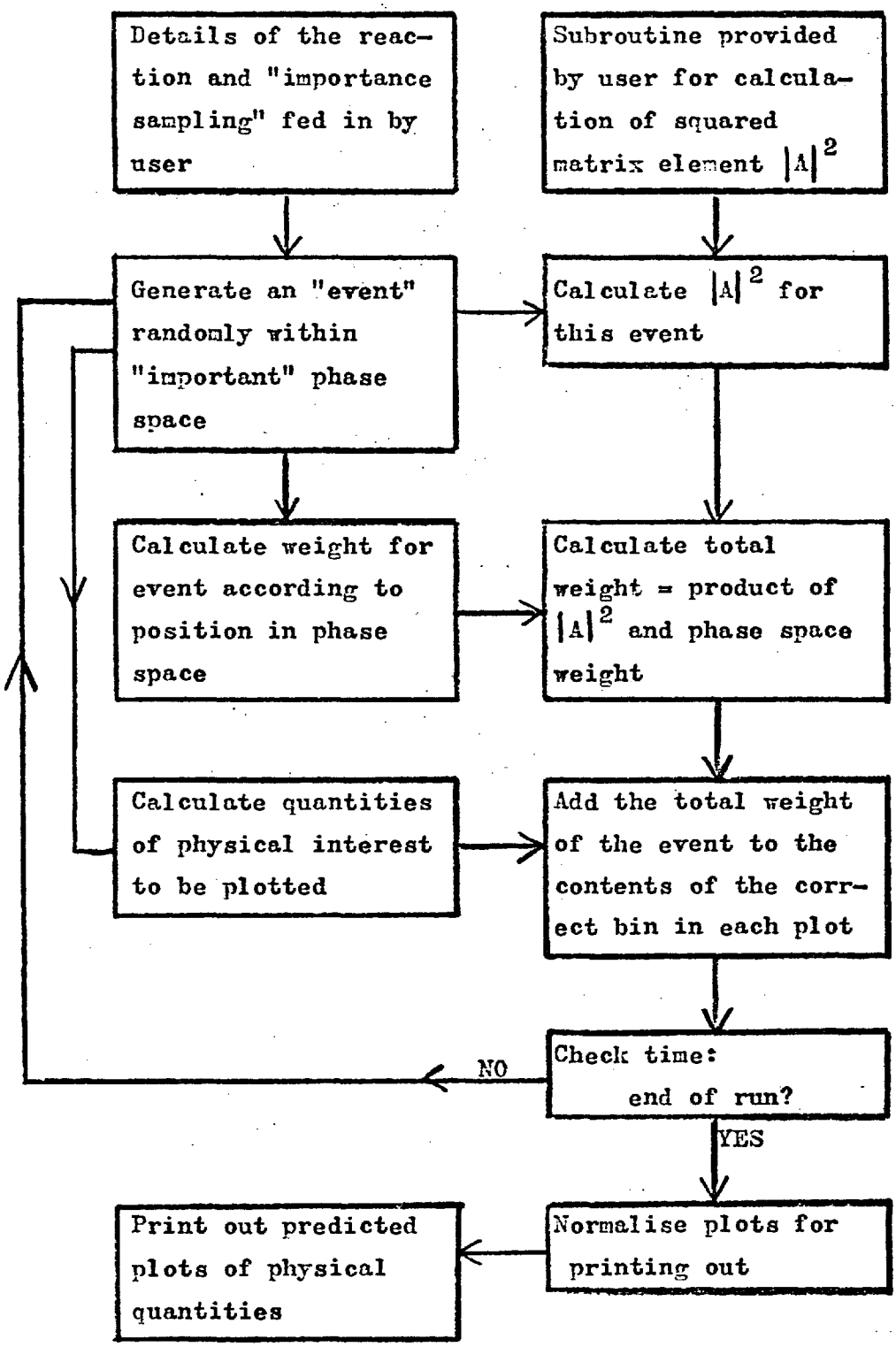

Results and Comparison with Experiment

Figures 5.2.2 and 5.2.3 show the predictions of the model model for the $\bar{K}\pi\pi$ mass spectrum and for the $t_{pp'}$ distribution, superimposed on the data. In the former, the shaded area represents the amount of $K^*(1420)$ (which cannot be produced diffractively) contaminating the data; this is estimated from the $K^*(1420)$ peaks in the $\bar{K}\pi\pi$ spectra for the reactions $K^-p \rightarrow \bar{K}\pi p$ in our experiment, using the tabulated branching ratios of the $K^*(1420)$.

The agreement of our predictions with the data is quite satisfactory. It should be borne in mind that the only free parameters in our model (besides the overall normalisation) are the trajectory parameters, and these were not adjusted a posteriori. Our predicted Q-meson is slightly narrower than the enhancement in the data — see the comments made earlier in connection with the K trajectory parameters.

Clearly, it would be possible by adjusting our trajectory parameters to fit the data very well. However, there would be no great benefit in doing this and it would require an extravagant amount of computer time.

Perhaps the most significant outcome of our work concerns the decay modes of the Q- and L-enhancements, shown by the Dalitz plots in figures 5.2.4 and 5.2.5. By the crossing symmetry inherent in our model, the predicted Dalitz plot distributions (figures 5.2.6 and 5.2.7) include not only the Q- and L-meson production from the diagrams 5.1.2 (I) and (II), but also the non-resonant "background" from diagrams 5.1.2 (III) and (IV). As can be seen, the predicted Dalitz plots for the Q-region (1.26 to 1.37 GeV/c^2) and the L-region (1.7 to 1.9 GeV/c^2) agree remarkably well with those obtained from our experiment.

Comparison of figs. 5.2.5 and 5.2.7 shows that our model is predicting rather too much $K^*(890)$ compared with $K^*(1420)$ in the decay of the L-meson. No doubt, this is because we have used a K^* trajectory with a linear imaginary part (see fig. C4, Appendix C).

FIGURE 5.2.2

The $K^-\pi^+\pi^-$ mass spectrum

$-t_{pp'} < 0.6$ GeV^2

Δ^{++} removed in $n(\pi^+p')$

3112 events in 40 MeV/c^2 bins

Dashed curve is the prediction of the model

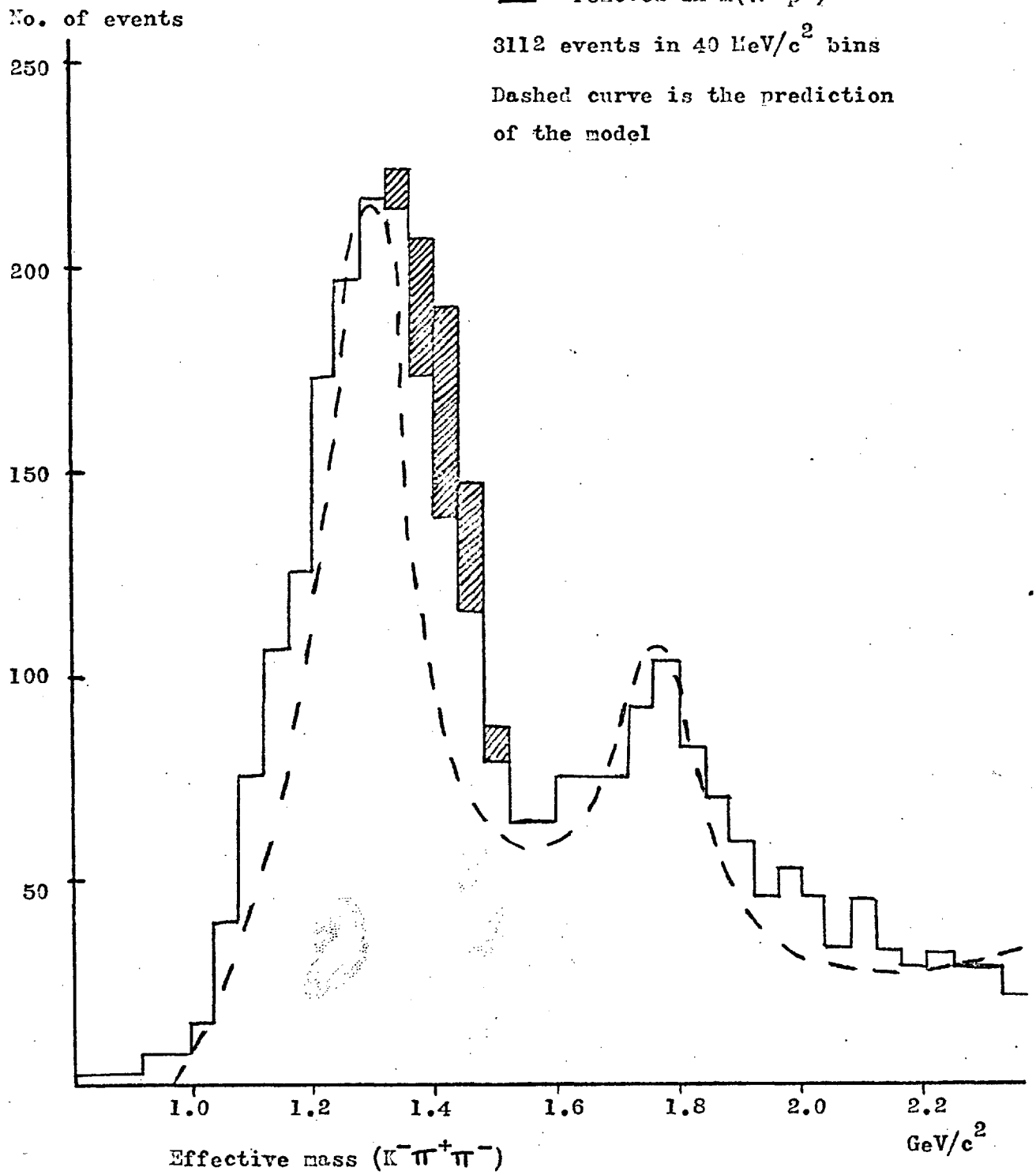

FIGURE 5.2.3

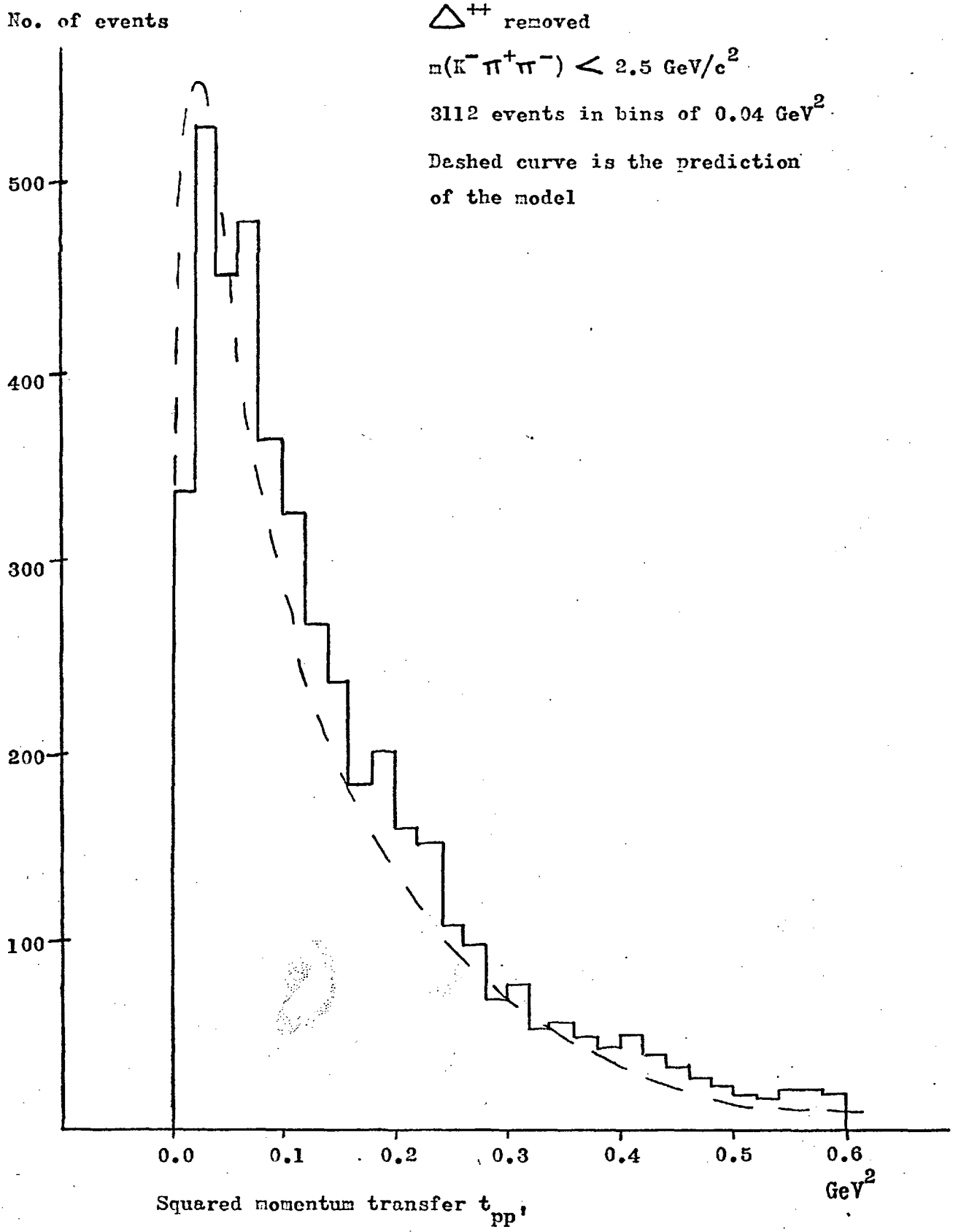
Distribution of $t_{pp'}$
Δ^{++} removed
$m(K^-\pi^+\pi^-) < 2.5$ GeV/c^2
3112 events in bins of 0.04 GeV^2
Dashed curve is the prediction of the model
No. of events
500
400
300
200
100
0.0
0.1
0.2
0.3
0.4
0.5
0.6
GeV^2
Squared momentum transfer $t_{pp'}$

FIGURE 5.2.4

Experimental Dalitz Plot for the Q-region

$1.26 < m(K^-\pi^+\pi^-) < 1.37$ GeV/c^2, $-t_{pp'} < 0.6$ GeV^2,

$\Delta^{++}(1236)$ removed. 713 events.

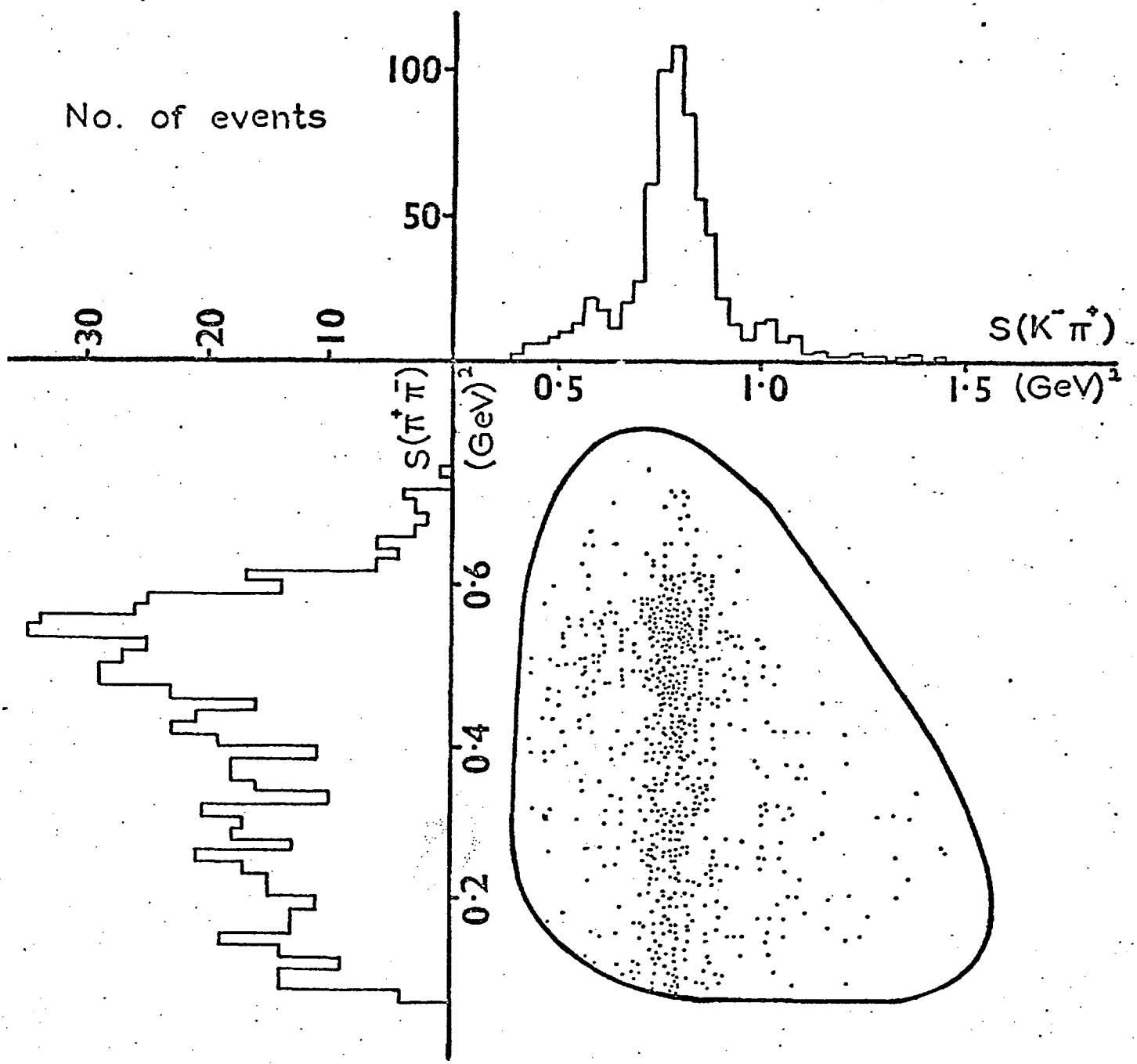

FIGURE 5.2.5

Experimental Dalitz plot for the L-region

$1.7 < m(K^-\pi^+\pi^-) < 1.9$ GeV/c^2 , $-t_{pp'} < 0.6$ GeV^2 ,

$\Delta^{++}(1236)$ removed. 462 events.

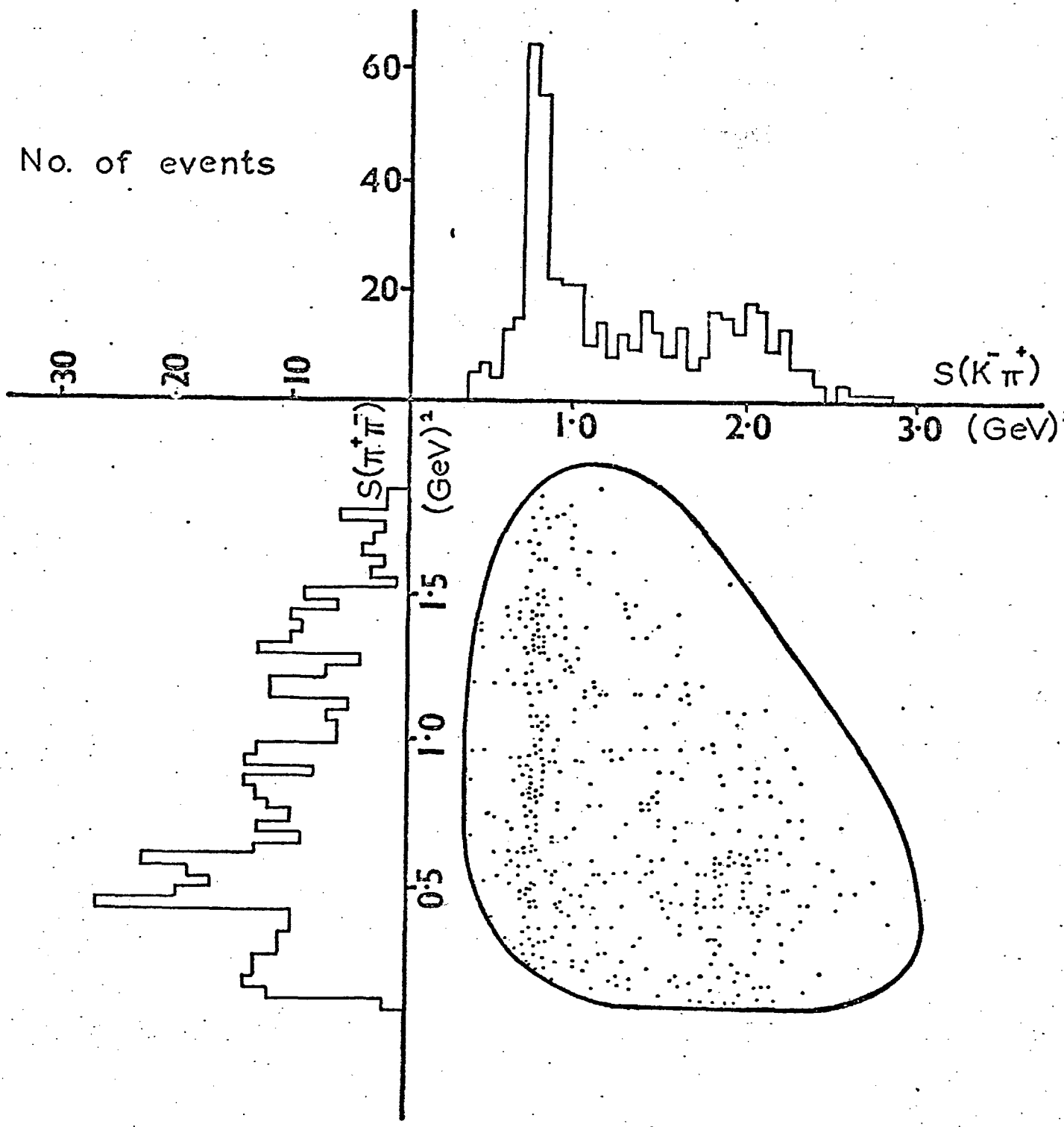

FIGURE 5.2.6

Predicted Dalitz Plot distribution for the Q-region

The contours represent densities of 10%, 40% and 70% of the density at the centre of the innermost contour

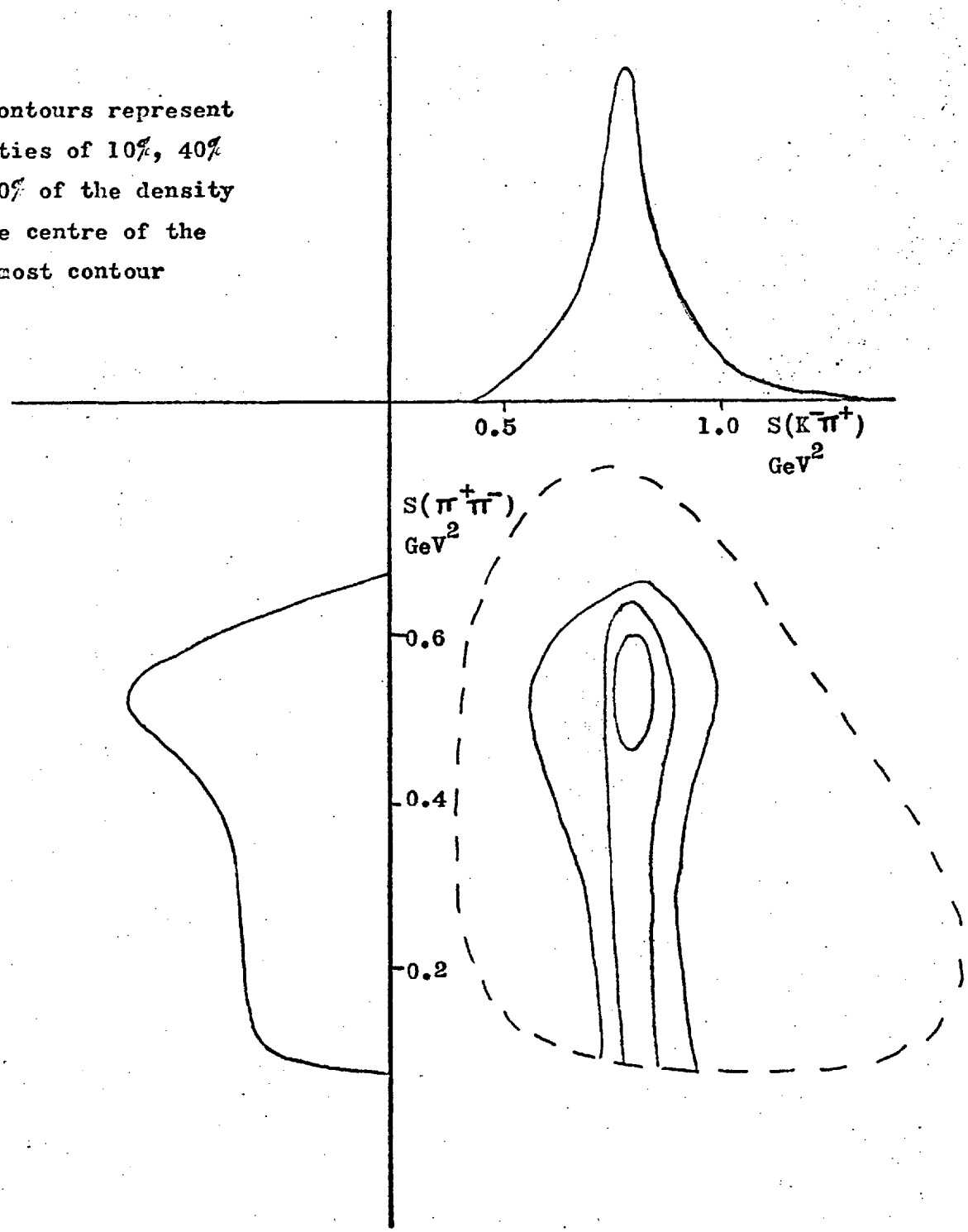

FIGURE 5.2.7

Predicted Dalitz Plot Distribution in the L-region.

The contours represent densities of 10%, 40% and 70% of the density at the centre of the innermost contour

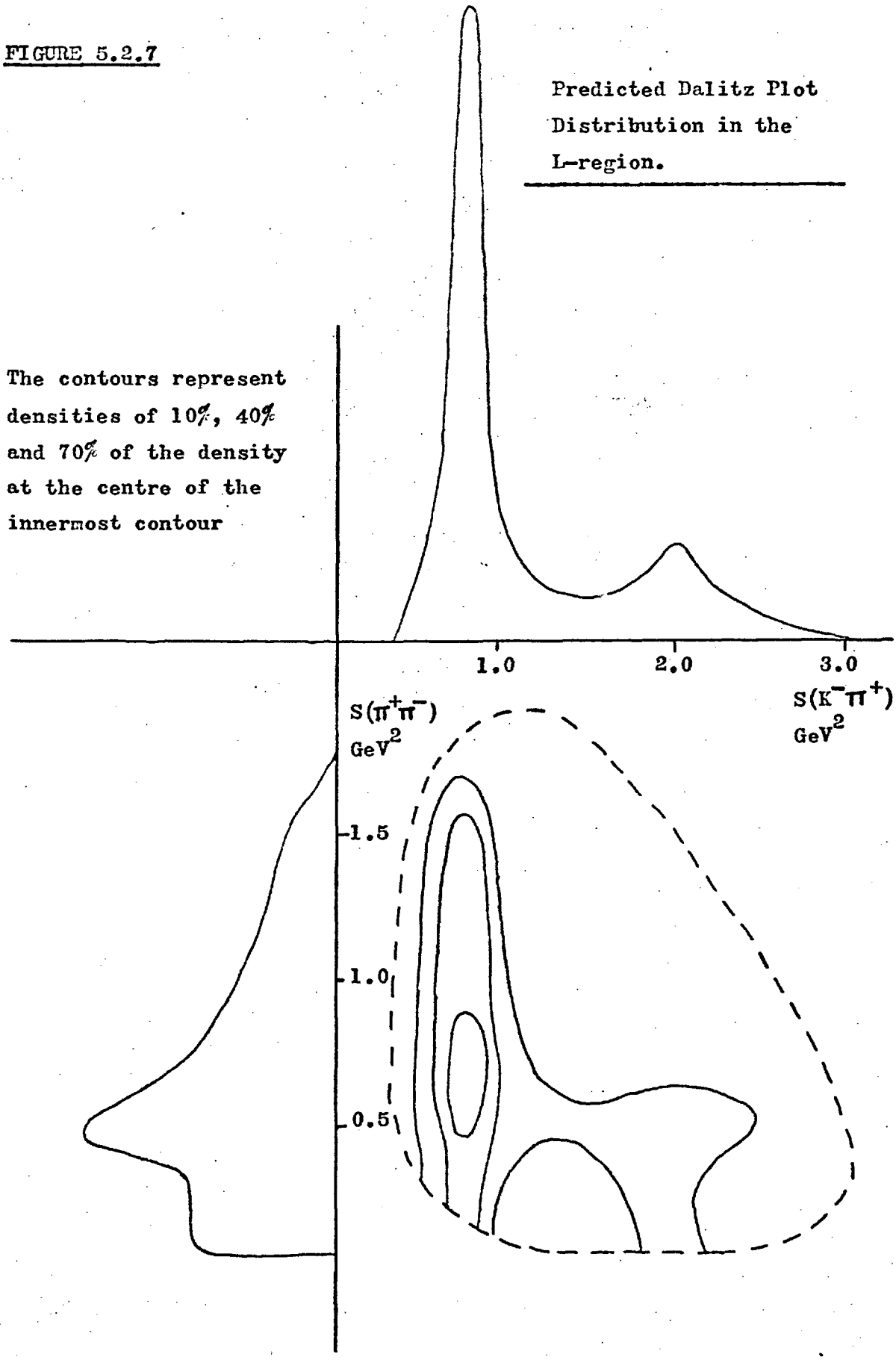

Further Results

We have already seen (fig. 5.2.3) that the prediction of our model is in rough agreement with the experimental distribution of the squared four-momentum transfer from the target to the outgoing proton. As a more stringent test of the model, we investigate here the distributions of t'_{pp} for different regions of the $\bar{K}\pi\pi$ effective mass spectrum. By t' we mean the quantity $t-t_{min}$, where t_{min} is the smallest momentum transfer that can occur with production of a $\bar{K}\pi\pi$ system with the effective mass considered.

Both our experimental and theoretical t' distributions are fitted to the expression

$$\frac{d\sigma}{dt'} = \text{Constant} \cdot \exp(At') \qquad (5.5)$$

In Ref. 1.11 it was pointed out that our data show a rapid decrease in the "slope" A as $m(\bar{K}\pi\pi)$ increases. This data is shown in figure 5.2.8 together with the predictions of our model. The errors on the theoretical points on this figure arise essentially from the statistical uncertainty which comes from performing a Monte-Carlo integration over phase space (using the progral FOWL) in a finite time.

Our procedure for deriving the predicted values of A was to obtain t'-distributions for ten $m(\bar{K}\pi\pi)$ regions three times each, plot these t'-distributions logarithmically, and have all thirty independently fitted by eye to eqn. 5.5. We then took the averages of each set of three values of the slope A, and derived errors from the spreads in value.

As can be seen from fig. 5.2.8, both the data and the prediction of the model indicate that A varies almost linearly with the $\bar{K}\pi\pi$ effective mass up to the highest masses considered. Furthermore, the lines have almost equal slopes. This, in itself, is a remarkable success.

FIGURE 5.2.8

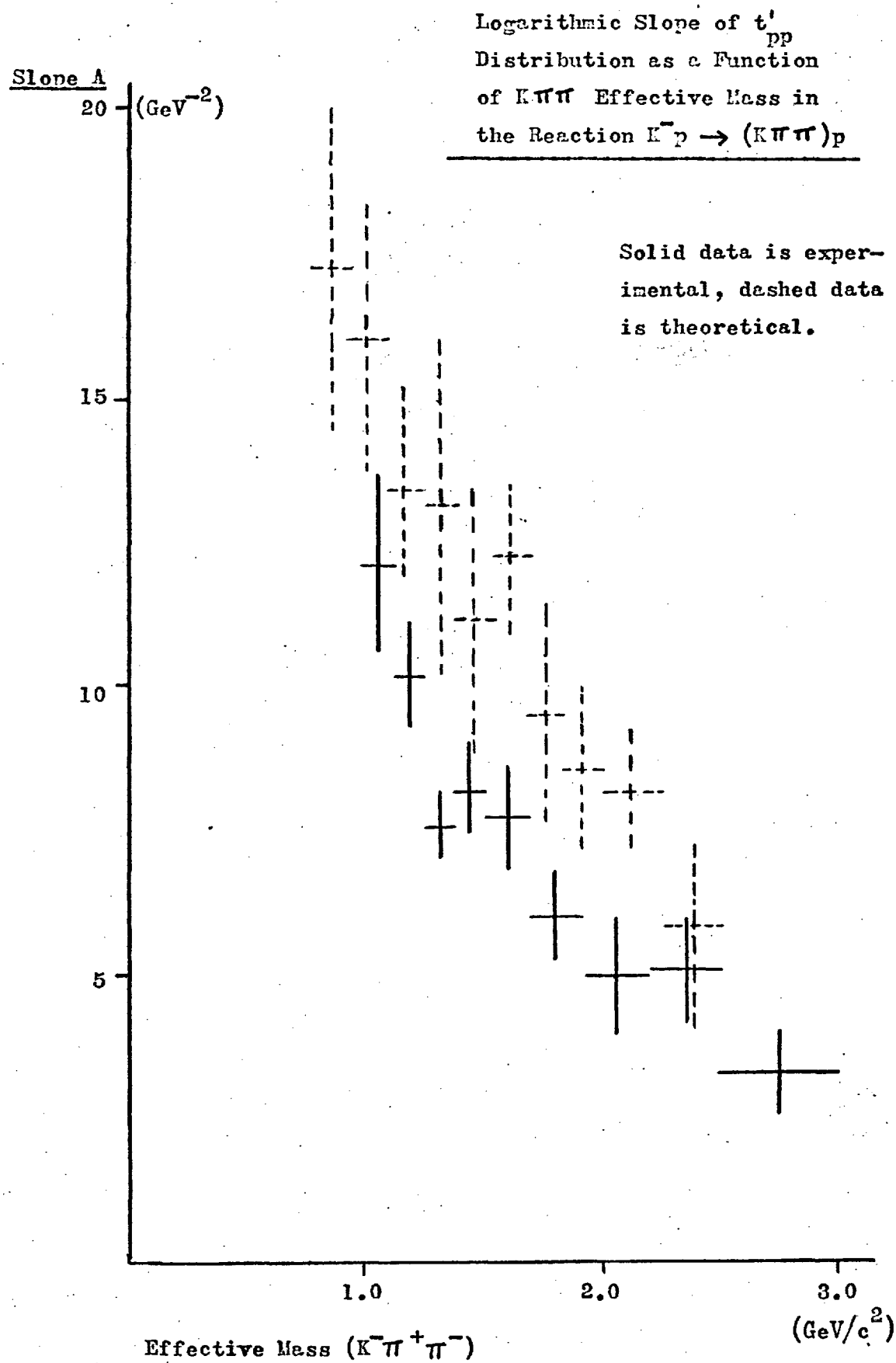
Logarithmic Slope of t'_{pp} Distribution as a Function of $K\pi\pi$ Effective Mass in the Reaction $K^-p \rightarrow (K\pi\pi)p$
Solid data is experimental, dashed data is theoretical.
Slope A
20
15
10
5
(GeV^{-2})
1.0
2.0
3.0
(GeV/c^2)
Effective Mass $(K^-\pi^+\pi^-)$

It was not to be anticipated a priori that our model would lead to predictions in agreement with experiment over a range of values of t'_{pp}. The Veneziano model was proposed only with fixed-mass external particles in mind; and yet when the "mass" of the Pomeron varies our result suggests that the B5 functions take this correctly into account.

Of course, the slope of our t' distributions is to some extent "input" to the model through the factor F in eqn. 5.2. However, as fig. 5.2.8 shows, this slope varies considerably from the "input" value of 7.7 GeV^{-2} as $m(\bar{K}\pi\pi)$ varies. Note that the theoretical slopes are consistently and uniformly higher than those found experimentally. We would not have found this discrepancy if we had used a slightly lower slope in eqn. 5.3 — say 4.5 instead of 7.7 GeV^{-2}. Now, 7.7 GeV^{-2} is the slope appropriate to elastic K^-p scattering, and contains both a ppP and a KKP "form factor". If we had decided just to make allowance for the ppP vertex, the appropriate slope would have been half of that found for pp elastic scattering. This is, in fact, about 4.5 GeV^{-2}. So, it seems possible that we should have used this lower slope for the parameter A in eqn. 5.3, and that the function V takes care of the top vertex in every respect, including the exponential dependence on the Pomeron "mass". In this context, we should point out that Pokorski and Satz (Ref.5.1) used only a ppP form factor (i.e. half the pp elastic slope) in their analysis of the $pp \rightarrow pn\pi^+$ reaction.

An important general property of Pomeron exchange reactions, which we have not yet mentioned in this chapter, is that as the beam particle momentum is raised above the threshold value for the reaction the cross-section seems to remain approximately constant. This has been found for a number of inelastic diffractive processes and is a well-known feature of high-energy elastic scattering.

Our model will obviously predict a flat cross-section for Q-meson production, because of the assumption of factorisability

and the use of an "S-factor" which corresponds to a flat Pomeron trajectory with unit intercept. Furthermore, it is (as we have already mentioned) implicit in our model that the reactions $K^-p \rightarrow Q^-p$ and $K^+p \rightarrow Q^+p$ should behave identically.

To test the validity of these assumptions (which are not, of course, unique to our model) we have compiled the Q-meson productions found in a number of K^-p and K^+p experiments. The results are shown in figure 5.2.9.

These cross-sections are taken from Refs. 5.7 to 5.18. We would like to point out that very few of these authors actually quote cross-sections for Q-production, and that to derive them from the published information is a difficult business which often involves counting events from published mass spectra. This involves uncertainties which are reflected in the errors shown on figure 5.2.9. Any innacuracies in the cross-sections shown are our responsibility rather than that of the authors of the papers to which we refer.

Figure 5.2.9 shows that the Q^- and Q^+ production cross-sections must rise sharply from the threshold beam momentum, quickly reaching a level of about 0.5 millibarns which then seems to remain constant. Also, we notice no significant difference between the Q^- and Q^+ cross-sections. These results, though not unexpected, are encouraging and in accord with the built-in requirements of our model.

So far in this Chapter we have concentrated on the $K^-p \rightarrow (K^-\pi^+\pi^-)p$ reaction, but our dual diffractive model is equally well applicable to the other charge configurations of the produced $\bar{K}\pi\pi$ system. Events of the type $K^-p \rightarrow K^-\pi^0\pi^0p$ cannot be fitted in the bubble chamber, so we have no data on this charge state; but we do have data on the reaction $K^-p \rightarrow K^0\pi^-\pi^0p$, and we have applied our model to this.

In writing down a Veneziano amplitude for the $K^-_{in}PK^0\pi^-\pi^0$ vertex, eight different dual diagrams must be taken into account.

FIGURE 5.2.9.

Cross-section for Ω production in $K^{+}p \rightarrow \Omega^{+}p$ as a function of incident kaon momentum.

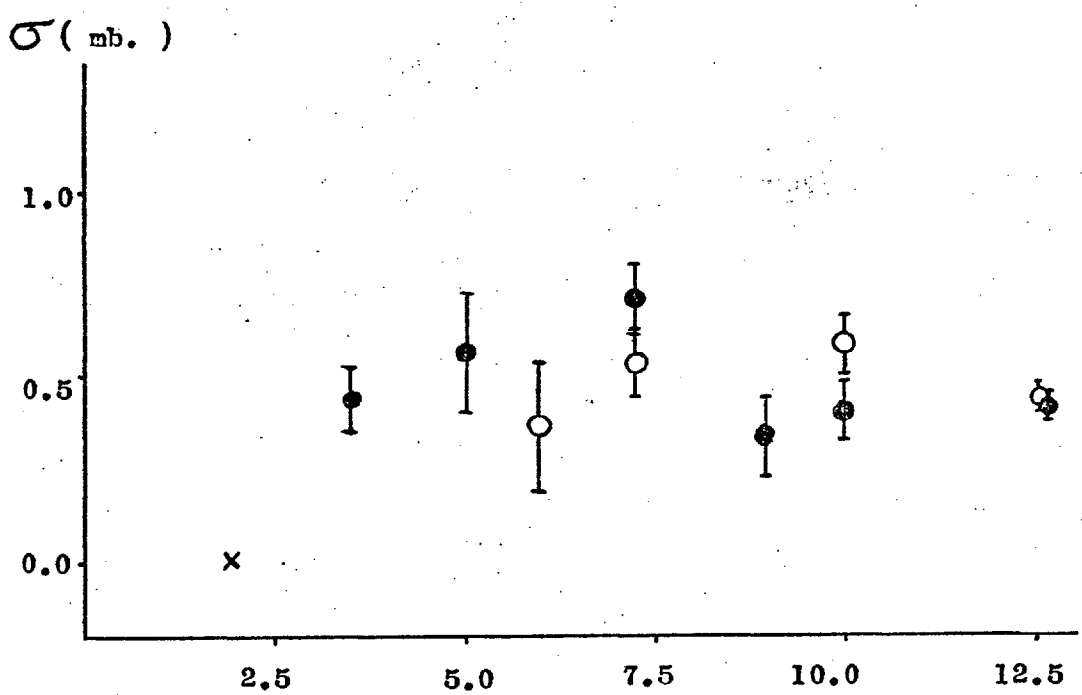

● = Ω^{+} data point

○ = Ω^{-} data point

× = threshold point

These are shown in figure 5.2.10, to be compared with the four diagrams (fig. 5.1.2) needed for $K^-_{in} P K^- \pi^+ \pi^-$. The amplitude is given by

$$V = \frac{1}{\sqrt{2}} \cdot (V_I + V_{II} + V_{III} + V_{IV} - V_V - V_{VI} - V_{VII} - V_{VIII})$$

where each V_i is a function of the form of eqn. 5.4. The terms $V_I - V_{IV}$ have the same sign and weight for the same reasons that the four graphs of fig. 5.1.2 have the same sign and weight. Similarly, the terms $V_V - V_{VIII}$ have the same sign and weight. The difference in sign between these two sets of terms arises essentially because the interchange of two pions which are in an I=1 state must lead to a change in sign of the amplitude. The factor of $1/\sqrt{2}$ comes from Clebsch-Gordan coefficients, bearing in mind that no exotic I-spins are allowed in any channel.

The amplitude above leads to a predicted $\bar{K}\pi\pi$ mass spectrum which is very similar to that found in the $K^-\pi^+\pi^-$ case, and indeed the data are very similar(fig. 4.2.3 (a) and (b)). More important, we can predict the branching ratio

$$R = \frac{\sigma(Q \rightarrow K^-\pi^+\pi^-)}{\sigma(Q \rightarrow K^0\pi^-\pi^0)}$$

where the Q region is defined by $m(\bar{K}\pi\pi) < 1.5$ GeV/c^2, and $-t_{pp} < 0.6$ GeV^2. This prediction is that $R = 1.14 \pm 0.12$, and is in excellent agreement with the experimental value of 1.06 ± 0.06. (This experimental result is taken from Chapter 4.)

FIGURE 5.2.10 Dual Diagrams for the $K^-_{in} P K^0 \pi^- \pi^0$ Vertex.

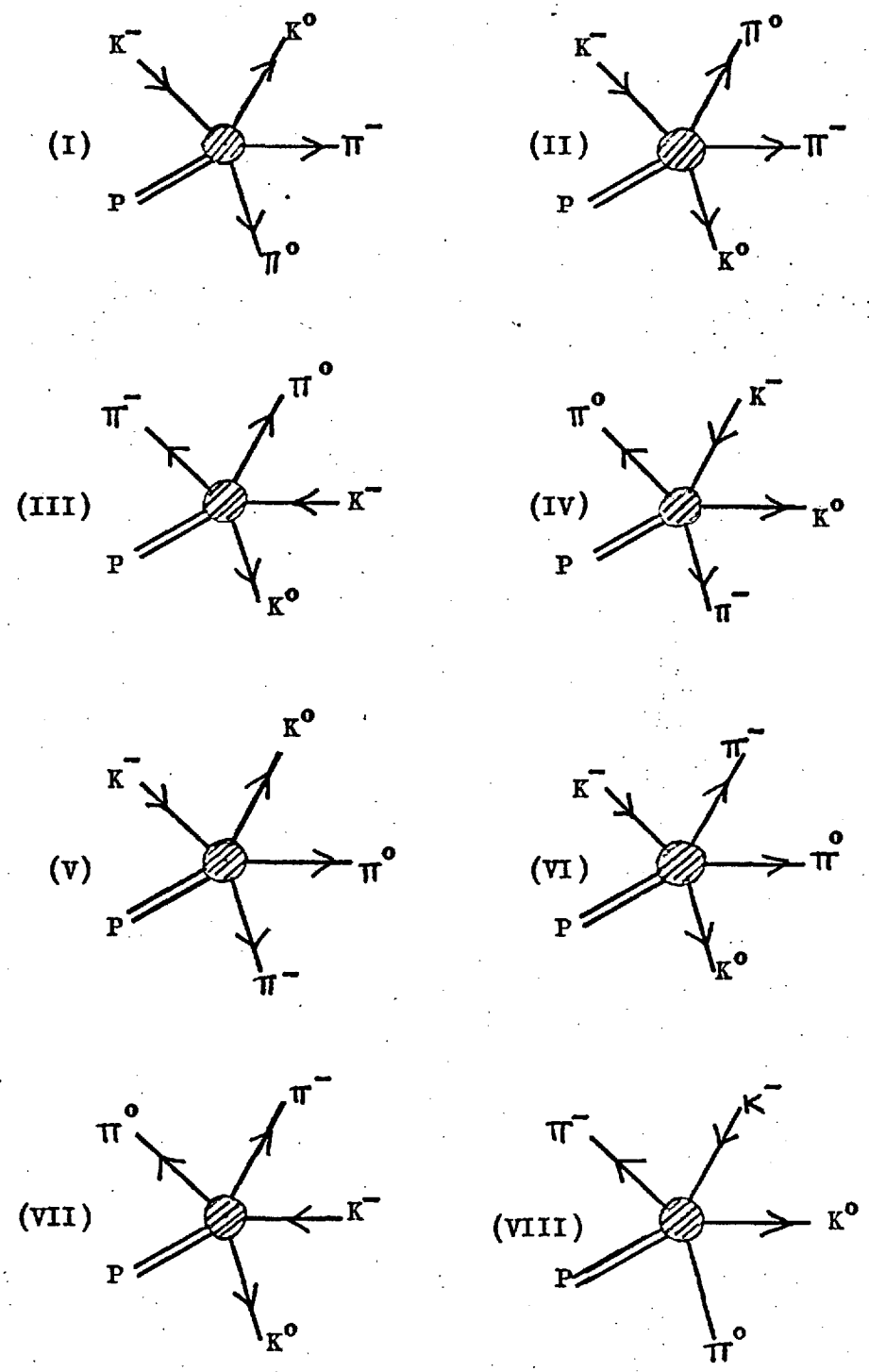

5.3 CONCLUSIONS

The obvious drawback of the dual diffractive model that we have described is that the Pomeron is treated (as regards the top vertex of fig. 5.0.1) as if it were a scalar particle. But the Pomeron is certainly not a scalar particle — for most purposes it is more accurately to be regarded as having spin = 1, and the factor S in eqn. 5.2 is designed to "patch up" our model in this respect.

This gives our model an unavoidable hybrid appearance. The Pomeron cannot be incorporated as a trajectory in the Veneziano model, and should not be regarded as a particle in any real sense. So, we construct our function V in eqn. 5.2 treating the Pomeron in the simplest way possible, i.e. as a scalar object with the quantum numbers of the vacuum. We then write down the functions S and F to take account of the behaviour of the Pomeron as known from elastic scattering.

Judged in this light, the success of our model indicates that to treat the Pomeron as though it were a particle (with the properties established from elastic scattering) is an adequate description of it even in the case of inelastic diffraction.

To give more insight into the nature of the Q-meson itself, and its $K^-\pi^+\pi^-$ decay Dalitz plot, we have derived in Appendix B the residue of the function V at the pole corresponding to $m(\bar{K}\pi\pi) = m(Q)$. The residue function is eqn. B13, which we can write as

$$\text{Res}(Q) = -2\alpha'.(p_{K^-_{in}} \cdot p_{\pi^+}) \cdot \frac{\Gamma(1-\alpha_{K^-\pi^+}).\Gamma(1-\alpha_{\pi^+\pi^-})}{\Gamma(2 - \alpha_{K^-\pi^+} - \alpha_{\pi^+\pi^-})}$$

$$-\alpha' t_{pp'} \cdot \frac{\Gamma(1-\alpha_{K^-\pi^+}).\Gamma(1-\alpha_{\pi^+\pi^-})}{\Gamma(1 - \alpha_{K^-\pi^+} - \alpha_{\pi^+\pi^-})} \qquad (5.6)$$

We will discuss in turn the two terms of eqn. 5.6.

In the first term, the factor ($p_{K^-_{in}} \cdot p_{\pi^+}$) has an obvious significance when we realise (by considering the rest frame of the Q) that $p_{K^-_{in}}$ is simply the polarisation vector of the Q-meson, and similarly that p_{π^+} is the polarisation vector of the K^* or ρ if $Q \rightarrow K^*\pi$ or $Q \rightarrow \rho K$. If the $K^*\pi$ and ρK couplings are S-wave, the first term is the same as that which follows from the work of Goebel et al. (Ref. 5.19) for a Q of spin-parity 1^+. In fact this was used by Goldsack and Otter (Ref. 5.20) to show that the Q decays into $K^*\pi$ or ρK by a predominantly S-wave coupling.

In short, the first term of eqn. 5.6 corresponds to the S-wave decay into 1^-0^- of a 1^+ Q-meson. It gives a Dalitz plot which differs only slightly from that of fig. 5.2.6, and we show in Appendix B (eqn. B15) that this corresponds to a strong $K^*(890)$ band in $s(K^-\pi^+)$ interfering constructively with a $\rho(765)$ band in $s(\pi^+\pi^-)$. There is a lot more K^* than ρ simply because the K^* is a narrower resonance than the ρ .

The second term of eqn. 5.6 has $t_{pp'}$ in its coefficient, i.e. its contribution is proportional to the four-momentum transfer from the proton. The three gamma-functions in this term form precisely the expression which is applicable to the interaction of four pseudoscalar particles (see for example Lovelace, Ref. 5.6). This term, therefore, describes a component of the Q with spin-parity 0^-, i.e. a daughter of the Q-meson.

The complete expression 5.6, then, descibes the decay of a pseudovector Q with an admixture of its pseudoscalar daughter proportional to the momentum transfer $t_{pp'}$.

To sum up: our model describes the diffractive dissociation of the kaon very satisfactorily, uniting the resonance and Deck-type descriptions of the process in a rather convincing way. It simultaneously explains the intrinsic properties of the Q-meson.

References (5)

5.1 S. Pokorski and M. Satz, Physical Review Letters 13, (1970) 113

5.2 M. Aderholz et al., Physics Letters 24B , (1967) 434

5.3 C. A. Savoy, Nuovo Cimento Letters 2 (1970), 870

5.4 G. Goldhaber, Physical Review Letters, 19, (1967)976

5.5 D.R.O. Morrison, Physical Review, 165, (1968) 1699

5.6 C. Lovelace, CERN preprint TH. 1041 (1969)

5.7 Q^+ at 3.5 GeV/c : Nuovo Cimento 49A, 374 and

5.8 Nuclear Physics B9, 403

5.9 Q^+ at 5.o GeV/c : Physics Letters 26B, 30

5.10 Q^- at 6.0 GeV/c : Nuovo Cimento 59A, 519

5.11 Q^- at 7.3 GeV/c : Physical Review 182, 1443

5.12 Q^+ at 7.3 GeV/c : Physics Letters 28B, 143

5.13 Q^+ at 9.0 GeV/c : Physical Review Letters, 19, 972

5.14 Q^- at 10.0 GeV/c : Nuclear Physics B8, 9

5.15 Q^+ at 10.0 GeV/c : "A Study of $\bar{K}\pi\pi$ States produced in 10 GeV/c K^+p Interactions", Birmingham-Glasgow-Oxford Collaboration Preprint, submitted to the 1970 Kiev Conf.

5.16 Q^- at 12.6 GeV/c : Physical Review Letters, 22, 731

5.17 Q^+ at 12.7 GeV/c : Physical Review D1? 78, and

5.18 CERN Hadron Conference (1968), II, 172

5.19 "Veneziano Model for $\pi\pi \rightarrow \pi$ S, Where S Has Arbitrary Spin and Parity", C.J. Goebel et al., Physical Review 182, 1487

5.20 "Veneziano Model Calculations for the Decay $Q \rightarrow K\pi\pi$ ", G. Otter and S.J. Goldsack, Imperial College Preprint.

CHAPTER 6

INELASTIC DIFFRACTION IN OTHER CHANNELS

In this Chapter we will investigate a few further reactions in which inelastic diffraction may take place. These are:

(i) $K^-p \rightarrow K^-K^+\Lambda$

(ii) $K^-p \rightarrow \Lambda\bar{p}p$

(iii) $K^-p \rightarrow K^{*o}(890)\pi^-\pi^-\Delta^{++}(1236)$

6.1 $K^-p \rightarrow K^-K^+\Lambda$

This is a "rare" channel in which we have fitted just 40 events. It is of interest because of the possible diffractive dissociation $p \rightarrow \Lambda K^+$. In figure 6.1.1 is shown the LPS angular distribution for these events, and it is clear from this that the Λ is always produced moving backwards, and the K^- forwards, in the C.M. frame. Most events have the K^+ moving forwards, along with the K^-, but there is a significant number of events (in the second sextant) with a backward-going K^+.

The effective mass distributions (not shown) show no significant structure except in the case of $m(K^+K^-)$, where 14 events form a very sharp peak at the $\phi(1019)$ mass. There is also a hint (6 events) of the f'(1514).

Resonant behaviour in the K^+K^- system, then, accounts for many of the events in the third sextant of fig. 6.1.1; but we are still left with those events where the K^+ is associated with the Λ. These cannot be identified with the effects of any particular N^* or Δ resonances, and although it seems likely that they arise from the dissociation of the proton, it is not possible to prove that this is diffractive in nature.

FIGURE 6.1.1

Longitudinal Momentum Phase Space Angle for $K^-p \rightarrow K^-K^+\Lambda$.

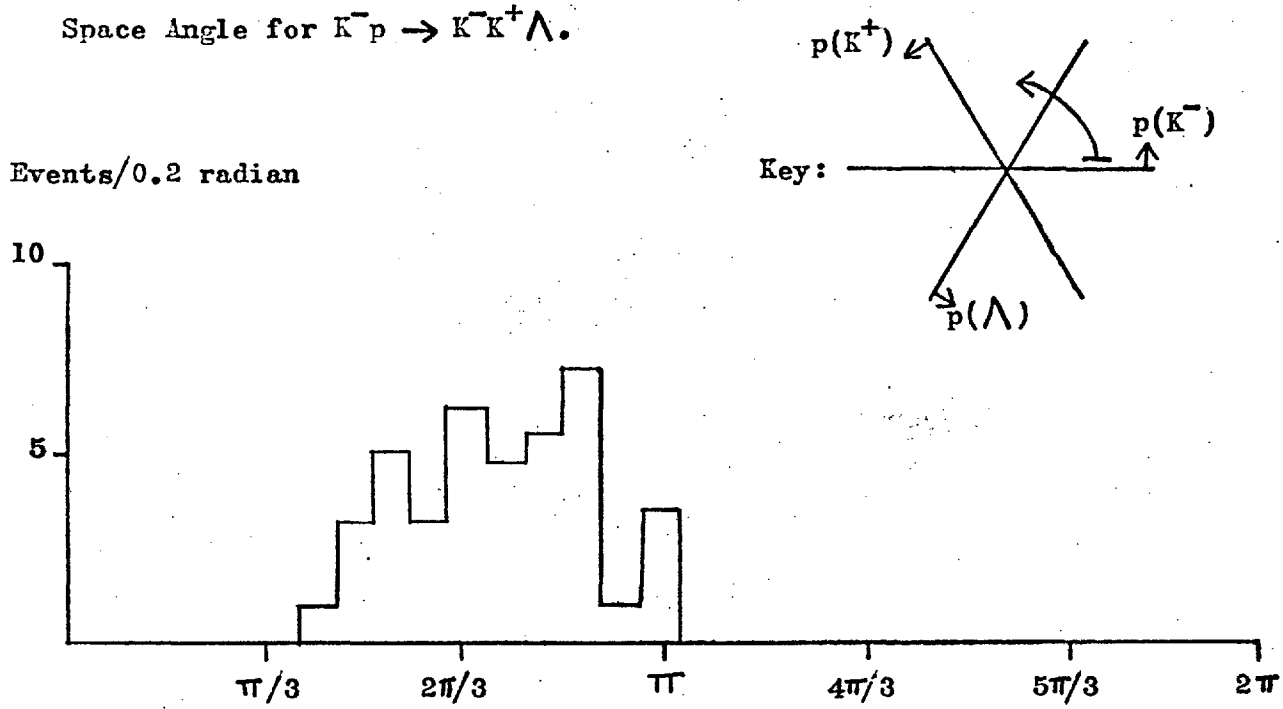

FIGURE 6.2.1

Longitudinal Momentum Phase Space Angle for $K^-p \rightarrow \Lambda\bar{p}p$.

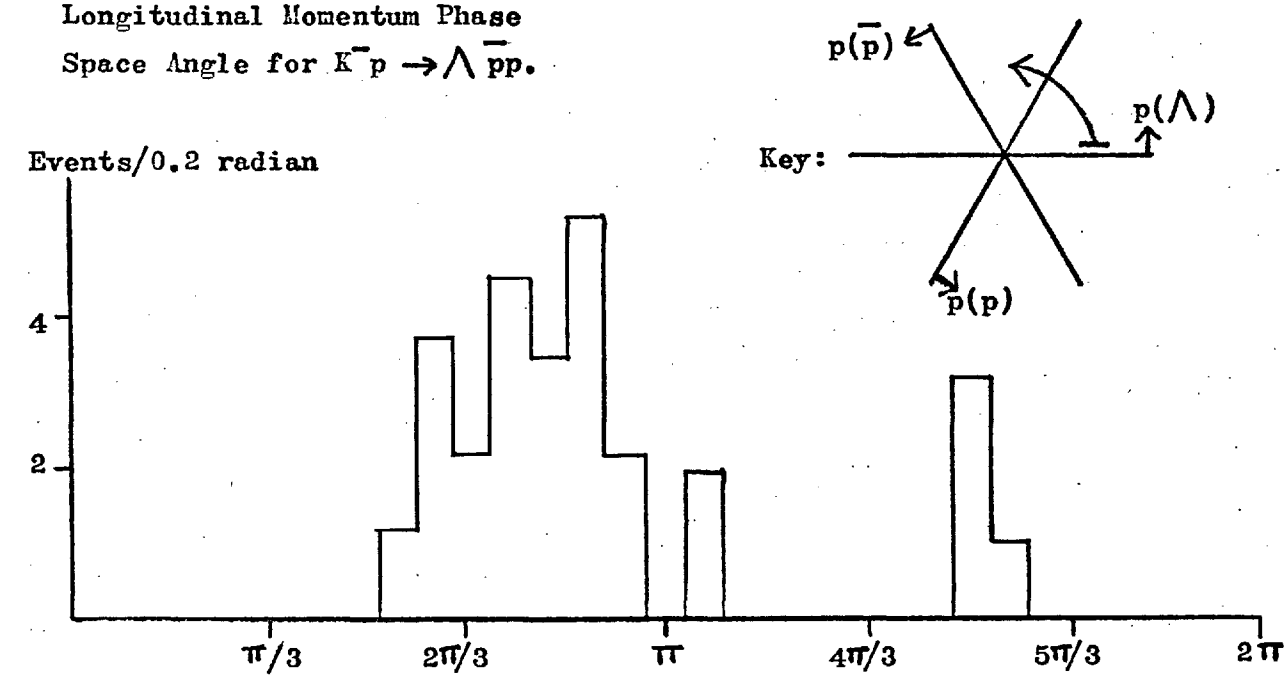

6.2 $K^- p \rightarrow \Lambda \bar{p} p$

Another "rare" channel, there are only 28 events from our experiment fitted to this reaction. The LPS angular distribution of figure 6.2.1, however, shows up some interesting features of this data. The majority of the events lie in the third sextant, with a backward proton and forward $\bar{p}$ and Λ in the CM frame. This is highly suggestive of the dissociation process $K^- \rightarrow \bar{p}\Lambda$.

We also notice four events in the fifth sextant, well separated in phase space from the other events. These have a backward-going Λ, while the proton and antiproton are moving forward with almost equal momenta. Although only four events are involved, we cannot escape the conclusion that strange meson exchange is playing its part here.

The effective mass plots (not shown) contain no discernible resonance peaks — hardly surprising with such low statistics. If we accept that we have observed the diffractive dissociation $K^- \rightarrow \bar{p}\Lambda$, then we should (if crossing symmetry holds at our diffractive vertices) expect the dissociation $p \rightarrow \Lambda K^+$ also to occur. Thus, the results of the previous section and of this section are together compatible with the hypothesis that diffractive dissociation is being observed. Since we have about 0.2 microbarns per event, the cross-sections involved here are about two orders of magnitude less than those found for diffractive dissociation processes in previous Chapters.

6.3 $K^- p \rightarrow K^{*o} \pi^- \pi^- \Delta^{++}$

We have already pointed out (in Chapter 4) that the diffractive dissociations

$$K^- \rightarrow K^- \pi^+ \pi^- \tag{6.1}$$

and

$$p \rightarrow p \pi^+ \pi^- \tag{6.2}$$

are seen to occur abundantly in our data on the reaction

$$K^- p \rightarrow K^- \pi^+ \pi^- p \, . \tag{6.3}$$

The purpose of this section is to investigate the simultaneous occurence of the dissociations 6.1 and 6.2 above; such a double diffractive dissociation process (DDD) will contribute to the channel

$$K^- p \rightarrow K^- \pi^+ \pi^- \pi^+ \pi^- p \, . \tag{6.4}$$

In fact we will restrict our attention to a subset of the above channel, namely the quasi-four-body events of the type

$$K^- p \rightarrow K^{*o}(890) \pi^- \pi^- \Delta^{++}(1236) \tag{6.5}$$

selecting such events from our data by the cuts

$$0.82 < m(K^- \pi^+) < 0.96 \text{ GeV}/c^2 \tag{6.6}$$

and

$$1.12 < m(p \pi^+) < 1.34 \text{ GeV}/c^2 . \tag{6.7}$$

We require that 6.6 is true for one of the π^+'s, and that 6.7 is only true for the other π^+.

Our reasons for making these selections are as follows:

(i) The $K^{*o}(890)$ and $\Delta^{++}(1236)$ resonances are very strongly produced in processes 6.1 and 6.2; we expect that this will also be the case in DDD.

(ii) Strong production of the K^* and Δ are in fact indicated by the $K^- \pi^+$ and $p \pi^+$ effective mass spectra for reaction 6.4. Out of 1427 fits, we have about 900 K^*'s and as many Δ's. When we examine the $m(K^- \pi^+)$ vs $m(p \pi^+)$ triangle plot (not shown), we find that the numbers of events in and around the $K^* - \Delta$ overlap region imply that there is no significant interference between these resonances. In other words, the triangle plot distribution function factorises in this region.

(iii) Of our 1427 fits to reaction 6.4, 327 are incorrect and arise

from ambiguities in distinguishing the final-state K^- from the π^-'s. However, the proportion of misfitted events will be much less when we select a sharp resonance such as the K^*.

(iv) We remove from our sample events corresponding to a host of nondiffractive reactions, and to the single diffractive dissociation reactions $K^-p \rightarrow (K^-4\pi)p$ and $K^-p \rightarrow K^-(4\pi p)$.

(v) Above all, the analysis and simulation of the data is considerably simplified when we restrict ourselves to quasi-four-body events.

We have 172 events of the type 6.5. The C.M. longitudinal momentum distributions of the particles are shown in figure 6.3.1, and the preponderance of forward K^*'s and backward Δ^{++}'s indicates (as we would expect) that the reaction is peripheral as regards strangeness and baryon number. On the other hand, the pions have a distribution peaking at zero in which it is impossible to distinguish separate forward and backward peaks.

Our aim here is to see if the data can be explained by the process of figure 6.3.2(a), and we have tried a number of different recipes for "sorting" the two pions. We find that there is no way of doing this cleanly. In particular, there is no statistically significant correlation between the C.M. frame directions of the two pions. For this reasons, we are obliged to show two combinations of particles per event in the $K^*\pi^-$ and $\Delta\pi^-$ effective mass spectra, which are given in figure 6.3.3.

It is interesting to compare these mass spectra with those in figures 4.3.2(b) and 4.3.3(b), i.e. with the $K^{*o}\pi^-$ and $\Delta^{++}\pi^-$ mass spectra found for single diffractive dissociation in the reaction (6.3) above. The two pairs of histograms are really quite similar, and this fact strongly suggests that the reaction (6.5) is diffractive in nature.

To check this, we have predicted the shapes of the histograms in figs. 6.3.1 and 6.3.3 under the assumption that reaction proceeds by DDD. These predictions are the dotted curves superimposed over

FIGURE 6.3.1 C.M. Longitudinal Momentum Distributions

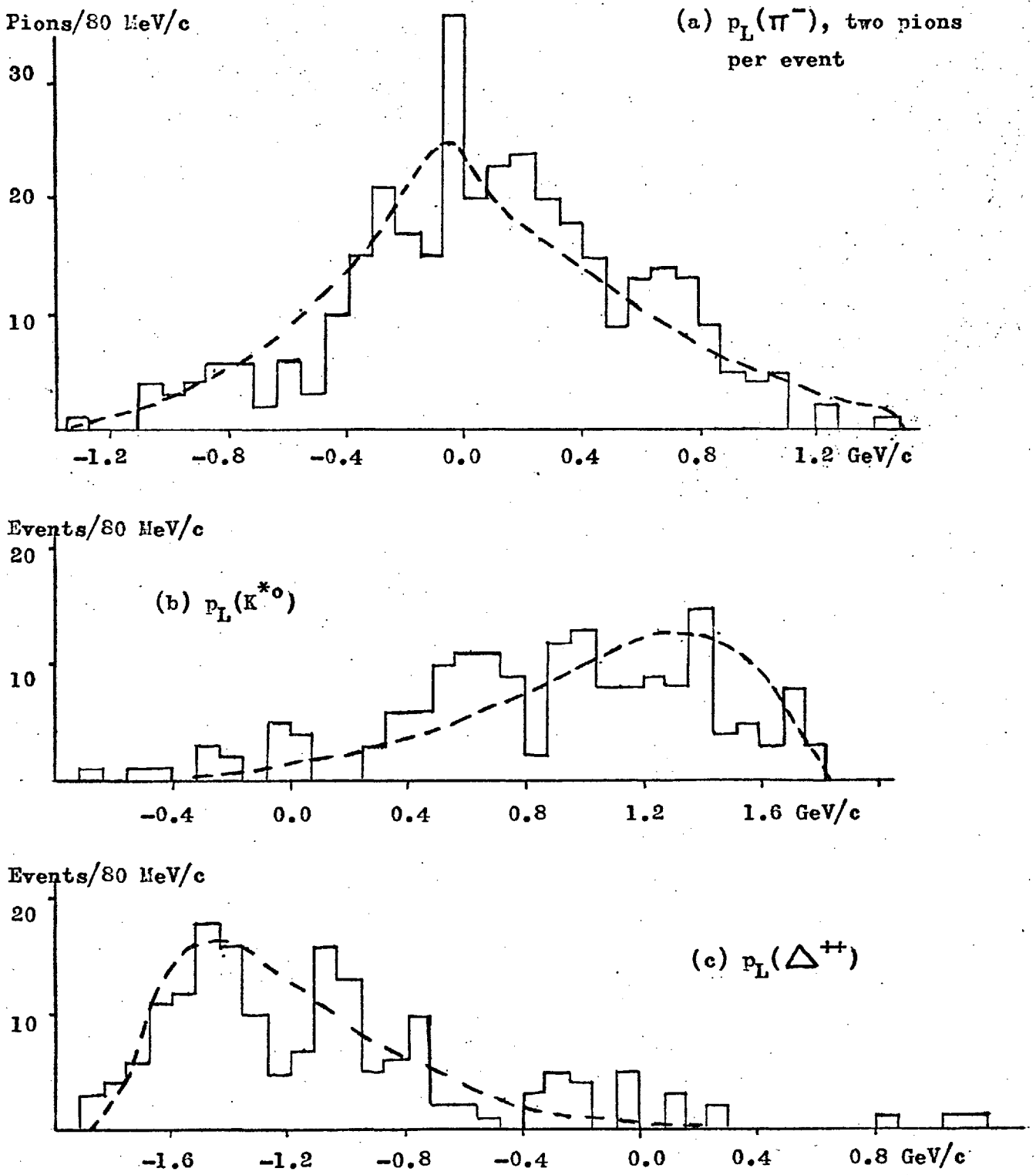

(Dotted curves are CLA Model predictions, see text)

FIGURE 6.3.2

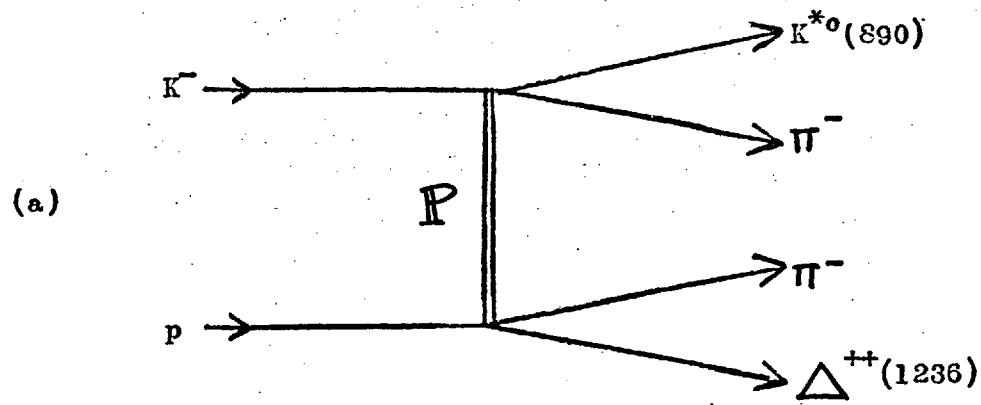

(b) Multiperipheral Graphs used in the CLA Model Calculation:

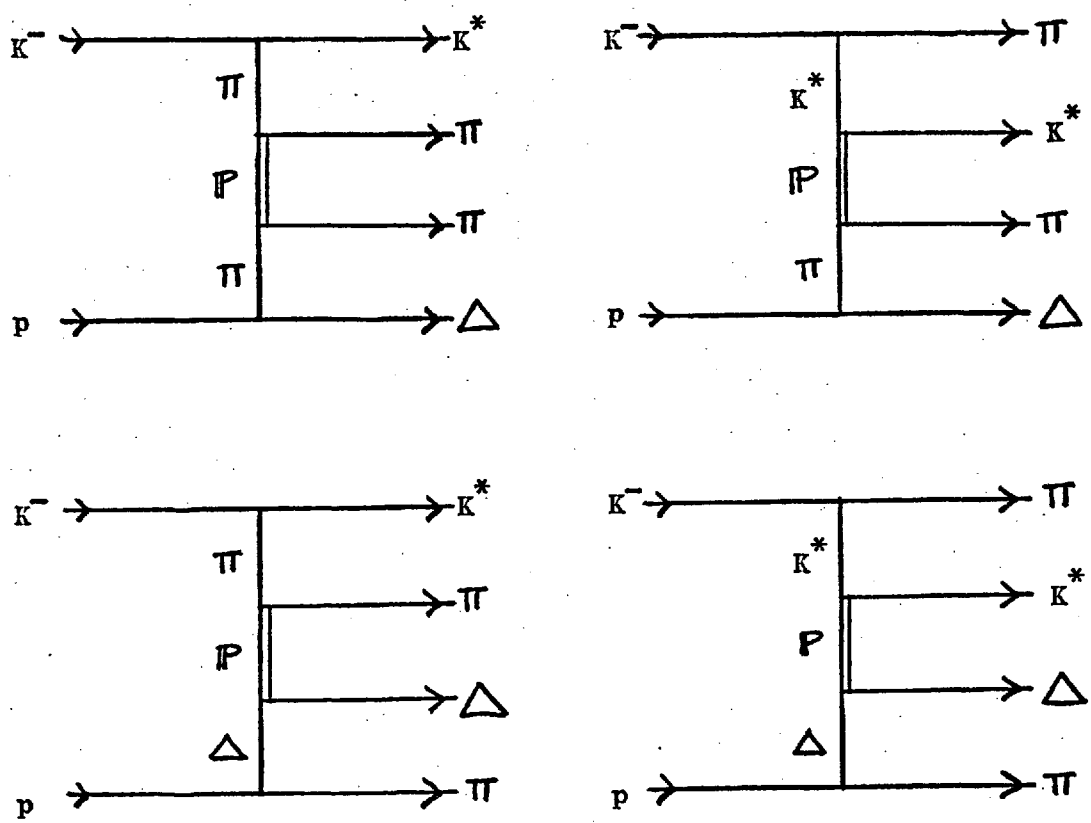

FIGURE 6.3.3 $K^{*o}\pi^-$ and $\Delta^{++}\pi^-$ effective mass distributions

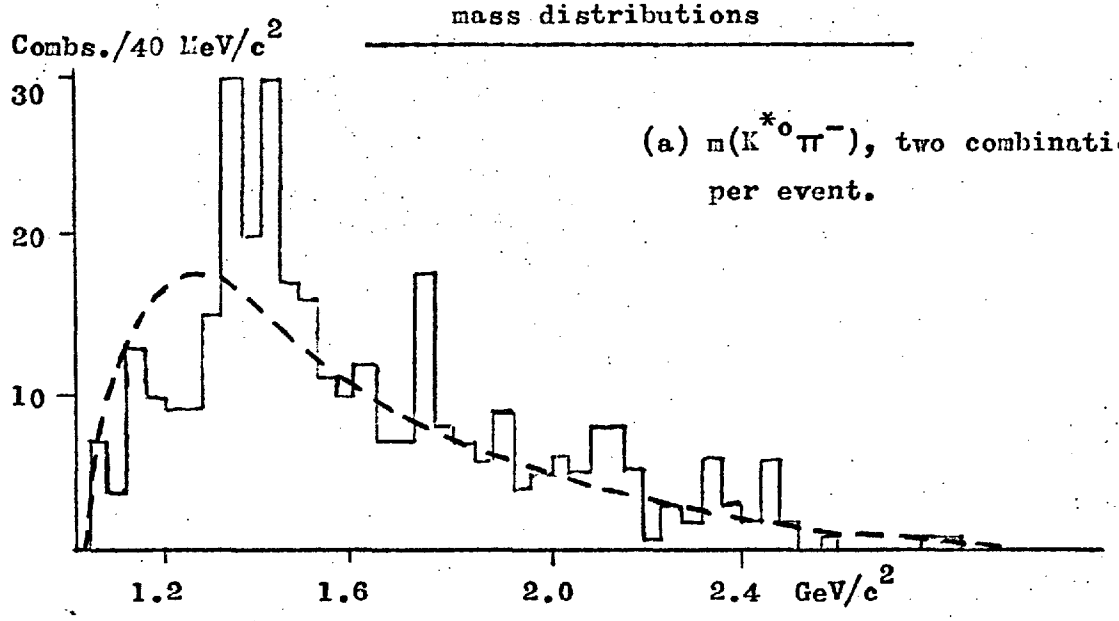

(a) $m(K^{*o}\pi^-)$, two combinations per event.

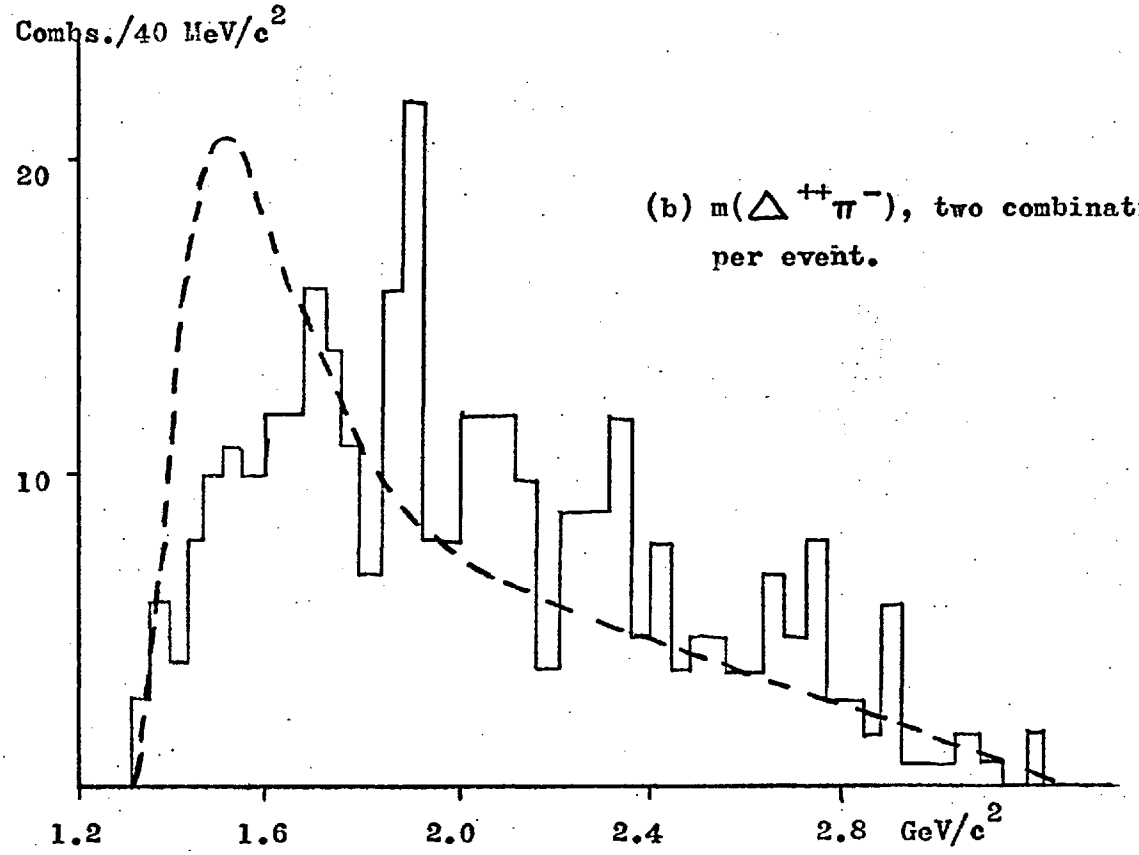

(b) $m(\Delta^{++}\pi^-)$, two combinations per event.

(Dotted curves are CLA Model predictions, see text)

those histograms. They were calculated using the multiperipheral model of Chan, Loskiewicz and Allison (Ref. 6.1), the "CLA Model." In this model, the overall amplitude is taken to be an incoherent some of contributions from the various multiperipheral graphs, which in this particular case are the graphs of figure 6.3.2(b).

The parameters used in calculating these graphs are the same as those suggested in Ref. 6.1, and which were also used in Ref.1.19. No absolute normalisation is given by the CLA model, are our curves are normalised to the total of the data in each case.

The CLA Model, with the Pomeron exchange graphs, gives a fairly good representation of the data. It is interesting to note that it falls short of fitting the effective mass spectra in precisely the same way (and for the same reason) as our Double-Regge-Exchange model calculations in Chapter 4 failed to fit the corresponding mass spectra there. (This reason is our failure to take proper account of resonances in the $K^*\pi$ and $\Delta\pi$ systems.)

Using our data on elastic K^-p scattering, and on inelastic diffraction in reaction (6.3), we can estimate the number of DDD events we might expect to find here by an argument which is presented diagrammatically in figure 6.3.4. We assume that the Pomeron exchange amplitudes can be factorised (in the simplest sense) and find that

$$\sigma_{QN} = \frac{\sigma_{Qp} \cdot \sigma_{KN}}{\sigma_{Kp}} \cdot \frac{p(QN).p(Kp)}{p(Qp).p(KN)} \cdot \qquad (6.8)$$

In this expression, Q and N refer to arbitrary narrow mass regions of the $K^{*o}(890)\pi^-$ and $\Delta^{++}(1236)\pi^-$ systems respectively, and the σ's are cross-sections for producing the suffixed final states from a fixed-energy K^-p initial state by Pomeron exchange. The p's are the magnitudes of the CM momenta of the (bracketed) final-state systems.

We calculate the right-hand side of eqn.(6.8) by taking the cross-sections given in Chapter 4, and using m_Q=1.5 and m_N=1.8 GeV/c^2 to calculate the momenta. The number of DDD events predicted to be in our data on reaction (6.5) then turns out to be 230.

FIGURE 6.3.4 Relating Double Diffractive Dissociation to Single Diffractive Dissociation and Elastic Scattering:

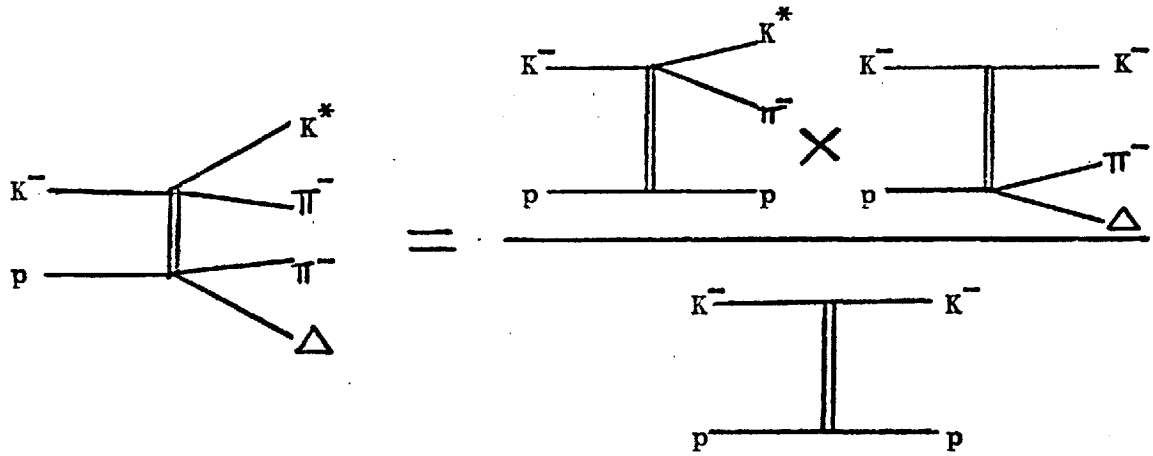

FIGURE 6.3.5 t-Distribution for Double Diffractive Dissociation:

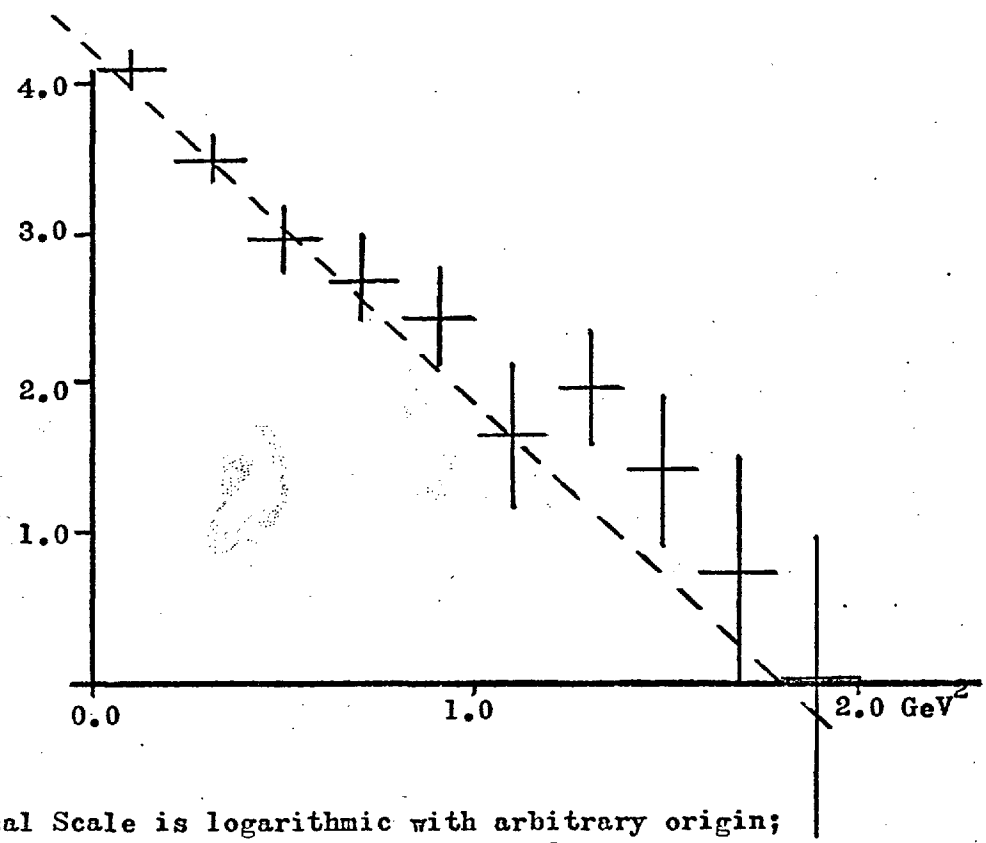

Vertical Scale is logarithmic with arbitrary origin;
Horizontal Scale is in bins of 0.2 GeV^2;
Dotted straight line has slope = 2.35 GeV^{-2}.

Our evidence that the data on reaction (6.5) arise from DDD can be summarised as follows:

(i) The number of events involved (172) is close to the number (230) suggested by the idea of Pomeron factorisability as shown in figure 6.3.4.

(ii) The longitudinal momentum spectra of fig. 6.3.1 are in good agreement with the predictions of the CLA model for DDD. In particular, our inability to distinguish between pions from the dissociation of the incident kaon and those from the dissociation of the target proton is to be expected.

(iii) The CLA model also enables us to describe the mass spectra of fig. 6.3.3 in the context of DDD.

(iv) Perhaps the most convincing evidence is the comparison of the mass spectra for single and for double diffractive dissociation. For example, fig. 6.3.3(a) shows a strong peak similar to the Q meson, and also a hint of the L meson.

Obviously, we have very strong circumstantial evidence to the effect that reaction (6.5) is dominated by Double Diffractive Dissociation. To prove this beyond doubt would require it to be shown that the cross-section for the process is almost independent of the beam momentum; unfortunately we cannot do this here.

Finally, in figure 6.3.5, we show the logarithmic t-distribution for our data. This is the squared four-momentum carried by the Pomeron; what we have actually plotted is, to be precise, the smaller value of $/t-t_{min}/$, this quantity having been calculated (for each event) for both orderings of the pions. t_{min} is the minimum value of t that can occur given the effective masses of the $K^{*}\pi^{-}$ and $\Delta\pi^{-}$ systems. In short, figure 6.3.5 is as sharp as it can be made, and its slope is to be taken as an upper limit.

This slope is found (by the "eyeball fit" superimposed on the graph) to be about 2.35 GeV^{-2}. This seems to be anomalously low in comparison to the diffractive scattering slopes we found in previous Chapters, but is not surprising when we bear in mind (a) the phase space in t in this case, and (b) the fact that we are essentially observing $\pi\pi$ elastic scattering as in the first graph of fig. 6.3.2(b).

6.4 CONCLUSIONS

In all three of the reactions we have studied here, we find strong indications that inelastic diffraction occurs. The cases $K^- \rightarrow \Lambda \bar{p}$ and $p \rightarrow \Lambda K$ are important in that all our other examples of inelastic diffraction have involved pion production. These cases are rare because of the high "mass lift" which must be given to the incident particles, and because of the low phase space volume for (e.g.) a decay $N^* \rightarrow \Lambda K$ in comparison with $N^* \rightarrow \Delta \pi$.

The occurence of double diffractive dissociation is expected on "factorisation" grounds, and it would be very remarkable if we did not observe it. We can say that the bulk of our data on the reaction $K^- p \rightarrow K^{*o}(890)\pi^-\pi^-\Delta^{++}(1236)$ are compatible with the hypothesis of DDD, with a cross-section of not much less than 30μb. (with $K^{*o} \rightarrow K^-\pi^+$).

Reference

6.1 Chan, Loskiewicz and Allison, Nuovo Cimento 57A, 93 (1968)

CHAPTER 7

ON THE NATURE OF INELASTIC DIFFRACTION

To understand inelastic diffraction, it is first of all necessary to understand elastic diffraction. So, in spite of this Chapter's title, we must begin it with a discussion of the elastic scattering of hadrons, a phenemenon which at medium and high energies is predominantly governed by Pomeron exchange.

7.1 ELASTIC SCATTERING

Our first problem is to clarify the meaning of the phrase "Pomeron exchange", or "diffraction", which we have used so liberally. The best approach to this is through the idea of diffraction as being the optical "shadow" of inelastic processes. To make progress, we have to make some sort of assumption about these inelastic processes, and at its simplest, this assumption might take the form of a statement about the size and "opacity" of the hadrons. This is the basis of the Optical Model, which enables us to relate the shapes of elastic scattering "t-distributions" to the spacial wave-functions of the hadrons (through a Bessel Transform). The Optical Model really comes into its own as a tool for investigating the structure of nuclei, but we will not find it fruitful for rationalising the behaviour of "elementary" particles in elastic scattering.

Here, we shall assume the principles of Duality and Unitarity; the former as embodied in the formalism of the dual resonance model. We will not commit ourselves to any particular algebraic representation for the reaction amplitudes, but assume that the relevant amplitudes have the properties of duality, crossing symmetry, etc. which are necessary to give meaning to their representation in terms of "dual diagrams".

All that we shall say in this context is only strictly true for mesons, which can be regarded (and drawn) as pairs of quarks. A reaction $ab \rightarrow X$, where X is an arbitrary system, can be drawn

in just two distinct ways, i.e. where a quark line is exchanged between a and b, and where this is not the case (and $X = X_1 + X_2$). These can be illustrated like this:

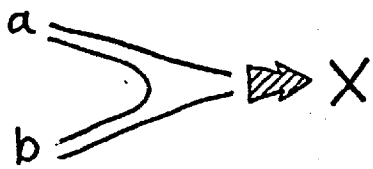

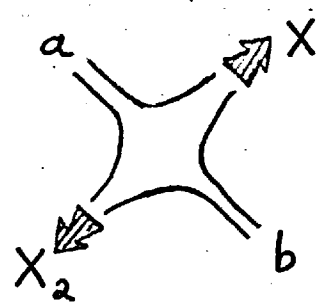

Note that the first of these implies the existence of resonances between the mesons a and b, whereas the second does not. We now invoke unitarity to express the forward elastic scattering amplitude between a and b as a sum over intermediate states, i.e.

$$\mathrm{Im}\langle ab|T|ab\rangle = \sum_X \langle ab|T|X\rangle\langle X|T^\dagger|ab\rangle \qquad (7.1)$$

This, of course, is no more than the familiar Optical Theorem. Expressed graphically, it is as follows:

$\langle ab|T|X\rangle =$

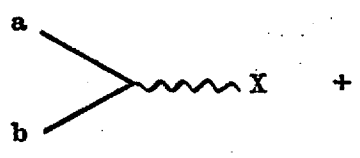

$+$

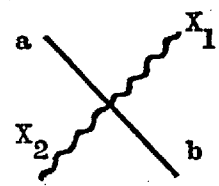

$=$

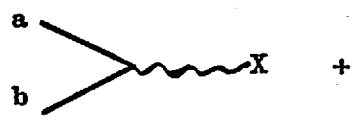

$+$

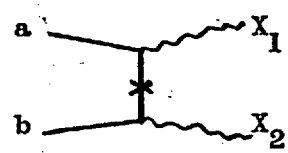

$\langle ab|T|X\rangle\langle X|T^\dagger|ab\rangle =$

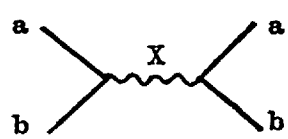

$+$

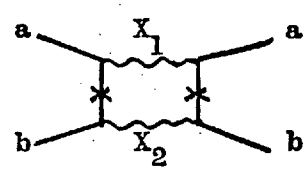

$\therefore\ \mathrm{Im}\langle ab|T|ab\rangle =$

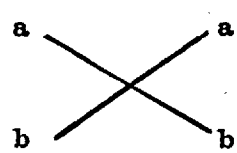

$+$

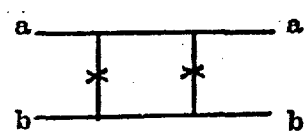

(7.2)

where we have introduced twisted propagators (denoted by a cross) and a non-planar loop diagram. (Ref. 7.1) The first term of eqn. (7.2) is no more than a simple four-point function, with reggeons

in both the s- and t-channels. It has nothing to do with the Pomeron, and will become insignificant at high energies. The second term, then, must account for the bulk of high-energy elastic scattering, i.e. diffractive scattering. Showing the quark lines, we can draw it like this:

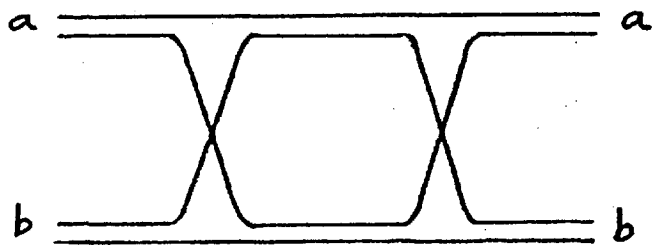

and it will be seen that there is no net exchange of quarks between a and b. So, this diagram represents the exchange of four-momentum, but no quantum numbers, and this exchange is not dual to any resonances in the s-channel. We will associate it with the Pomeron.

The arguments given above are oversimplified, and open to objections concerning, in particular, the nature of the summation over the intermediate states X. Some authors (Ref. 7.2) suggest that this diagram is simply the lowest-order term in a series of multi-loop graphs which together build up the Pomeranchuk singularity.

The non-planar graph above has been calculated (Ref. 7.3) by "sewing" reggeons, i.e. by joining together two legs of a six-point graph without loops, and also (Ref. 7.4) by Nielson's ingenious electrostatic analogue (Ref. 7.5). The results are in agreement with one another, but the amplitude found is exceedingly complicated, and there is a serious difficulty with its normalisation. The most significant finding is that the Pomeron behaves like a trajectory with slope equal to half the slope of normal Regge trajectories.

Having decided that the Pomeron is to be represented by a particular dual diagram, we must ask ourselves how we should interpret diagrams where this Pomeron occurs more than once. In figure 7.1.1 we show pairs of Pomerons in "series" and in "parallel", and

FIGURE 7.1.1

(a) 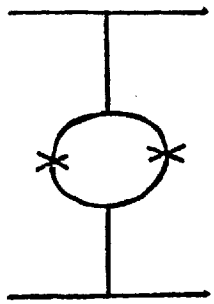 = Pomeron Exchange

(b) 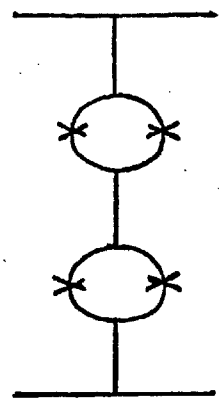 = 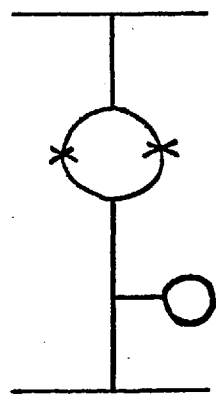

(c) 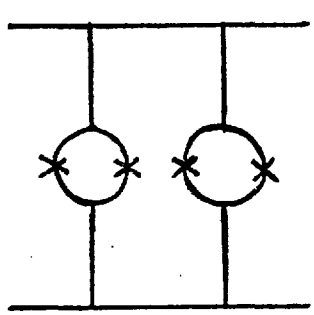 = 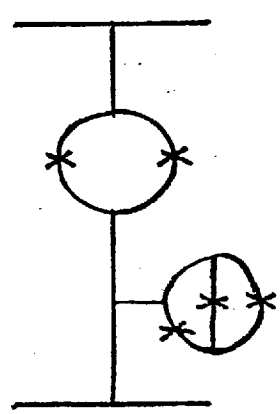

identify them with reduced graphs containing the primitive "tadpoles" of Ref. 7.6. This sort of reduction is a duality transformation, and for more general cases has been investigated through algebraic topology (Ref. 7.6). The point we wish to make here is that this sort of "tadpole" can be regarded as a self-energy graph for the line to which it is attached; in a renormalised theory, they would be redundant, self-energy effects being taken into account in the propagators of the bare lines.

Unfortunately, the dual resonance model has not, at this point in time, been successfully renormalised. This is why it is not unitary, and why complex trajectory functions have had to be used (as in Chapter 5) in phenomenological applications of it. On the other hand, such applications (usually using the B_4 and B_5 functions) have been surprisingly successful, and we are encouraged to hope that the problems of renormalisation and unitarity will not be insurmountable.

Lovelace (Ref. 7.7) has investigated the properties of the Pomeron as described by fig. 7.1.1(a), and the resulting expressions for Pomeron propagators and vertex functions have been incorporated into a phase shift analysis (Ref. 7.8) which enables K^+p elastic scattering data to be explained consistently over a wide energy range without any necessity for introducing exotic resonances.

We have already mentioned that the calculation of the graph of fig. 7.1.1(a) suggests that the Pomeron should behave as a trajectory with half the usual slope. This is in agreement with data on pp elastic scattering from Serpukhov (Ref. 7.9) which was fitted to a slope of 0.40 ± 0.09 GeV^{-2} for the Pomeron.

We also notice that the Pomeron exchange graph for, say, the process $ab \rightarrow ab$ can be turned (by a duality transformation) in to the graph for $\bar{a}b \rightarrow \bar{a}b$. In other words, we have "built in" the requirement that particles and antiparticles should behave similarly in elastic scattering at high energies. This was one of the original theorems of Pomeranchuk, and is in fact fairly well obeyed.

Baryon-antibaryon scattering is an exception to this. It cannot be represented by the graph we have drawn, whereas baryon-baryon scattering can be. Experimentally, there is in fact a significant difference between, for example, pp and $\bar{p}p$ elastic cross-sections at high energies. This serves to remind us that much of what we have said in this section can only be strictly justified in the absence of baryons.

Nevertheless, we have built up a picture of the Pomeron which enables us to understand, in a simple way, many of the known properties of elastic diffraction. We shall find it equally useful for understanding inelastic diffraction.

7.2 THE QUANTUM NUMBERS OF THE POMERON

The idea of the Pomeron given in the previous section can be applied to inelastic as well as to elastic processes, and it is then obvious that the Pomeron does not carry any additive quantum numbers; i.e. diffractive scattering cannot involve the exchange of strangeness, hypercharge, charge or isospin. Many people would regard this as one of the definitive properties of the Pomeron. In our picture, this follows from our use of the "naive quark model"; in this connection it is interesting to note that Baacke (Ref.7.10) has suggested a connection between the isoscalar nature of the Pomeron and the absence of "exotic" resonances.

The situation as regards multiplicative quantum numbers is not so clear-cut. Although it seems likely that G- and C-parity is conserved in diffractive dissociation, this is by no means proven experimentally.

The spin and parity of a diffractively-produced system will in general be different from that of the incident particle; but it will belong to the same spin-parity series. In other words, the "naturalness" of spin-parity is conserved. This is the "Gribov-Morrison" rule, and is strictly true for the dissociation of spinless mesons, in the forward direction, off spinless nucei. While there is no experimental evidence to suggest that this rule is ever broken, it is impossible to say whether it is universally true or whether it is merely a good approximation.

Since the Pomeron seems to carry no quantum numbers, it is difficult to see how it can be a quantised object. It is, in fact, misleading to speak of "Pomerons" as if they could be enumerated. The absurdity of, say, "double Pomeron exchange" is in full accord with what we pointed out in the previous section (fig. 7.1.1(c)).

7.3 FACTORISABILITY AND PERIPHERALITY

In Chapter 4 we were able to explain the Q enhancement in three distinct ways. In the framework of the Dual Resonance Model these are understandable as different views of the interaction defined by this graph:

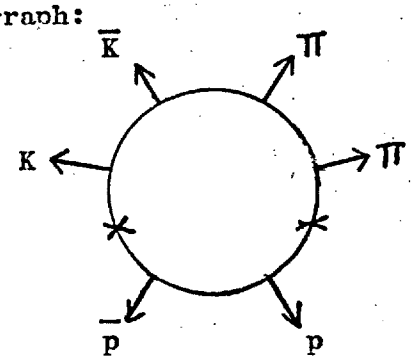

It is trajectories, rather than individual resonances, which are input to this model; so it is natural for us to describe the Q (and L) meson as a Regge recurrence of the kaon. Using a simplified partially dual model, this idea was put to the test in Chapter 5, and we were able to successfully explain the features of the data.

In fact, the model used in Chapter 5 and also the Double-Regge-exchange and CLA models used in Chapters 4 and 6 assumed, essentially, that the amplitude for a diffractive process can be "factorised", i.e. that this sort of reaction:

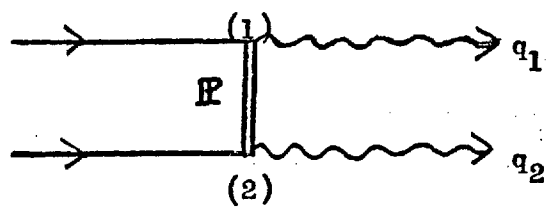

has an amplitude of the form

$$/A/ \;=\; F_1(q_1,t) \;\cdot\; \left(\frac{s}{s_o}\right)^{\alpha(t)} \cdot\; F_2(q_2,t) \qquad (7.3)$$

where F_1 and F_2 are functions only of t and of the variables q_1 and q_2 which define the diffractively produced systems. "s" is the squared effective mass of the component particles of these systems which are assumed to scatter off one another.

In most phenomenological work, the t-dependence of the vertex functions F_1 and F_2 can be written as a simple exponential in t; an

important parameter in this representation is the coefficient of t in the coefficient of t in such an exponential, i.e. the "slope". Since these "form factors" are multiplicative, the slopes are additive.

It follows from the above that the differential cross-section for a diffractive process will have an exponential dependence on t, and the reactions we have studied were found to occur with the following slopes:

(i)	$K^-p \to K^-p$	6.9	GeV^{-2}
(ii)	$K^-p \to K^-(\pi N)^+$	6.4	"
(iii)	$K^-p \to K^-(\pi^-\Delta^{++})$	4.6	"
(iv)	$K^-p \to (K^{*o}\pi^-)p$	7.8	"
(v)	$K^-p \to (K^{*o}\pi^-)(\pi^-\Delta^{++})$	< 2.35	"

We see that, while all these diffractive processes are peripheral, some are more peripheral than others. We can understand this by visualising inelastic diffraction as virtual elastic diffraction. For example, π^-p elastic scattering (at about 10 GeV/c) occurs with a slope of roughly 7.5 GeV^{-2}; so it is not surprising that (iv) above has a slope of this order if it is pictured as virtual π^-p scattering. Reactions (iii) and (v) depend on $K^-\pi^-$ and $\pi^-\pi^-$ scattering respectively, and we would interpret their low slopes as evidence that (in the optical model) the mesons have a lower interaction radius, i.e.are smaller than protons. In the case of reaction (v), the slope is depressed still further by the low value of s which must be applied in this case in eqn.(7.3).

To sum up, we have found throughout this work that, in spite of the undoubtedly complex physical structure of the Pomeron, the amplitudes for diffractive processes can be approximately factorised in the form (7.3), though the details have varied according to the models we have used. In other words, Pomeron exchange can be parametrised in the same way as Reggeon exchange, and this similarity is what has led to the definition of a "trajectory" for the Pomeron.

Empirically, it is found that the Pomeron trajectory must have a high intercept (close to unity) and a much lower slope than do "normal" trajectories. This implies that the cross-sections for diffractive processes must fall slowly, if at all, as the incident beam momentum is increased. In fact there is some theoretical justification (Ref. 7.7) for supposing that they behave like $(\log s)^{-1}$ with respect to elastic scattering cross-sections, where s is the squared total C.M. energy. At the same time, average particle multiplicities will probably increase like log(s), (Ref. 7.11) so that the importance of diffractive dissociation (both "single" and "double") is likely to become greater as more and more channels become open.

In the future, the problems associated with inelastic diffraction will certainly become more urgent and more demanding of both experimental and theoretical workers in hadron physics.

References (7)

7.1 "Dual Multiparticle Theory", V. Alessandrini et al, CERN Preprint TH.1160 (1970)

7.2 "Unitarity in Dual Resonance Models", A. Di Giacomo et al., Physics Letters 33B, 171 (1970)

7.3 K. Kikkawa et al., Physical Review 184, 1701 (1969)

7.4 G. Frye and L. Susskind, Physics Letters 31B, 589 (1970)

7.5 H. B. Neilson, "An Almost Physical Interpretation of the Integrand of the Veneziano Formula", NORDITA Preprint (1969)

7.6 "The Primitive Graphs of Dual Resonance Models", Gross et al., Physics Letters 31B, 592 (1970)

7.7 "Pomeron Form Factors and Dual Regge Cuts", C. Lovelace, Rutgers Preprint (1971)

7.8 "K^+p Reggeised Phase Shift Analysis", C. Lovelace and F. Wagner, CERN Preprint TH.1251 (1970)

7.9 G.G. Beznogikh et al., Physics Letters 30B, 274 (1969)

7.10 "A Note on the Generation of an Isospin Independent Pomeranchuk Contribution in a Charged Particle Veneziano Model", J. Baacke, CERN Preprint TH.1112 (1969)

7.11 "Very High-Energy Collisions of Hadrons", R. P. Feynman, Physical Review Letters, 23, 1415 (1969)

APPENDIX A

Elastic K^-p Scattering at 10 GeV/c.

In this appendix we shall examine the elastic scattering data so far obtained in our experiment. This elastic scattering is overwhelmingly diffractive, i.e. it can be regarded as due to almost pure "Pomeron" exchange between the two particles. (This fact is confirmed by the extreme rarity of the reaction $K^-p \rightarrow K^0n$ at 10 GeV/c ; if the elastic scattering involved an appreciable amount of isovector exchange, then the $K^-p \rightarrow K^0n$ cross-section would be of the same order of magnitude.)

In our data sample, there are 16,261 events fitted to the "elastic" hypothesis. These are highly reliable four-constraint fits, of which only 30 are ambiguous with other hypotheses. Figure A1 shows the logarithmic t-distribution for this data. The line superimposed on this is a straight line fit to the data in the range $0.1 < -t < 0.4$.

The region $-t < 0.1$ has been disregarded in the fit because the events here involve a very short proton track in the bubble chamber and are difficult to observe on film; i.e. there is a bias against these events at the scanning stage. This is the reason for the dip at low t which is apparent in the first two bins in figure A1.

In fitting to a straight line, we are assuming that

$$\frac{d}{dt}(N_{el}) = A.\exp(kt) \qquad (A1)$$

when t is small; the parameters A and k are found to be

$$A = 1.328 \times 10^5 \pm 3\% \quad (GeV^{-2})$$

$$k = 6.88 \pm 2\% \quad (GeV^{-2}) .$$

The "slope" k is used elsewhere in this work. We will also need to know the "microbarn equivalent" of our data sample, and we can now calculate this (and also the total elastic cross-section) by using the known K^-p total cross-section at 10 GeV/c and applying the optical theorem.

FIGURE A1

Logarithmic t-Distribution
for Elastic Scattering.

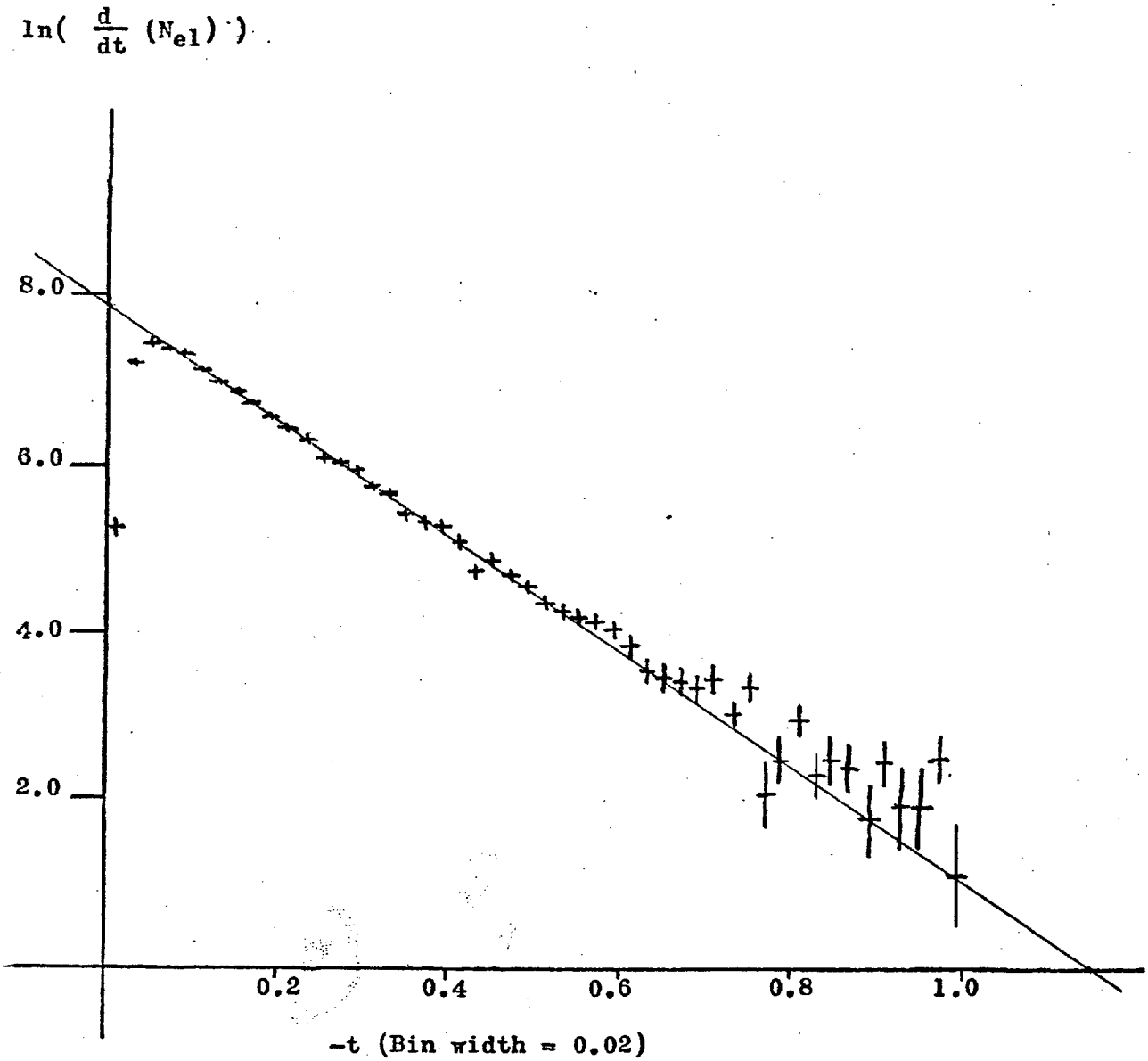

The Optical theorem (assuming that the forward scattering amplitude is imaginary) tells us that

$$\sigma_{tot}^{\,2} = 16\pi\hbar^2 \left.\frac{d\sigma_{el}}{dt}\right|_{t=0}$$

i.e. that

$$\frac{d\sigma}{dN} = \frac{\sigma_{tot}^{\,2} \cdot w}{16\pi\hbar^2 \cdot A} \qquad (A2)$$

where w is the bin width and ln(A) the straight-line intercept from fig. A1. To find the total elastic cross-section, disregarding the biased data with $-t<0.1$, we can use

$$\sigma_{el} = \frac{d\sigma}{dN} \cdot N_{el}(-t<0.1) \cdot \exp(0.1k) \qquad (A3)$$

Then, with $\sigma_{tot} = 22.5 \pm 0.2$ mb. (Ref A1), eqns. (A2) and (A3) give us

$$\frac{d\sigma}{dN} = 0.194\ \mu\text{b./event}, \pm 3\%$$

and $\sigma_{el} = 3.82$ mb., $\pm 3\frac{1}{2}\%$.

This latter result indicates that some 17% of all our events must be elastic, and that the processing efficiency for them is 82.5% , averaged over t. This efficiency is much less than that for inelastic channels, where the difficulty in seeing short-recoil protons is not serious.

Reference A1 W. Galbraith et al., Physical Review 138B (1965),913

APPENDIX B

The Q-pole Residue Function for $K^-p \longrightarrow (K\pi\pi)^-p$

In Chapter 5 we introduce a dual diffractive model for the reaction $K^-p \longrightarrow (K\pi\pi)^-p$, writing our amplitude in the form

$$A = \exp(\tfrac{1}{2}kt_{pp'}) \cdot S_{Pp'} \cdot V(K^- P \longrightarrow (K\pi\pi)^-) \qquad (B1)$$

The Veneziano-type factor V contains poles corresponding to the observed resonances in the $K\pi\pi$ system, and in this appendix we will derive the residue of the pole at $m_{K\pi\pi} = m_Q$. This expression will describe the $(K\pi\pi)$ Dalitz plot from the decay of the Q - meson.

Consider first the charge configuration $K^- P \longrightarrow K^-\pi^+\pi^-$, numbering these particles as in figure B1. Note that in this figure all particles are labelled as though they were outgoing. With this convention, we have

$$p_1 + p_2 + p_3 + p_4 + p_5 = 0 \qquad (B2)$$

for their four-momenta.

FIGURE B1

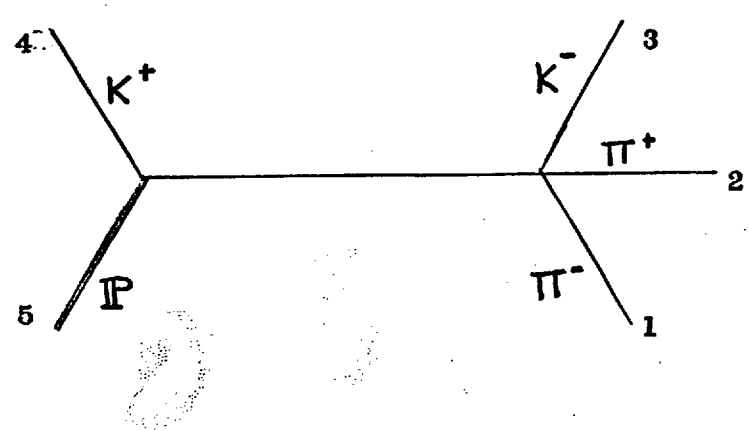

The factor V will contain four terms, two of which contain the Q - meson pole at $s_{123} = s_{45} = m_Q^2$. Taking only these terms, we have

$$V = \alpha_{23} \cdot B_5(-\alpha_{45}, 1-\alpha_{34}, -\alpha_{23}, 1-\alpha_{12}, -\alpha_{15})$$

$$+\alpha_{12} \cdot B_5(-\alpha_{45}, 1-\alpha_{14}, -\alpha_{12}, 1-\alpha_{23}, -\alpha_{53}) \qquad (B3)$$

where the α's are the appropriate trajectory functions. The first term of eqn. (B3) can be written

$$\alpha_{23} \cdot \sum_{k=0}^{\infty} \left[(-1)^k \cdot \binom{-\alpha_{15}+\alpha_{34}-1+\alpha_{23}}{k} \cdot B_4(1-\alpha_{34},k-\alpha_{45}) \cdot B_4(k+1-\alpha_{12},-\alpha_{23}) \right] \tag{B4}$$

using the Hopkinson-Plahte series representation of the B_5 function. When $\alpha_{45}=1$, i.e. at the Q-pole, eqn.(B4) has residue

$$\alpha_{23}.\alpha_{34} \cdot B_4(1-\alpha_{12},-\alpha_{23}) + \alpha_{23}.(\alpha_{15}-\alpha_{34}+1-\alpha_{23}) \cdot B_4(2-\alpha_{12},-\alpha_{23}) \tag{B5}$$

which can be rearranged to give

$$B_4(1-\alpha_{12},1-\alpha_{23}). \left\{ -(1-\alpha_{12}).(1-\alpha_{23}) - \alpha_{15}.(1-\alpha_{12}) - \alpha_{34}.(1-\alpha_{23}) + \alpha_{34} \right\} \tag{B6}$$

Similarly, the residue function from the second term of eqn. (B3) will be

$$B_4(1-\alpha_{12},1-\alpha_{23}). \left\{ -(1-\alpha_{12}).(1-\alpha_{23}) - \alpha_{35}.(1-\alpha_{23}) - \alpha_{14}.(1-\alpha_{12}) + \alpha_{14} \right\} \tag{B7}$$

so that the whole of eqn. (B3) gives us

$$\begin{aligned} \underset{(\alpha_{45}=1)}{\text{Res (V)}} &= -B_4(1-\alpha_{12},1-\alpha_{23}). \left\{ 2(1-\alpha_{12}).(1-\alpha_{23}) + \right. \\ &\quad (\alpha_{35}+\alpha_{34}).(1-\alpha_{23}) + \\ &\quad \left. (\alpha_{14}+\alpha_{15}).(1-\alpha_{12}) - (\alpha_{34}+\alpha_{14}) \right\} \\ &= W, \text{ say.} \end{aligned} \tag{B8}$$

To simplify (B8), note that in the ideal case of linear, parallel trajectories

$$\begin{aligned}\alpha_{35} + \alpha_{34} &= \alpha_k^o + \alpha_\rho^o + \alpha'.(s_{35}+s_{34}) \\ &= \alpha_k^o + \alpha_\rho^o + \alpha'.(s_{12}-m_Q^{\,2}+2m_k^{\,2}+m_{I\!P}^{\,2}) \\ &= \alpha_{12} - 1 + \alpha'T \qquad \text{(B9)}\end{aligned}$$

where T is the squared "mass" of the Pomeron. In similar fashion, we obtain

$$\alpha_{14} + \alpha_{15} = \alpha_{23} - 1 + \alpha'T \qquad \text{(B10)}$$

and inserting (B9) and (B10) into (B8) we find

$$W = -B_4(1-\alpha_{12},1-\alpha_{23}).\left\{\alpha'T.(2-\alpha_{23}-\alpha_{12}) - (\alpha_{34} + \alpha_{14})\right\} \qquad \text{(B11)}$$

Now,

$$\begin{aligned}\alpha_{34} + \alpha_{14} &= \alpha_\rho^o + \alpha_k^{o}* + \alpha'.(s_{34}+s_{14}) \\ &= \alpha_\rho^o + \alpha_k^{o}* + \alpha'.((p_3+p_4)^2+(p_1+p_4)^2) \\ &= \alpha_\rho^o + \alpha_k^{o}* + \alpha'.(3m_k^{\,2}+m_\pi^{\,2}+2p_4.(p_3+p_1)) \\ &= 1 + 2\alpha'.(m_k^{\,2} + p_4.(p_3+p_1))\end{aligned}$$

using $\alpha_\rho(m_\pi^{\,2}) = \alpha_k*(m_k^{\,2}) = \frac{1}{2}$, i.e. taking the ρ (or K^*) trajectory to be half a unit above the π (or K) trajectory. Now using (B2), we find

$$\begin{aligned}\alpha_{34} + \alpha_{14} &= 1 - 2\alpha'.p_4.(p_2+p_5) \qquad \text{(B12)} \\ &= \alpha'.(T - 2p_2.p_4)\end{aligned}$$

and using this, (B11) leads to

$$W = -B_4(1-\alpha_{12},1-\alpha_{23}).(\alpha'T(1-\alpha_{12}-\alpha_{23}) + 2\alpha'p_2.p_4) \qquad \text{(B13)}$$

Having obtained eqn. (B13), we can immediately write down the corresponding expressions describing the other Q - decay charge configurations $K^0\pi^-\pi^0$ and $K^-\pi^0\pi^0$. In both these cases we number the particles 3,2, and 1 in that order. For these charge states, two more terms must be included in eqn. (B3), and these lead to an extra term in (B13). This term differs from (B13) only by the interchange $1 \leftrightarrow 2$ of the particle labels, and is added for the $K^-\pi^0\pi^0$ case and subtracted from (B13) for the $K^0\pi^-\pi^0$ case.

The result we have derived, eqn (B13), has a number of interesting features. In particular, when T = 0, it reduces to

$$W = -2\alpha' p_2 \cdot p_4 \, . B_4(1-\alpha_{12}, 1-\alpha_{23}) \qquad \text{(B14)}$$

and this will describe the $Q \longrightarrow K^-\pi^+\pi^-$ Dalitz plot when the Q is peripherally produced.

At the pole where α_{12} or $\alpha_{23} = 1$, i.e. for $Q \rightarrow \rho^0 K^-$ or for $Q \rightarrow K^{*0}\pi^-$, the residue of (B14) is simply $-2\alpha' p_2 \cdot p_4$, and this describes the correlation between the spin of the ρ or K^* and that of the Q. This coefficient is slowly-varying over the Dalitz plot.

Close to the $K^*-\rho$ overlap region on the Dalitz plot, the B_4 function can be expanded like this:

$$B_4(1-\alpha_{12}, 1-\alpha_{23}) \approx \left(\frac{1}{1-\alpha_{12}} \cdot \frac{1}{1-\alpha_{23}}\right) \Big/ \left(\frac{1}{2-\alpha_{12}-\alpha_{23}}\right)$$

$$= \frac{1}{1-\alpha_{12}} + \frac{1}{1-\alpha_{23}}$$

$$= \frac{1/\alpha'}{(s_{12}-m_\rho^2) + i\Gamma_\rho m_\rho} + \frac{1/\alpha'}{(s_{23}-m_{k^*}^2) + i\Gamma_{k^*} m_{k^*}} \qquad \text{(B15)}$$

Here, the widths of the ρ and $K^*(890)$ resonances enter through the imaginary parts of the trajectory functions as explained in Appendix C. The terms of eqn. (B15) are Breit-Wigner function for the ρ and for the K^*, interfering constructively where the ρ and K^* bands intersect on the Dalitz plot.

APPENDIX C

Regge Trajectory Functions for Use in Veneziano Amplitudes.

A typical amplitude of the Veneziano type is

$$V = \frac{\Gamma(1-\alpha(s)).\ \Gamma(1-\alpha(t))}{\Gamma(1-\alpha(s)-\alpha(t))} \qquad (C1)$$

and this will describe, for example $K^- \pi^+ \longrightarrow K^- \pi^+$ scattering. It has poles at positive integral values of $\alpha(s)$ and $\alpha(t)$, and close to the pole at, say, $\alpha(s) = n$ we can expand it in the form

$$V \approx \frac{\Gamma(1-\alpha(t))}{\Gamma(1-n-\alpha(t))} .(-1)^{n+1}. \frac{1}{(n-1)!} . \frac{1}{\alpha(s)-n} \qquad (C2)$$

If $\alpha(s)$ is real, this pole is in the physical region, violating unitarity. So, we add a small imaginary part to $\alpha(s)$, putting in the form

$$\alpha(s) = \alpha^{\circ} + \alpha' s + i\alpha''(s-s_o)^{\gamma}. \Theta(s-s_o) \qquad (C3)$$

Then, if $\mathrm{Re}\,\alpha(s_{res}) = n$, (C2) becomes

$$V \propto \frac{1}{\alpha'(s-s_{res}) + \mathrm{Im}\,\alpha(s_{res})} \qquad (C4)$$

close to the pole. This is simply a Breit-Wigner in s with the half-width

$$\Gamma_{res}\, m_{res} = \mathrm{Im}\,\alpha(s_{res})/\alpha'' \qquad (C5)$$

i.e. we must choose the trajectory parameters so that

$$\alpha''(s_{res} - s_o)^{\gamma} = \alpha' \Gamma_{res} m_{res} \qquad (C6)$$

as well as

$$\alpha^{\circ} + \alpha' s_{res} = n = \text{spin of resonance} \qquad (C7)$$

The parameter s_0 represents the value of s at which we begin to add an imaginary part to $\alpha(s)$, and we choose this to be the threshold mass squared for the channel concerned. For example, in $K^-\pi^+ \rightarrow K^-\pi^+$ the s-channel trajectory function must be real below $s_0 = (m_K + m_\pi)^2$.

From (C6) it is clear that at high values of s_{res}, where $s_{res} \gg s_0$,

$$\Gamma_{res} \approx \frac{\alpha''}{\alpha'} \cdot (m_{res})^{2\gamma-1} \qquad (C8)$$

and if the widths of our resonances are not to decrease when the masses become large we must have $\gamma \geqslant \frac{1}{2}$.

Returning now to eqn.(C1), we see that at large s and small t we can write

$$V \approx \Gamma(1-\alpha(t)).(1-\alpha(s))^{\alpha(t)} \qquad (C9)$$

which is the correct Regge limit when $\alpha(s)$ is real. When $\alpha(s)$ is of the form (C3), (C9) becomes

$$V \approx \Gamma(1-\alpha(t)).\ e^{i\pi\alpha(t)}.(\alpha' s+\alpha^{\circ}-1+i\alpha''(s-s_0)^{\gamma})^{\alpha(t)}$$

or, since we are considering large s,

$$V \approx \Gamma(1-\alpha(t)).e^{i\pi\alpha(t)}.(\alpha' s + i\alpha'' s^{\gamma})^{\alpha(t)} \qquad (C10)$$

From this, we can see that in order to retain correct Regge asymptotic behaviour we must have $\gamma \leqslant 1$. So we must choose the exponent γ in the range $\frac{1}{2} \leqslant \gamma \leqslant 1$. Bearing this in mind, and using (C6) and (C7), we have chosen parameters for the K^*, ρ, K and π trajectories used in chapter 5. These are tabulated in fig.C1, and the corresponding Chew-Frautschi plots are shown in figs. C2 and C3 for comparison with the known masses of the resonances concerned. Similarly, figs. C4, C5 and C6 show the known resonance widths and the curve implied in each case by eqn. (C6). The masses and widths used in calculating the trajectory parameters and in figs. C2–C6 are those published by the Particle Data Group in the Jan. 1970 Review of Particle Properties.

FIGURE C1

Table of Trajectory Function Parameters.

Trajectory	α^0	α'	α''	s_0	γ
K^*	0.35	0.82	0.095	0.4	1
ρ	0.48	0.95	0.11	0.078	$\frac{1}{2}$
K	-0.166	0.68	0.0535	0.244	1
π	-0.017	0.88	(Not required)		

In deciding on these parameters, we first obtained α^0 and α' in each case from the Chew-Frautschi plots (Figs. C2 and C3). Then, using s_0 = squared threshold mass, it remains to fix α'' and γ.

For the ρ trajectory, where the ρ, f and g mesons appear with almost equal widths, we use $\gamma = \frac{1}{2}$. For the K and K^* trajectories, we use $\gamma = 1$.

In calculating α'' in the case of the K trajectory we have not, for reasons explained in Chapter 5, taken the Q width into account.

FIGURE C2

K and K^* trajectories

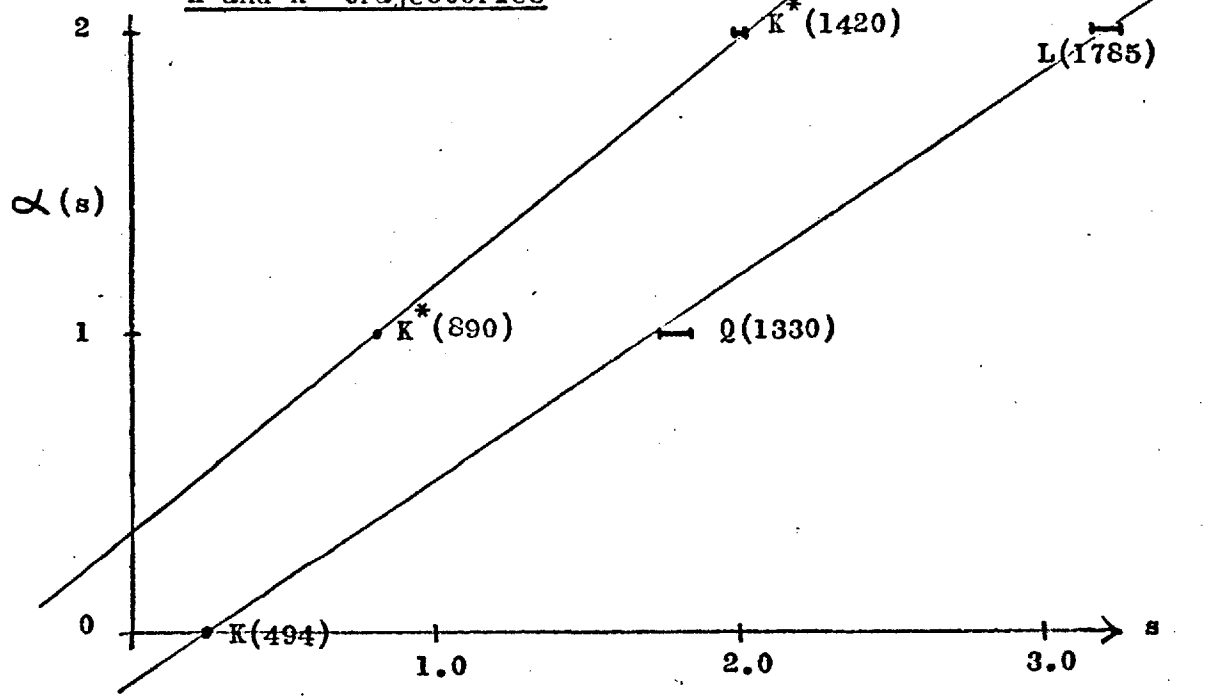

FIGURE C3

π and ρ trajectories

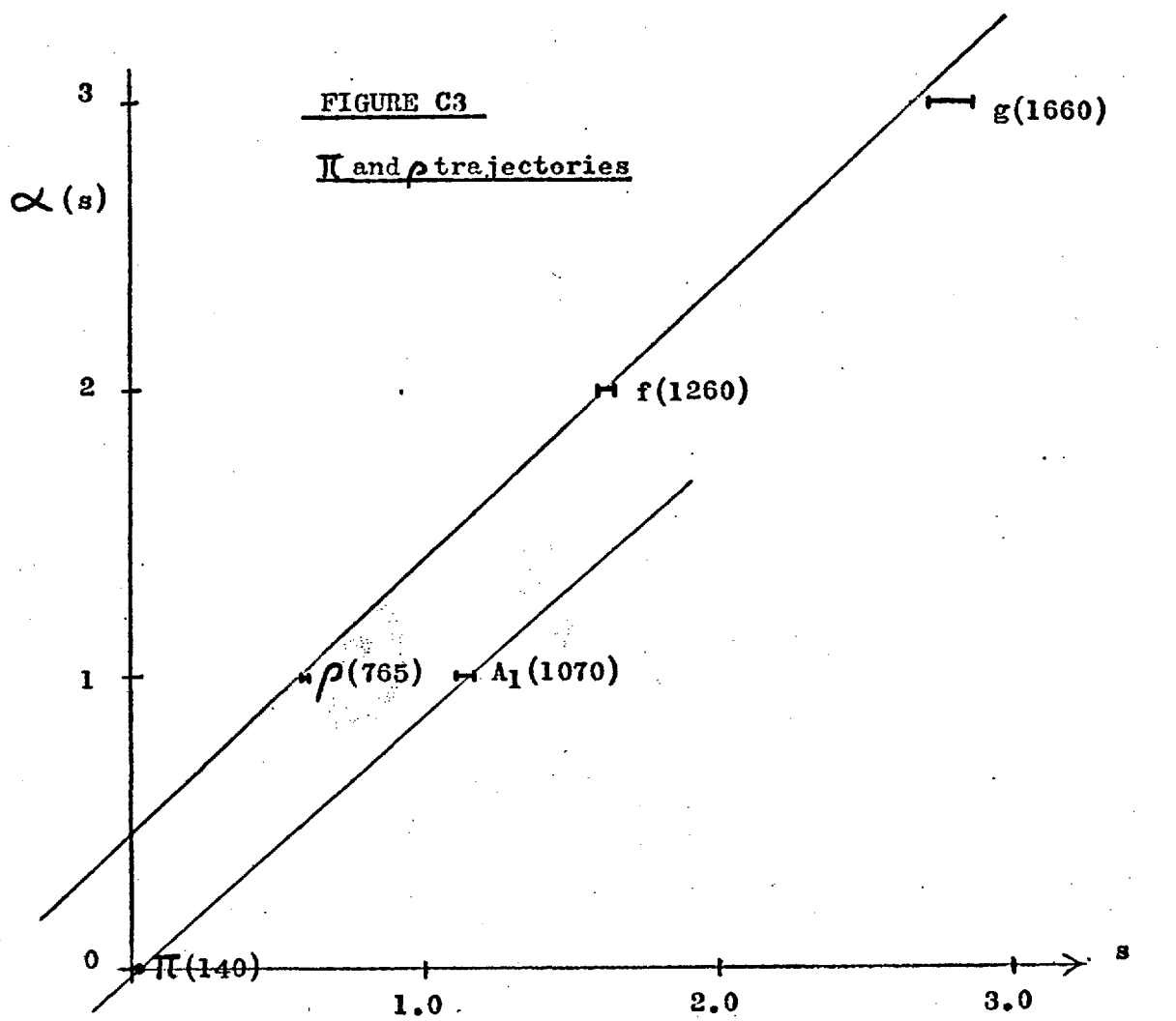

FIGURE C4 K^* trajectory

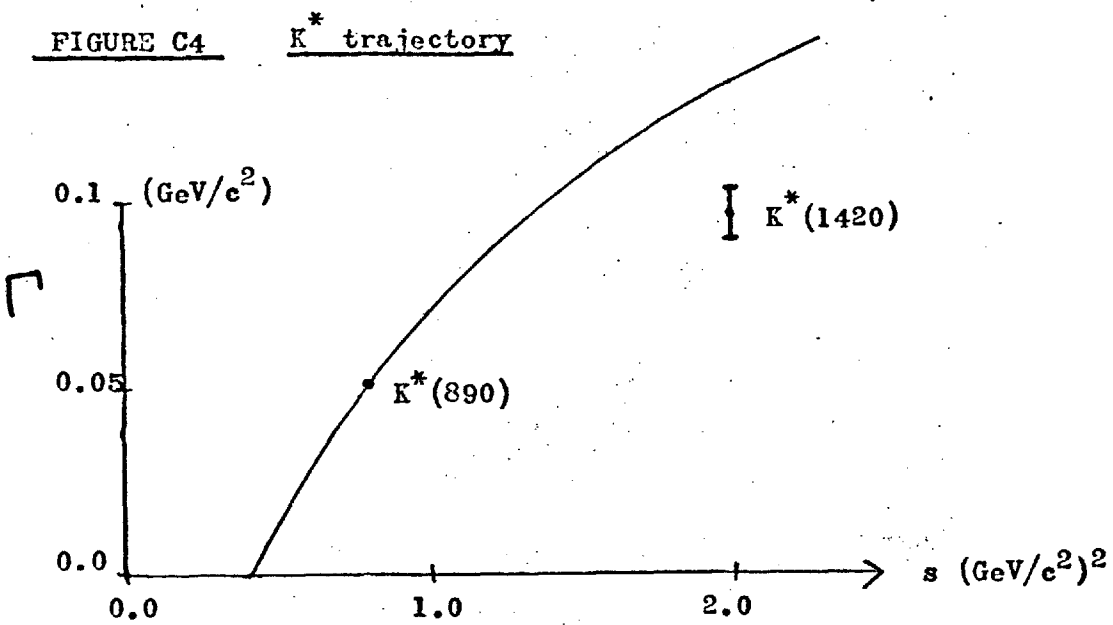

FIGURE C5 K trajectory

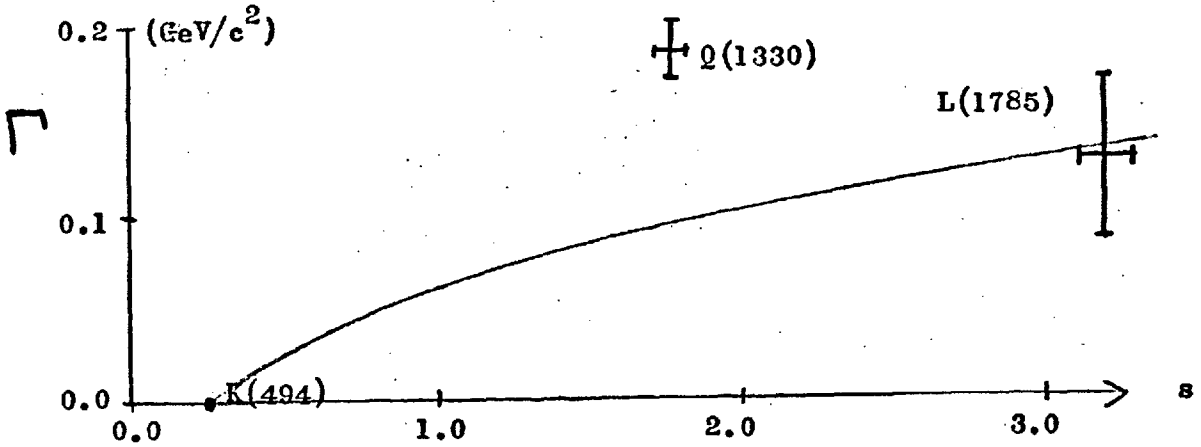

FIGURE C6 ρ trajectory

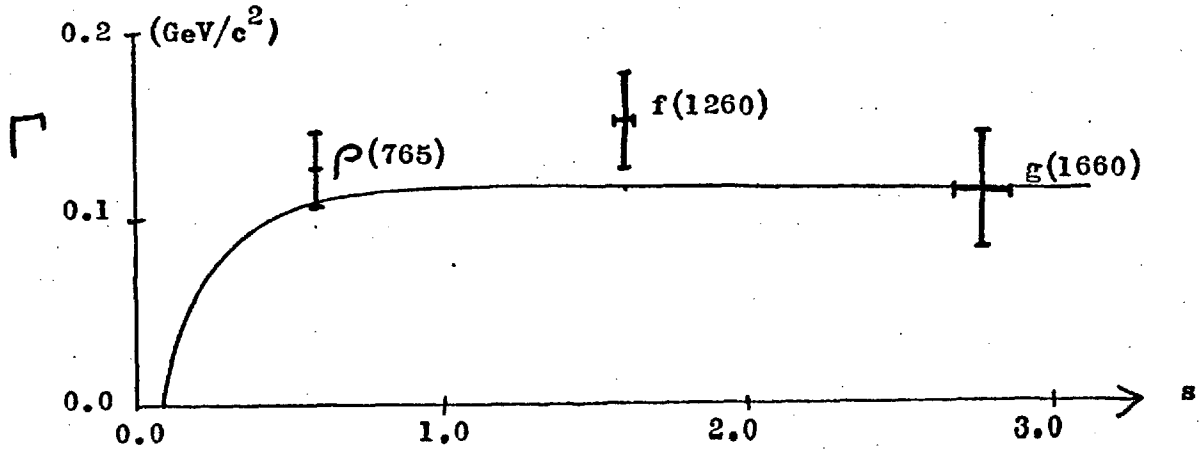

APPENDIX D

Isospin Analysis of the Reactions $K^-p \to \bar{K}N$ and $K^-p \to \bar{K}\pi N$

The purpose of this appendix is to derive relationships between cross-sections for the various $K^-p \to \bar{K}\pi N$ reactions, paying particular attention to the isospin of the πN system. The results are made use of in Chapter 3.

By way of introduction, we will first examine the $K^-p \to \bar{K}N$ amplitudes.

$K^-p \to \bar{K}N$

This reaction occurs in two charge states, namely

$$K^-p \to K^-p \qquad \text{(D1)}$$

and

$$K^-p \to \bar{K}^o n \qquad \text{(D2)}$$

and we will denote the amplitudes for these two processes by A_1 and A_2.

We introduce total isospin amplitudes F_o and F_1, where the suffix denotes the total (s-channel) isotopic spin. The A's and the F's are inter-related, and using Clebsch-Gordan coefficients we find that

$$A_1 = \tfrac{1}{2}(F_1 + F_o) \qquad \text{(D3)}$$

and

$$A_2 = \tfrac{1}{2}(F_1 - F_o) \quad . \qquad \text{(D4)}$$

Alternatively, we may use t-channel isospin amplitudes G_o and G_1, corresponding respectively to isoscalar and isovector exchange particles. In this case, we find that

$$A_1 = \tfrac{1}{2}(G_1 + G_o) \qquad \text{(D5)}$$

and

$$A_2 = G_1 \quad . \qquad \text{(D6)}$$

It is important to realise that the A's, F's and G's are no more than alternative choices for the two isotopically independent amplitudes which must contribute to the $K^-p \to \bar{K}N$ reactions. A_1 and A_2 are useful because they relate directly

to the cross-sections for reactions (D1) and (D2). The F's and G's, on the other hand, are introduced because they correspond to definite I-spin states in the s and t channels and so are more physically relevant than the A's.

Now, at 10 GeV/c incident K^- momentum, we are well above the s-channel resonance region where the total K^-p isospin would be important. The C.M.S. energy is 4.46 GeV, and for such a system the isospin is not well defined. It would therefore be very surprising if the $K^-p \to \bar{K}N$ amplitude were dependent on the total I-spin, and we can say that

$$F_0 = F_1 \quad . \tag{D7}$$

It follows, using eqns. (D3)-(D6), that

$$A_1 = F_0 = F_1 = \tfrac{1}{2}G_0 \tag{D8}$$

and

$$A_2 = G_1 = 0 \quad . \tag{D9}$$

We conclude that the elastic reaction (D1) will occur, whereas the charge-exchange reaction (D2) will be suppressed. If we examine the t-channel, this elastic scattering will appear as the result of the exchange of an isoscalar object. Needless to say, these conclusions are well confirmed by experiment and the exchanged object is the familiar Pomeron.

It remains to point out that the preceding argument could equally well be completely reversed, and we should not regard our premises as being any more fundamental than our conclusions. Suffice it to say that:

> for $K^-p \to \bar{K}N$ scattering at high energies, the dominance of Pomeron exchange implies, and is implied by, the fact that the scattering is independent of the s-channel K^-p isospin. (D10)

<u>$K^-p \to \bar{K}\pi N$</u>

We will write the amplitudes for these reactions as

$$A_1 = A(K^-p \to K^0\pi^-p) \tag{D11}$$

$$A_2 = A(K^-p \to K^-\pi^0p) \tag{D12}$$

$$A_3 = A(K^-p \to K^-\pi^+n) \qquad \text{(D13)}$$

and

$$A_4 = A(K^-p \to K^o\pi^on) \quad . \qquad \text{(D14)}$$

These can be decomposed in terms of three independent isospin amplitudes, but these can be chosen in various ways. We will make two such decompositions. If I_S, I_T and I_B are the isospins in the channels shown in figure D1, we firstly consider amplitudes F_T^B labelled by I_T and I_B, and secondly amplitudes G_S^B labelled by I_S and I_B.

The F_T^B which contribute are $F_o^{\frac{1}{2}}$, $F_1^{\frac{1}{2}}$ and $F_1^{3/2}$. Referring to figure D2, and using Clebsch-Gordan coefficients, we arrive at the relations

$$3A_1 = \qquad\qquad 2F_1^{\frac{1}{2}} + F_1^{3/2} \qquad \text{(D15)}$$

$$3A_2 = -\sqrt{3/2}\,F_o^{\frac{1}{2}} + \sqrt{\tfrac{1}{2}}\,F_1^{\frac{1}{2}} + \sqrt{2}\,F_1^{3/2} \qquad \text{(D16)}$$

$$3A_3 = \sqrt{3}\,F_o^{\frac{1}{2}} - F_1^{\frac{1}{2}} + F_1^{3/2} \qquad \text{(D17)}$$

$$3A_4 = \qquad\qquad -\sqrt{2}\,F_1^{\frac{1}{2}} + \sqrt{2}\,F_1^{3/2} \qquad \text{(D18)}$$

The G_S^B are $G_o^{\frac{1}{2}}$, $G_1^{\frac{1}{2}}$ and $G_1^{3/2}$; in terms of these (see fig. D3) the A's decompose like this:

$$2\sqrt{3}\,A_1 = \sqrt{2}\,G_o^{\frac{1}{2}} - \sqrt{2}\,G_1^{\frac{1}{2}} - G_1^{3/2} \qquad \text{(D19)}$$

$$2\sqrt{3}\,A_2 = -G_o^{\frac{1}{2}} - G_1^{\frac{1}{2}} + \sqrt{2}\,G_1^{3/2} \qquad \text{(D20)}$$

$$2\sqrt{3}\,A_3 = \sqrt{2}\,G_o^{\frac{1}{2}} + \sqrt{2}\,G_1^{\frac{1}{2}} + G_1^{3/2} \qquad \text{(D21)}$$

$$2\sqrt{3}\,A_4 = -G_o^{\frac{1}{2}} + G_1^{\frac{1}{2}} - \sqrt{2}\,G_1^{3/2} \qquad \text{(D22)}$$

The magnitudes of A_1, A_2 and A_3 are experimentally measurable; this is not possible for A_4 because it corresponds to an unfittable reaction. Disregarding their absolute phase (as we must) the three independent isospin amplitudes (however we choose them) involve five real numbers, and we cannot extract these from our data without making some assumptions.

In view of what we found for the $K^-p \to \overline{K}N$ reactions, let us examine the consequences of assuming that $G_o^{\frac{1}{2}} = G_1^{\frac{1}{2}}$.

FIGURE D1

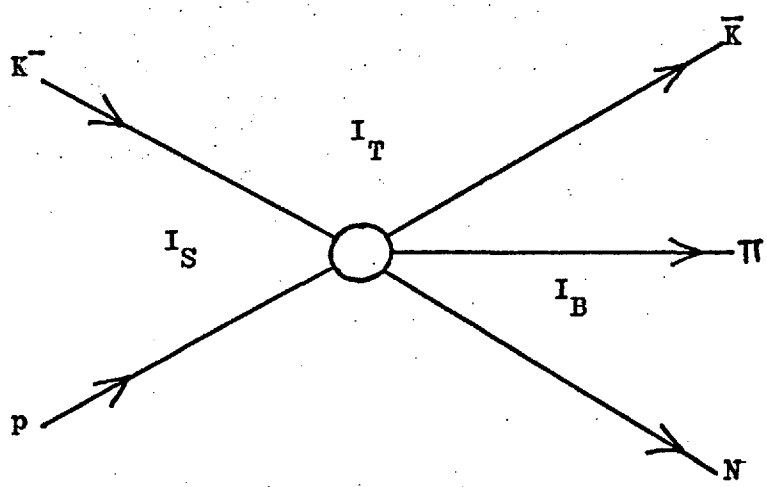

FIGURE D2

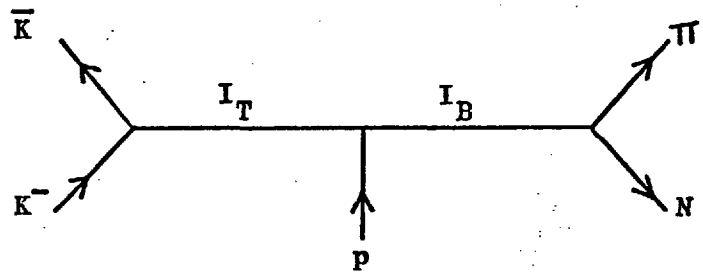

FIGURE D3

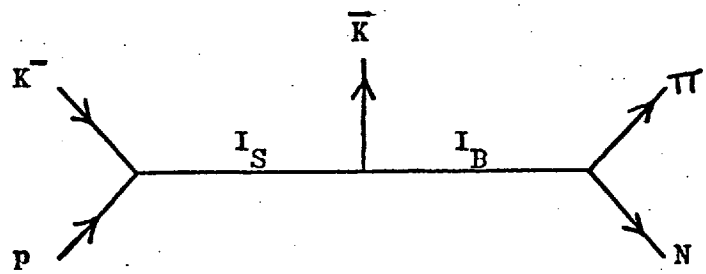

In this case, it follows easily that $F_1^{\frac{1}{2}} = 0$, i.e. that isovector exchange occurs only when an $I = 3/2$ πN system is produced. So we have (omitting the I_T suffix)

$$3A_1 = F^{3/2} \tag{D23}$$

$$3A_2 = -\sqrt{3/2}\, F^{\frac{1}{2}} + \sqrt{2}\, F^{3/2} \tag{D24}$$

$$3A_3 = \sqrt{3}\, F^{\frac{1}{2}} + F^{3/2} \tag{D25}$$

Writing $/A_i/^2 = \sigma_i$, it follows that

$$/F^{\frac{1}{2}}/^2 = 2/9\,(\sigma_2 + \sigma_3 - 3\sigma_1) \tag{D26}$$

$$/F^{3/2}/^2 = \sigma_2 \tag{D27}$$

$$6\sqrt{3}\ \mathrm{Re}(F^{\frac{1}{2}}.F^{3/2\,*}) = \sigma_3 + 3\sigma_1 - 2\sigma_2 \tag{D28}$$

and since both sides of (D26) must be positive, we expect to find that

$$\sigma_2 + \sigma_3 > 3\sigma_1 \quad , \tag{D29}$$

and this will provide a test of the assumption that $F_1^{\frac{1}{2}} = 0$.

Another simplifying assumption which will prove useful is that interference can be neglected between the various isospin amplitudes. Applying this to eqns. D15–D17, and writing $/F/^2 = \Sigma$, we get

$$9\sigma_1 = 4\Sigma_1^{\frac{1}{2}} + \Sigma_1^{3/2} \tag{D30}$$

$$9\sigma_2 = 3/2\Sigma_0^{\frac{1}{2}} + \tfrac{1}{2}\Sigma_1^{\frac{1}{2}} + 2\Sigma_1^{3/2} \tag{D31}$$

$$9\sigma_3 = 3\Sigma_0^{\frac{1}{2}} + \Sigma_1^{\frac{1}{2}} + \Sigma_1^{3/2} \tag{D32}$$

which are easily solved to give the Σ's in terms of the known cross-sections σ_1, σ_2 and σ_3.

Finally, consider the isospin of the $(\pi N)^+$ systems which are produced in reactions (ii) and (iii). It follows from (D16) and (D17) or from (D20) and (D21) that the ratio

$$R = \sigma_2/\sigma_3 \tag{D33}$$

will be equal to $\frac{1}{2}$ wherever $I(\pi N)^+ = \frac{1}{2}$, and 2 wherever $I(\pi N)^+ = 3/2$. For this reason the ratio R is a useful clue in investigating the production mechanisms.

APPENDIX E

Longitudinal Momentum Phase Space for Presentation of Data.

Data on the high-energy collisions of hadrons can be presented in various ways, according to whatever aspects of the data are of interest to the experimenter. We describe here a technique (Ref. E1) which is particularly useful for displaying the features of three-body (or quasi-three-body) final states.

We exploit the fact that particles produced in hadronic interactions have transverse momenta which are generally restricted to a few hundred MeV/c. At medium and high energies (beam momentum greater than, say, 5 GeV/c in the lab) the transverse momenta of secondary particles are therefore considerably lower than their typical longitudinal momenta (which we will take in the CM frame) . So, we can ignore the transverse momenta and consider the longitudinal momentum phase space.

Denoting the longitudinal momenta of three final-state particles by q_i (i=1,3) and their masses by m_i , we have by momentum conservation

$$\sum_i q_i = 0 \qquad \text{(E1)}$$

and by energy conservation

$$\sum_i (q_i^2 + m_i^2)^{\frac{1}{2}} \leq E_{tot} \qquad \text{(E2)}$$

where the equality holds in the latter equation when the transverse momenta are neglected. Since we can also ignore the m_i compared with the q_i at high energy, (E2) leads to

$$\sum_i /q_i/ \approx E_{tot} \qquad \text{(E3)}$$

Now, (E1) implies that the q_i can be displayed in two dimensions, using three coordinate axes at 120° to one another (On the same principle as a Dalitz plot). Plotted in this way, eqn. (E3) will describe the outline of a regular hexagon, as is shown in figure E1. If (E3) were exact, events plotted on this graph would lie

along the boundary of the hexagon, but insofar as the m_i and the transverse momenta are not exactly zero the events will actually lie slightly within the boundary.

A "Hexagon Plot" of the type descibed shows the longitudinal momenta of the three particles, and the correlations between them, in a clear and easily digestible way. Each face of the hexagon can be associated with a particular multiperipheral graph, as is shown in Fig. E1.

A useful economy in presentation can be made by plotting, rather than the hexagonal scatter plot, a histogram of the angle ω (see fig. E1). This angle will be given by

$$\tan\omega = \frac{\sqrt{3}q_1}{q_1 + 2q_3} \quad . \qquad \text{(E4)}$$

Various extensions and refinements of the longitudinal momentum phase space technique can be made; for example, some of the information lost by assuming that the transverse momenta are negligible can be retained by making scatter plots of the angle ω against the transverse momenta of the three particles. If we consider four-particle final states, it turns out that the longitudinal momentum phase space lies just inside the surface of a cuboctahedron, with the four momenta measured by distances from four planes which lie within it.

Reference E1 This technique was originally suggested by Van Hove (Physics Letters 28B (1969) 429; also Nuclear Physics B9 (1969) 331) and some applications to this experiment appear in Ref. 1.19.

FIGURE E1

The Hexagon Plot for Longitudinal Momenta of Three-Particle Final States.

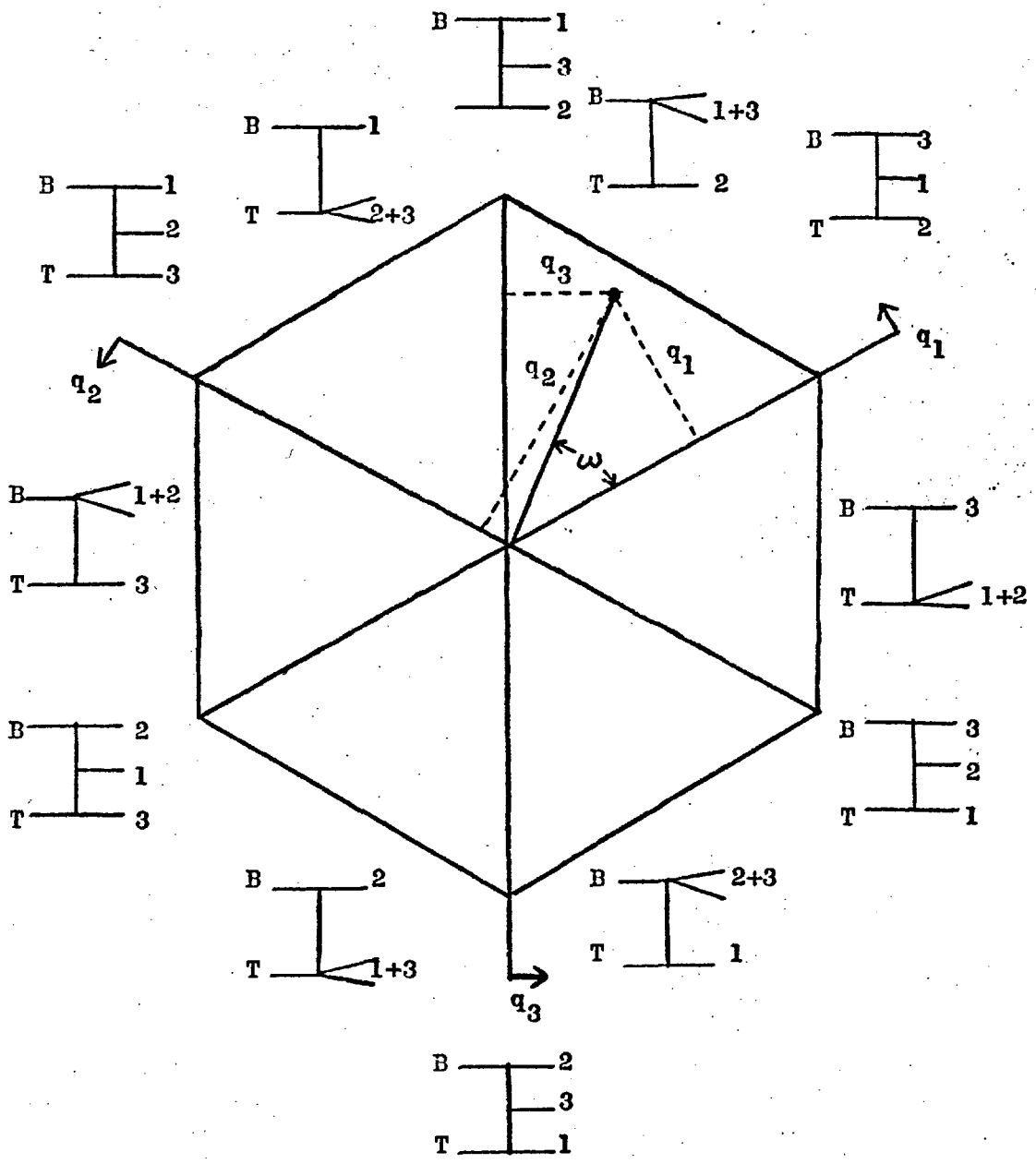

B=Beam, T=Target.

ACKNOWLEDGEMENTS

I wish to thank all my family and friends for their support and encouragement during the preparation of this thesis. I am grateful to all those who contributed to the success of the experiment and so made this work possible.

Thanks are due especially to my colleagues at Imperial College and elsewhere, and in particular to Drs. S. Goldsack and G. Otter, for the benefit of their advice and criticism.

M. J. C.